POLITECNICO
DI TORINO

Master degree course in Nanotechnologies for ICTs

Master Degree Thesis

Quantum well intermixing in high-power laser diodes

Supervisors
Prof. Matteo Cocuzza
Ph.D. Alessio Verna

Candidate
Andrea Gerini
ID: 236140

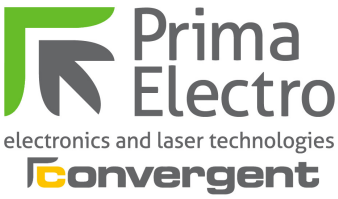

Prima Electro / Convergent Photonics
Dott. Claudio Coriasso
Dott. ssa Giuliana Morello

Academic year 2017-2018

Summary

In recent years the use of laser diodes has increased significantly in industry for material processing applications. In particular this kind of devices, realized in III-V compounds (InGaAs/AlGaAs) emitting around 920 nm, are commonly used to optically pump fiber lasers. High-power laser diodes can reach several MW/cm^2 power densities at the semi-reflecting mirrors of the optical cavity that, interacting with any defect on the facet itself, can induce a positive feedback mechanism that leads to catastrophic optical mirror damage (COMD). There are several approaches to increase the COMD threshold such as better facet passivation and non-injected regions at the facets.

Since most high-power semiconductor laser diodes are realized with a quantum well structure, it's also possible to integrate non-absorbing mirrors (NAMs) by realizing post-growth regions with larger bandgap thus reducing the absorption at the laser emission wavelength. This can be done using quantum well intermixing which consists in the introduction of defects, more specifically III-group vacancies, that induce compositional disordering between quantum well barriers and well itself. This phenomenon can be evaluated studying the photoluminescence (PL) wavelength shift with respect to the initial quantum well.

The aim of this thesis was the investigation of quantum well intermixing in InGaAs/AlGaAs material, induced by impurity-free vacancy diffusion (IFVD) or impurity-induced disordering (IID) techniques, while striving to maintain compatibility with the current production process at the Turin facility of Prima Electro/Convergent Photonics. These techniques have been studied in order to induce a spatially-selective compositional disordering characterized by the maximum possible $\Delta\lambda$ in the NAM region and the minimum possible change in the emission wavelength of the rest of the resonant cavity.

The IFVD approach is relatively simple since it only requires the deposition of dielectric layers, in this work PECVD SiO_2 and Si_3N_4, to either enhance or suppress the intermixing which is caused by the out-diffusion of Ga atoms from the substrate during annealing. The IID approach, instead, requires a much more complex equipment since the disordering is enhanced by ion implantation followed by the annealing.

A series of experiments was carried out on samples of 2 cm^2 in order to determine the optimal parameters for an eventual complete fabrication process. In particular the effect of different dielectric materials and different annealing conditions has been studied. These optimal process parameters have then been transferred to whole-wafer processes to evaluate the effectiveness of NAMs during the diode operation, in particular from the yield of the burn-in test.

A finite element model of the IFVD process has been developed coupling the vacancy

generation and diffusion with the compositional disordering. Its results, in particular the vacancy profiles, have been compared with simulations of the vacancies introduced by the IID process and used to evaluate the implantation and annealing conditions of an ongoing experiment.

Acknowledgements

I wish to thank all the amazing people in via Schiaparelli who have made these months in Prima Electro/Convergent Photonics a truly stimulating and unforgettable experience from both a human and a professional point of view.
A special thanks to Claudio Coriasso and Giuliana Morello for all their teachings and help during this experience. I also wish to thank Prof. Amr Helmy who helped me better understand what I was studying.
Finally, I would like to thank my family for all the support given me during these years.

Contents

List of Tables

List of Figures

List of Acronyms

AR Anti-reflective.

BPP Beam Parameter Product.

CB Conduction Band.

COMD Catastrophic Optical Mirror Damage.

CW Continuous wave.

DOS Density of States.

FDM Finite Differences Method.

FEM Finite Element Method.

HR High-reflectivity.

ICP Inductively Coupled Plasma.

ICP-RIE Inductively Coupled Plasma Reactive Ion Etching.

IFVD Impurity-Free Vacancy Diffusion.

IID Impurity-Induced Disordering.

JDOS Joint Density of States.

MBE Molecular Beam Epitaxy.

MOCVD Metal-Organic Chemical Vapour Deposition.

NAM Non-Absorbing Mirror.

ODE Ordinary Differential Equation.

P-PAID Pulsed Photo-Absorption Induced Disordering.

PAID Photo-Absorption Induced Disordering.

PDE Partial Differential Equation.

PECVD Plasma Enhanced Chemical Vapour Deposition.

PL Photoluminescence.

QW Quantum Well.

QWI Quantum Well Intermixing.

RF Radio Frequency.

RIE Reactive Ion Etching.

RTA Rapid Thermal Annealing.

SCH Separate Confinement Heterostructure.

SEM Scanning Electron Microscope.

TFM Transfer Matrix.

VB Valence Band.

Introduction

Nowadays high-power laser diodes are used in several applications where compact coherent light sources with high efficiency and high optical power are required. In particular, devices emitting in the $800 \div 1000$ nm region are used as optical pumping sources for solid state fiber lasers that are widely used in industrial applications such as laser cutting, welding and additive manufacturing.

The high-power laser diodes consist usually of a single GaAs or InGaAs quantum well embedded into doped cladding layers of AlGaAs that act as waveguides for the vertical confinement of the emitted photons. They also present a ridge structure for the optical confinement in the horizontal direction, a $2 \div 5$ mm resonant cavity and electrical contacts used for the current injection. These devices can emit around 15 W, which corresponds to optical power densities exceeding $20\,\mathrm{MW/cm^2}$ at the semi-reflecting facets. These extremely high power densities may easily cause catastrophic optical mirror damage (COMD) unless preventive actions are taken to reduce the amount of defects and the absorption in the facet regions.

Several techniques can be used to increase the COMD threshold at the facet regions such as non-injected regions, careful passivation of the facets or non-absorbing mirrors (NAMs) realized by quantum well intermixing. This thesis focuses on the investigation of several approaches to integrate NAMs by compositional disordering, in particular impurity-free vacancy diffusion (IFVD) and impurity-induced disordering (IID), and eventually the evaluation of the NAM effect on the COMD threshold in a real fabrication process.

In order to investigate the quantum well intermixing, both experimental activity and modelling effort are required. Experiments have to be performed with several rapid thermal annealing (RTA) conditions and technological parameters, such as the thickness of the dielectric caps used to induce the compositional disordering, so that optimal process conditions may be determined. These conditions must then be properly adjusted to transfer the process from samples of $2\,\mathrm{cm^2}$ to whole 4-in (100 mm) wafers, while striving to maintain compatibility with the current production work-flow. The characterization of the process with a model is needed to have an insight in the comparison between the IFVD approach and the IID one.

This thesis is structured as follows:

Chapter 1 gives a brief explanation of semiconductor laser devices since the aim of the investigation was quantum well intermixing in high-power laser diodes

Chapter 2 details the different techniques to achieve compositional disordering reported in literature. Moreover the quantum well intermixing phenomenon is modelled with two

approaches: phenomenological and theoretical. The former determines the intermixed material profile through a comparison with the measured PL wavelength shifts while the latter is able to couple the vacancy profile with the disordering.

Chapter 3 explains the experimental activity carried out at the facilities of Prima Electro/Convergent Photonics in Turin and Chilab laboratory. Starting with the thermal stability of the InGaAs/AlGaAs material during RTA, several conditions of dielectric materials (thickness and pattern) and annealing (temperature and time) have been explored to determine optimal parameters compatible with an eventual complete fabrication process. The adjustments needed to transfer the IFVD technique to whole wafers have been determined. Finally a complete fabrication process has been performed in order to evaluate the performances of the intermixed diodes with those of the standard production. In this chapter a brief investigation of the intermixing caused by Ar bombardment is also reported.

Chapter 4 examines the IID process as an alternative to IFVD through the evaluation of the vacancy profiles. Moreover, details of an ongoing IID experiment are given.

Chapter 5 shows the main experimental results and a brief comparison with the state-of-art is made.

Chapter 1

High-power semiconductor lasers

Nowadays there are several applications in which laser devices are used, ranging from telecommunication to biomedical [1]. In particular, for industrial material processing applications [2], semiconductor laser diodes provide compact coherent light sources with high efficiency and high emitted optical power.

In this sector, high power semiconductor lasers have been realized in order to emit in the 900-980 nm region which allows the coupling with fiber laser as an optical pumping source. Typical laser diodes are realized with III-V semiconductors, in particular InGaAs/AlGaAs alloys. This kind of devices usually consists of edge emitting diodes controlled with a current injection and around 15 W can be obtained from a single emitter.

1.1 Basics of laser physics

Laser devices consist of a resonant cavity delimited by two semi-reflecting mirrors, one with high-reflectivity (HR-facet) and the other anti-reflective (AR-facet). The resonant cavity is realized with an active material that provides the optical amplification by exploiting the radiative electronic transitions. The mirrors establish a feedback mechanism inside the cavity where the generated light is subjected to amplification and reflections. The laser light emission is the fraction of light transmitted through the AR-facet.

1.1.1 Electronic transitions

The absorption and emission of photon are associated with electronic transitions between states in valence band (lower energy) $|1\rangle$ and conduction band (higher energy) $|2\rangle$. The photon energy is given by the separation between levels according to $h\nu = E_2 - E_1$. Three basic electronic transitions exist in a semiconductor material, schematically shown in fig. 1.2:

1. spontaneous emission

2. absorption

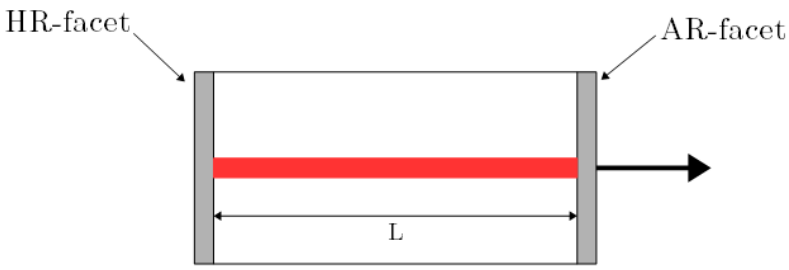

Figure 1.1: Schematic representation of a resonant cavity

3. stimulated emission

Spontaneous emission consists in the generation of a photon due to the recombination between an electron in conduction band (CB) and an hole in valence band (VB) without any interaction with already existing photons. This emission covers a whole spectra of wavelengths, one for each permitted electronic transition. Absorption, instead, is the excitation of an electron from VB to CB and the consequent generation of a hole in VB due to the interaction with a photon of proper energy. Stimulated emission requires the interaction between photons and electrons in CB, which induces the radiative recombination of the electron-hole pair. The emitted photon is characterized by the same wavelength, phase, polarization and propagation direction of the incident photon, therefore light amplification takes place in the material. This third kind of electronic transition is the mechanism that is exploited in laser devices. Obviously such process requires electrons already present in CB states in a condition called population inversion which can be realized either through carrier injection (commonly used in high-power laser diodes) or optically pumping the material (as in the case of optical fiber lasers). Thus population inversion is the fundamental requirement to have optical gain in an active material.

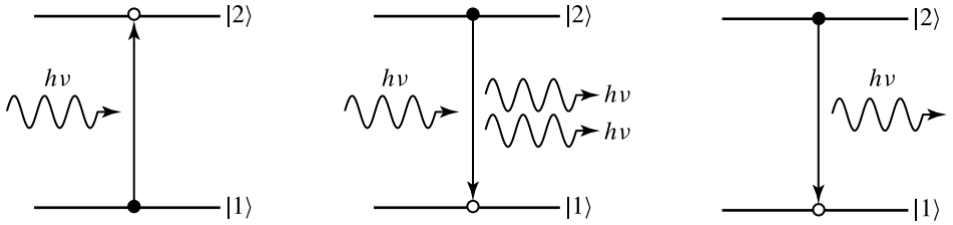

Figure 1.2: Electronic transitions [3]: (a) absorption, (b) stimulated emission and (c) spontaneous emission

The rates at which these radiative processes take place depend on the density of photons and the density of available state pairs between CB and VB.

Another possible electronic transition is the non-radiative recombination in which energy is dissipated through heat and no photon is generated. This mechanism is an unwanted defect in semiconductor lasers and in high-power devices it may lead to catastrophic optical damage.

1.1.2 Round-trip conditions

The active material is pumped to have population inversion, spontaneous emission takes place and a fraction of the radiation is guided along the longitudinal axis of the resonator. These photons are reflected at the facets and induce the stimulated emission of other photons and, once the amplification is able to compensate the intrinsic losses inside the material, it's possible to have laser emission. This is described by the laser round trip conditions.

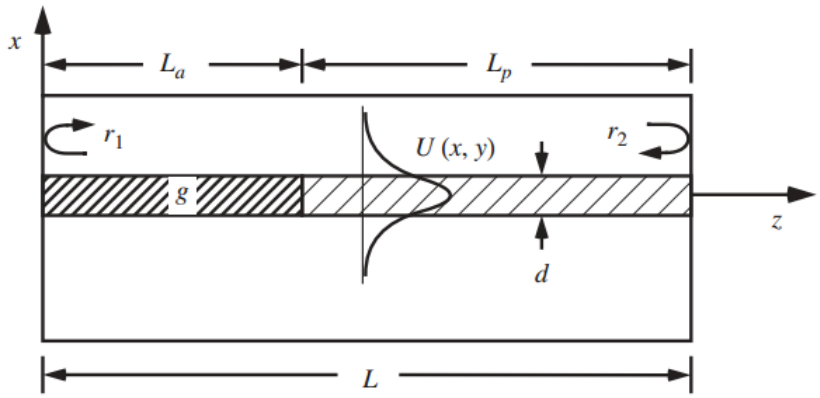

Figure 1.3: Generic laser cavity cross-section from [4]. L_a is the gain region, L_p the passive region

In a modern laser diode, the optical energy propagates in a dielectric waveguide mode, confined both in the lateral and trasversal direction, and described by normalized transverse electric field profile $E_0(x, y)$. The mode propagation can be expressed as [4]

$$\vec{E}_{TE} = \hat{y}E_0(x, y)\mathrm{e}^{\mathrm{j}\omega t} \cdot \mathrm{e}^{-\mathrm{j}\tilde{\beta}z} \tag{1.1}$$

where $\tilde{\beta}$ is the complex propagation constant, which includes any modal loss (α_i) or modal gain Γg which can be expressed as

$$\tilde{\beta} = \beta_r + \mathrm{j}\beta_i = \frac{2\pi n_{\mathrm{eff}}}{\lambda} + \frac{\mathrm{j}}{2}(\Gamma g - \langle\alpha_i\rangle) \tag{1.2}$$

where n_{eff} is the effective refractive index obtained by solving the Helmoltz equation for the waveguide refractive index profile. Assuming $L_p = 0$ (fig. 1.3) and facet reflectivities r_1, r_2, the condition for which the mode reaches threshold is that the gain compensate the losses as described by the Barkhousen conditions for a resonator

$$T = r_1 r_2 \cdot \exp\left(-2\mathrm{j}\frac{2\pi n_{\mathrm{eff}}}{\lambda}L\right) \cdot \exp\left(+[\Gamma g - \langle\alpha_i\rangle]L_a\right) = 1 \tag{1.3}$$

The Barkhausen condition are satisfied for

$$\angle T = 2m\pi \tag{1.4}$$

$$|T| = 1 \tag{1.5}$$

From the phase condition the cavity longitudinal modes λ_m can be derived:

$$2\beta_r L_a = 2m\pi \tag{1.6}$$

$$\lambda_m = \frac{2n_{\text{eff}}L_a}{m} \tag{1.7}$$

while from the gain condition the threshold gain $\Gamma g_{\text{th}}$is obtained

$$r_1 r_2 \exp([\Gamma g - \langle\alpha_i\rangle]L_a) = 1 \tag{1.8}$$

$$\Gamma g_{\text{th}} = \frac{1}{L_a}\log\left(\frac{1}{r_1 r_2}\right) + \langle\alpha_i\rangle = \alpha_m + \langle\alpha_i\rangle \tag{1.9}$$

with mirror loss α_m and average internal loss $\langle\alpha_i\rangle = \alpha_m + \langle\alpha_i\rangle$.

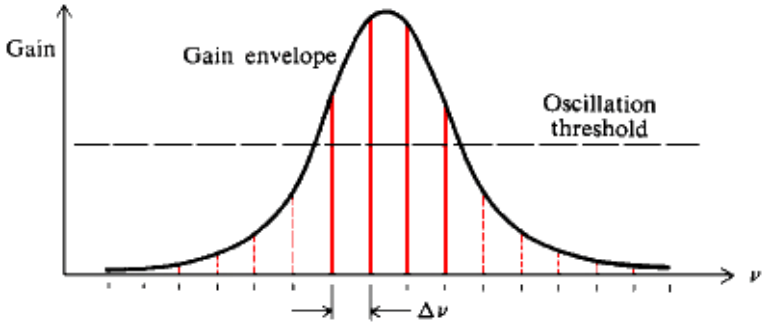

Figure 1.4: Threshold gain from http://laserstars.org

1.2 Semiconductor lasers

Semiconductor materials present at 0 K two bands, one completely filled (valence band, lower energies) and the other completely empty (conduction band, higher energies) of electrons separated by an energy gap around 1 eV. At room temperature, part of the conduction band is populated by electrons leaving holes in valence band. This energy structure makes possible both the population inversion and the stimulated emission.

In order to increase the probability of radiative electron-hole pair recombination and, therefore allowing the laser diode to sustain the photon emission, the semiconductor material must have a direct band gap in which the recombination process doesn't require the interaction with photons.

1.2.1 Double heterostructures

In order to optimize the stimulated emission probability, a direct-gap semiconductor material must be used and both high carrier density and high photon densities are needed. Moreover, since carriers are constantly recombined during stimulated emission, a mechanism to replenish the electron population in CB is necessary. Therefore a proper *pin* junction that allows the confinement of both carriers and photons is used (fig. 1.6).

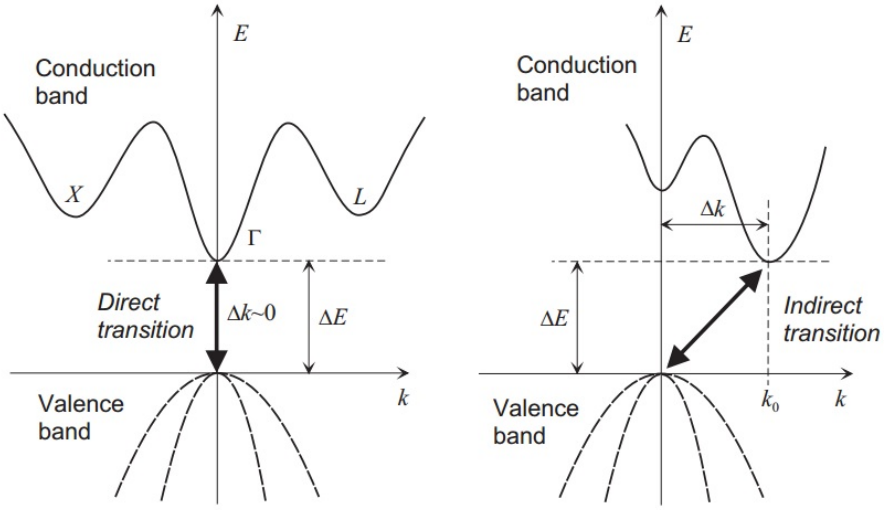

Figure 1.5: Direct and indirect semiconductor bandgaps [5]

In *pin* junctions population inversion can be maintained using the diode in forward bias through carrier injection. In particular the probability of stimulated emission can be described using electrons and holes Fermi distributions ($f_c(E,T)$, $f_v(E,T)$) and quasi-Fermi levels E_{F_c}, E_{F_v}:

$$f_c = \frac{1}{1+\exp\left(\frac{E_2-E_{F_c}}{k_BT}\right)}$$
$$f_v = \frac{1}{1+\exp\left(\frac{E_1-E_{F_v}}{k_BT}\right)}$$

The stimulated emission process should be predominant with respect to absorption so

$$R_{\text{stim}} - R_{\text{abs}} = f_c(1-f_v) - f_v(1-f_c) = f_c - f_v > 0$$

$$\begin{aligned} f_c &> f_v \\ E_2 - E_{F_c} &< E_1 - E_{F_v} \\ E_g &= E_2 - E_1 \\ E_g &< h\nu \end{aligned}$$

The population inversion is reached when the quasi Fermi levels $E_{F_c}$and E_{F_v} penetrate in CB and VB. Therefore to have stimulated emission the following relation has to be respected:

$$E_g < E_{F_c} - E_{F_v}$$

The materials used are III-V compounds, shown in fig. 1.7 that are compatible with semiconductor substrates such as GaAs or InP and provide the wavelength needed for the specific application, for example 1.3 µm and 1.55 µm in optical communications and

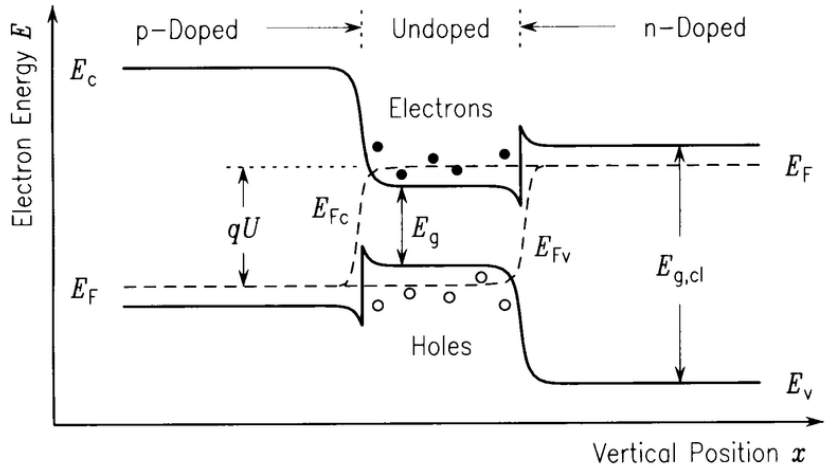

Figure 1.6: Example of double heterostructure [6]

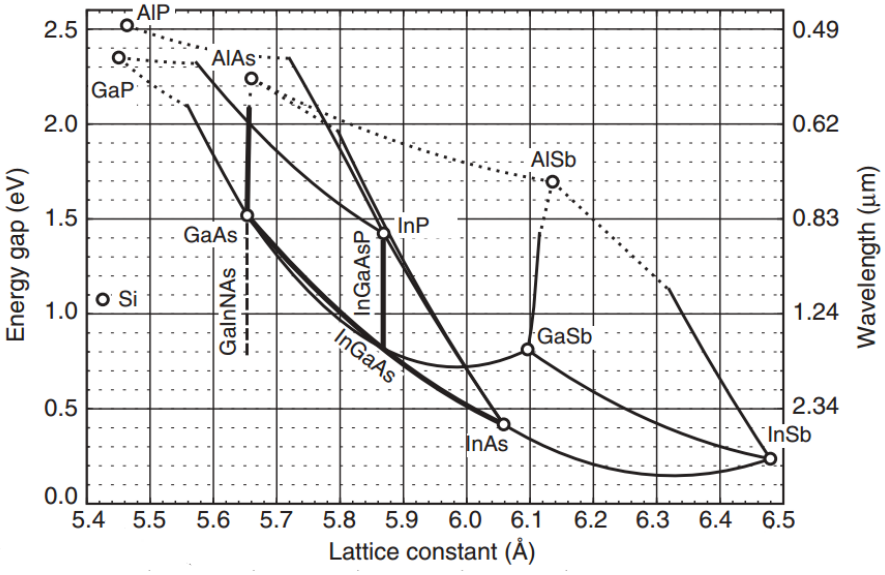

Figure 1.7: Semiconductor alloy diagram [4]. The structure is realized in AlGaAs/GaAs but, to be able to optically pump the fiber laser, the quantum well consists of a single layer of InGaAs which provides the proper wavelength.

$900 \div 980$ nm in material processing. Moreover these compounds can be used to fabricate structures to spatially confine both photons and carriers thus controlling also the optical properties of the semiconductor.

Carrier confinement is obtained realizing a quantum well, a double heterostructure of thickness comparable with the electronic wavelength. These heterojunctions use cladding regions with higher bandgap as potential barriers, while the well itself has lower gap. In

this way the electronic wave is confined in the well ad its energy levels become quantized as shown in fig. 1.8.

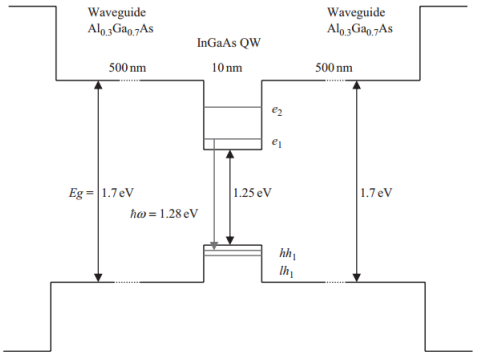

Figure 1.8: Band gap distribution and relevant energy levels of an InGaAs-QW embedded in a AlGaAs waveguide layers from [7]

Quantum wells are fundamental to increase the efficiency of semiconductor laser diodes since they allow to reach the same population inversion with a smaller number of the injected electrons than for the bulk semiconductor and heavily modify the density of states (DOS) with respect to bulk materials (fig. 1.9).

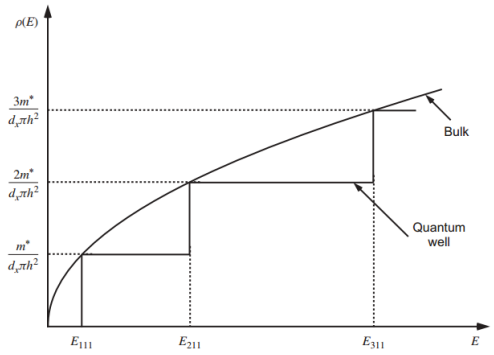

Figure 1.9: Comparison of DOS between bulk semiconductor and infinite-barrier quantum well [4]

From the strong carrier confinement and the joint-density-of-states given by quantum wells, the laser diodes have several other advantages such as lower laser threshold, high thermal operation, high differential gain, wide gain bandwidth. If the quantum well is realized with layers that induce compressive strain in the structure, the diode has also low thermal dependence (high T_0). Finally quantum wells also allow to tune the emission wavelength of the laser by properly modifying the energy levels.

The optical confinement provides the high photon density needed for the laser diode and it's realized with a separate confinement heterostructure (SCH) different in the vertical direction and a waveguide in the horizontal direction. The characteristic dimensions of these waveguides are much larger than the quantum well thickness, being the optical wavelength

longer than the electronic one.

On the horizontal direction, the waveguide is fabricated with a ridge structure in which a chemical etch process is used to remove part of the material, thus introducing a significant refractive index variation $n(z)$. On the vertical direction, instead, the index guiding is realized with layers having different refractive indices between one another. The vertical waveguide is realized during the epitaxial growth using III-V compounds but with different molar fractions in each layer. Both lateral and vertical confinement are schematically represented in fig. 1.10.

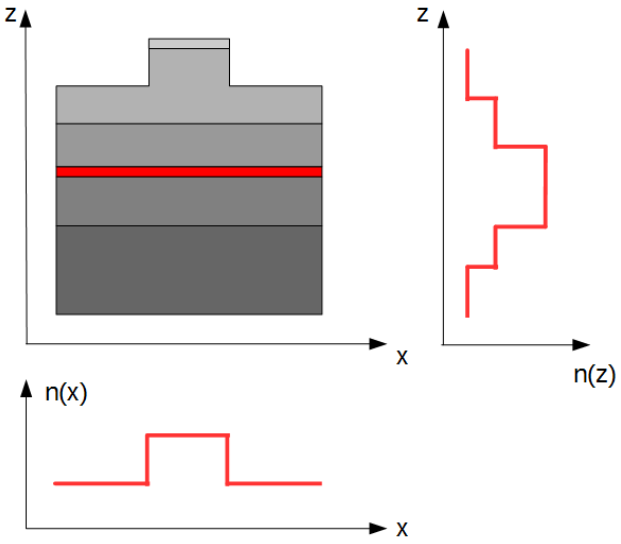

Figure 1.10: Optical confinement with ridge structure

1.2.2 High-power laser diodes

High-power laser diodes are a particular class of semiconductor lasers that are characterized by high output optical power and high brightness. They are fabricated in III-V compounds, usually InGaAs/AlGaAs alloys, and present a single quantum well which emits in the range $900 \div 980$ nm.

This class of diodes is able to emit tens of watt of output power and their main application is the optical pumping of fiber lasers that are able to reach kilowatts of power, making them particularly suitable for material processing. In addition to optimum optical and electrical performance, the thermal behaviour is extremely important in high-power laser diodes, so they must have:

- low optical losses,
- high internal and external efficiency,
- optimum facet coating,
- low operating voltage,

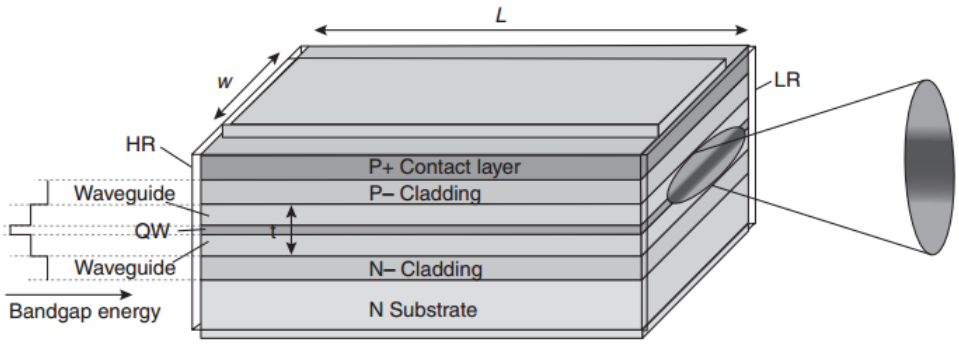

Figure 1.11: An example of high power laser diode from [8]

- efficient heat dissipation,
- high temperature performance.

Beam quality

Another important parameter for high-power laser diodes is their beam quality, which is characterized by the Beam Parameter Product (BPP), and their brightness.

The BPP is calculated from the far-field divergence angle and the beam radius according to

$$\mathrm{BPP} = w \cdot \theta \quad (\mathrm{mm} \cdot \mathrm{mrad})$$

where w is half beam width and θ is its angular semi-divergence, both measured at the output mirror of the laser diode. The BPP cannot be reduced by manipulating the beam with linear optics. Another parameter evaluating the beam quality is the beam quality factor M^2 which compares the the optical beam with a gaussian one, that is characterized by the best possible BPP:

$$\mathrm{BPP}_{\mathrm{Gauss}} = \frac{\lambda}{\pi}$$
$$M^2 = \frac{\mathrm{BPP}}{\mathrm{BPP}_{\mathrm{Gauss}}} \geq 1$$

For asymmetric beams, the M^2 factor can be significantly different in the two orthogonal directions. In fact, in edge-emitting semiconductor lasers the waveguide in the transverse direction (normal to the growth plane) is single-mode, resulting in a very low M^2 (fast axis). While the waveguide in the lateral direction (slow axis) is large, and highly multimode.

Another important parameter is the brightness B which also is related to the BPP

$$B = \frac{P_{\mathrm{opt}}}{\pi^2 \mathrm{BPP}^2} = \frac{P_{\mathrm{opt}}}{\pi^2} \cdot \left(\frac{1}{w\theta}\right)^2 \quad \left(\mathrm{W\,cm^{-2}\,sr^{-2}}\right)$$

This parameter is proportional to the material processing efficiency, so an higher value of B is desirable which, in turn, means the BPP should be as small as possible.

Fiber laser

Material processing requires powers of the order of kW so single laser diodes with optical power around tens of W cannot be directly used. However coupling many diodes increases the total BPP since $\mathrm{BPP}_{\mathrm{tot}} \approx \sum_i \mathrm{BPP}_i$ thus preventing their direct use in this application. Due to this limitation, laser diodes are typically used as pump sources for rare-earth-doped fiber lasers which, in turn, deliver the required optical power at low BPP at the expense of optical power loss around 30%.

Figure 1.12: Example of multiemitter module

The optical pumping is realized by an array of multiemitter modules (an example is shown in fig. 1.12), each consisting of several 920 nm laser diodes whose output beams are coupled with a multimodal coupler. This incoherent superposition increases significantly the BPP, thus degrading the beam quality, but the resulting output beam has elevated optical power, around 1.6 kW. The photons from the multiemitter array are injected into the active fiber to excite ytterbium ions to metastable states.

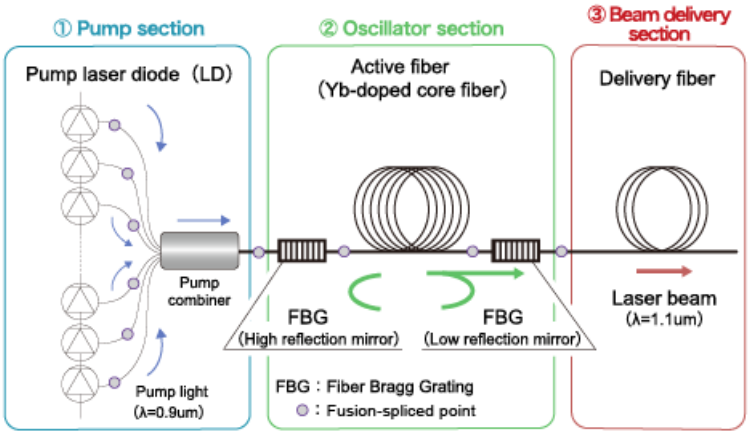

Figure 1.13: Schematic representation of a fiber laser system from www.fiberlaser.fujikura.jp

The active fiber is a ytterbium-doped resonator that amplifies light by stimulated emission. The optical confinement is realized by the difference in the refractive index between core and cladding layers of the fiber itself and the resonant cavity is formed with Bragg reflectors. The fiber laser acts as a BPP converter since, differently from the pumping system, it's characterized by low BPP, high brightness, power around 1 kW and emission wavelength at 1050 nm.

Therefore the fiber laser system, schematically shown in fig. 1.13, can be used in material processing for applications such as laser cutting, drilling, welding, additive manufacturing and it can be even used in biomedical applications.

COMD and NAM

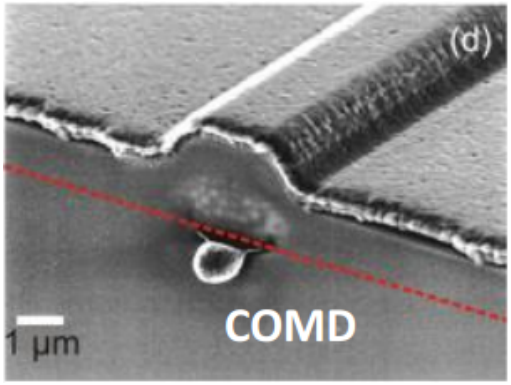

(a) COMD observed with SEM. It's evident the melting of the facet.

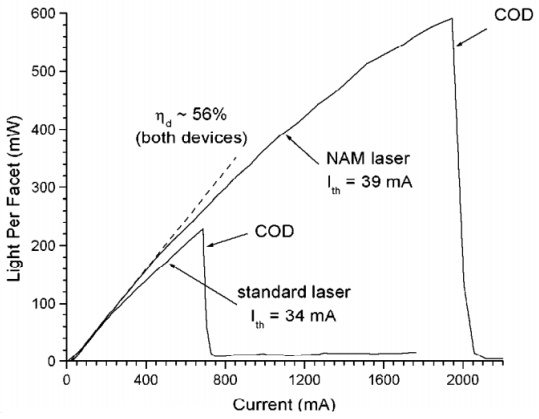

(b) Typical COMD in L-I-V measures [9]

Figure 1.14: Catastrophic Optical Mirror Damage (COMD)

Three main failure mechanisms [10]–[13] can be observed in high power laser diodes:

- rapid degradation of the output power due to significant defects already present after the device fabrication;
- gradual degradation which consists of a slow output power decrease due to creation and diffusion of point defects;
- sudden degradation in which the output power drops instantly after reaching a threshold condition (fig. 1.14).

The catastrophic optical mirror damage (COMD) belongs to the third group and it's characterized by a fast thermal runaway due to excessive non-radiative recombination at the diode facets in a positive feedback mechanism. At high power the mirror tends to overheat and the optical absorption increases significantly, thus causing localized heating. This, in turn, leads to a reduction in the material bandgap and consequent increase of the absorption at the emission wavelength. This mechanism causes the thermal runaway that leads to the facet melting. So in high-power laser diodes, which can emit power densities exceeding 20 MW/cm^2, any defect can easily induce COMD [10], [11], [14] and

proper preventive actions must be taken in order to increase the COMD threshold. To do so several approaches have been reported in literature:

- better facet passivation that reduces the defects acting as recombination centers;
- non-injected regions at the facets that reduce the non-radiative recombinations;
- deposition of $\lambda/4$ layers on the HR facet that shift the optical standing wave pattern in order to have a minimum of the intensity at the facet [15], [16];
- realization of non-absorbing mirrors (NAMs) [9], [17] through quantum well intermixing.

The first one can be carried out, for example, by cleaving the diodes under vacuum or with proper facet treatments, the third one consists in the deposition of a suitable multilayer stack of dielectrics, while the forth one is the approach that has been investigated in this work.

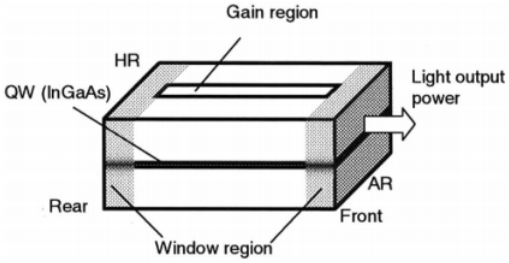

Figure 1.15: Schematic of laser diode with NAM regions [18]

Non-absorbing mirrors (NAMs) consist of a window structure [18]–[20] near the facets where the bandgap is higher with respect to the cavity. These passive waveguides can be realized by etching and regrowing the epitaxial layers but this approach requires the equipments needed for an epitaxial growth (such as MBE or MOCVD reactors) and can introduce a mode mismatch at the butt joint or other defects. The quantum well intermixing technique, instead, creates and diffuses vacancies inside the crystalline structure to induce compositional disordering in the region. This, followed by a rapid thermal annealing process, results in an higher bandgap while preserving the alignment with the active waveguide. Moreover the variation of refractive index at the butt joint can be made negligible thus reducing the mode mismatch.

Chapter 2

Quantum well intermixing

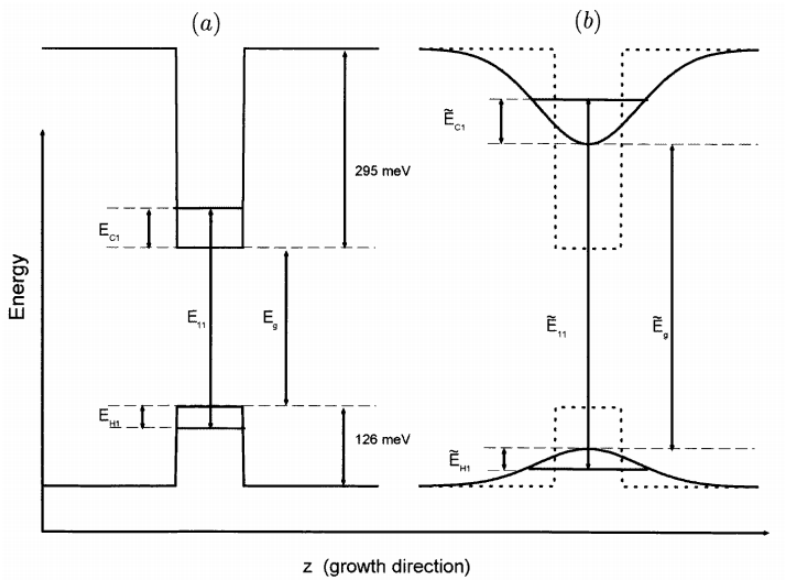

Figure 2.1: Example of compositional disordering in AlGaAs [21]

The quantum well intermixing (QWI) is a post-growth technique to modify the potential profile of a quantum well by the compositional disordering of the barrier-well interface therefore changing the quantized energy states. This allows, in principle, the integration of a variety of devices [22]–[25] such as passive waveguides, modulators [26], [27], photodetectors [28] and can be even used to tune the emission wavelength of a laser diode [29]–[32]. In the case of InGaAs/AlGaAs high power laser diodes, the most interesting aspect of this technique is the possibility to integrate non-absorbing mirrors (NAMs) at the facets of the diode itself.

The QWI process takes place through the diffusion of III-group vacancies across the epi-structure in such a way to realize the compositional disordering. This leads to the modification of the quantum well profile and the change of its bound states (fig. 2.2), the increase of energy gap and, in extreme cases, the reduction of the potential barriers. In this

way it's possible to make transparent the facet regions by reducing their absorption at the emission wavelength.

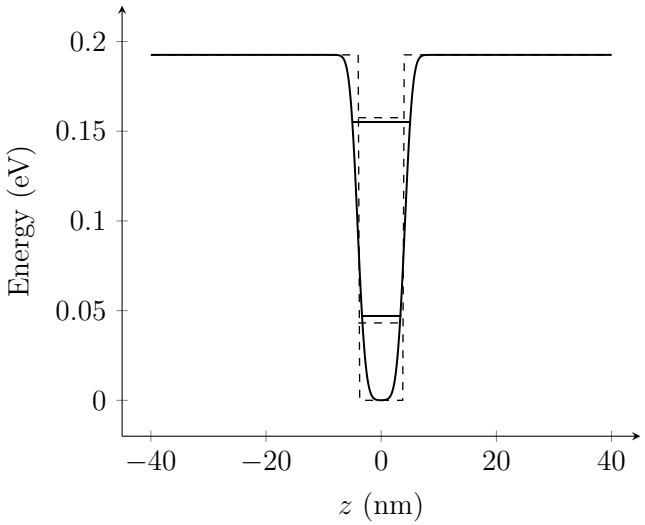

Figure 2.2: Effect of QWI on a rectangular quantum well. It's possible to notice a shift in the bound state energies between the two wells

Several techniques can be used to induce the compositional intermixing, each with its own advantages and weaknesses. The most commonly used are impurity-free vacancy diffusion (IFVD), impurity-induced disordering (IID), Ar^+ plasma bombardment and laser-induced intermixing. In the following sections each of them is presented more in detail.

2.1 Impurity-free vacancy diffusion (IFVD)

The impurity-free vacancy diffusion (IFVD) is perhaps the simplest technique to enhance the intermixing of the quantum well and it requires the deposition of dielectric cap layers on the sample surface [33]. The mechanism of compositional disordering is the generation and subsequent diffusion of vacancies due to the out-diffusion of III-group atoms from the material into the dielectric cap during a rapid thermal annealing (RTA).

Choosing the proper dielectric or its stoichiometry it's possible both to suppress or enhance the intermixing, allowing also a certain degree of spatial selectivity in tuning the bandgap [34].

In literature the most reported dielectrics are:

- SiO_xN_y layers [35]–[39], in which the Ga concentration increases with the oxygen content thus increasing also the intermixing;
- Si_3N_4 that tends to suppress the intermixing [40]–[42];
- SiO_2 that enhances the intermixing [40], [43]–[48]. Depending on the deposition technology, the annealing temperature needed to achieve a significant intermixing ranges from 660 °C to 950 °C. In particular sputtered SiO_2 has the lowest requirements

for the temperature due to the increase in the vacancy concentration given by the sputtering process itself;

- SrF_2 that inhibits the intermixing [45], [49]–[51] more efficiently than Si_3N_4.

The observed intermixing depends on the encapsulating dielectric, its properties (thickness and porosity), and stress at the cap/semiconductor interface due to difference in their thermal expansion coefficients [52]. In fact Si_3N_4 and SiO_2 layers can be used to respectively enhance or inhibit the intermixing in AlGaAs alloys due to the stress they cause on GaAs: if tensile (Si_3N_4) the vacancies are trapped closer to the surface. Another factor in the amount of intermixing is the diffusion coefficient of Ga into the dielectric: in the case of SiO_2 caps the diffusivity is one order of magnitude greater than in Si_3N_4 layers.

The properties of the encapsulating dielectric layer may be varied with different deposition conditions [53] or growth techniques such as sputtering [24], [54], evaporation or plasma enhanced chemical vapour deposition (PECVD). This degree of freedom also affects the required annealing temperatures that range from 660 °C to 950 °C; however such high temperatures may also damage the material itself.

Besides its simplicity, another advantage of IFVD is the low defect density it generates, thus maintaining high crystal quality and low propagation losses. The main weakness of IFVD, instead, is the management of the different thermal expansion coefficients of the involved materials. If not properly considered it's possible to observe delamination or reduced efficiency after the RTA [47], [49].

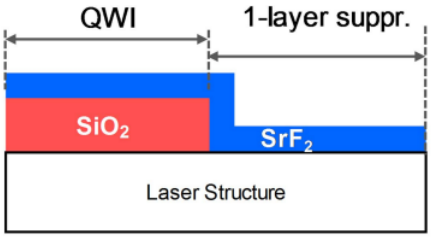

Figure 2.3: Example of IFVD structure [49]

2.2 Impurity-induced disordering (IID)

The impurity-induced disordering (IID) consists in the implantation of neutral or electrically active atomic species such as As^+ or H^+ followed by rapid thermal annealing in order to realize the compositional intermixing. This technique can become impurity-free if the implanted element is already present in the crystalline matrix.

The parameters of this technique are implanted species, ion energies and doses [30], [52], [55]. Usually highly energetic ions are used in order to reach the depth at which the quantum well lies, thus the facilities needed for such a process aren't neither readily available nor common. However, the ion implantation is a well established technique in the field of semiconductor devices and allows a very good spatial selectivity and control. An issue that may arise is the crystal damage that may introduce defects acting as recombination centers thus countering the effects of NAMs.

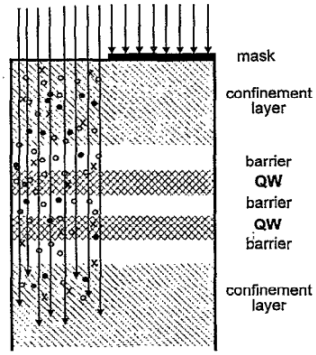

Figure 2.4: Example of IID process. The implantation range allows to generate vacancies close to the quantum well layer.

Depending on doses and ion energies, the annealing temperatures required to have an efficient disordering range from 700 °C to 950 °C. In principle, if the vacancies are generated in close proximity to the quantum well layer, the required temperatures can be significantly lower with respect to the IFVD approach, thus overcoming the extremely small vacancy diffusivity in III-V compounds for $T < 850\,°C$. This, however, may require the use of highly energetic ions and, depending on the ion species itself, they may cause excessive crystal damage.

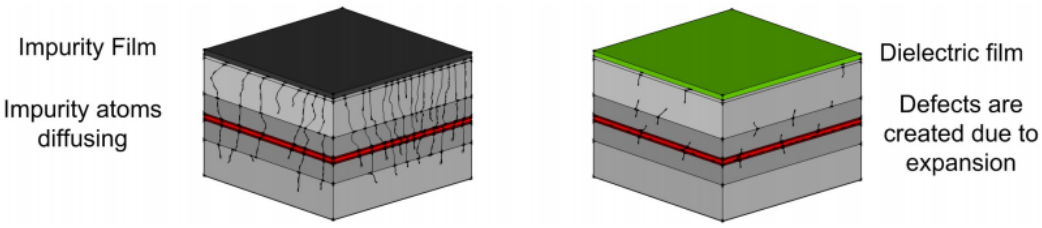

Figure 2.5: Comparison between IID and IFVD [32]. Being the IID vacancies much closer to the quantum well with respect to IFVD, the annealing temperature can be significantly lowered.

In literature several ions have been reported:

- electrically active species such as fluorin and boron [56]–[62] which may introduce non-radiative defects in the NAM;
- ions belonging to the material matrix such as arsenic in AlGaAs [63]–[66] that make this approach impurity-free. However, using such heavy ions requires energies of the order of 1 MeV or higher in order to reach the quantum well layer, thus possibly causing the amorphization of the material;
- light ions, in particular protons [67]–[71], that can reach the quantum well with lower energies but are unable to generate the same amount of vacancies as heavier ions.

2.3 Ion bombardment

The ion bombardment can be considered a variant of the IID technique since it uses low-energy ions to create vacancies near the material surface that are subsequently diffused during RTA. This approach promises to reduce the unrecoverable crystalline damage of the material with respect to ion implantation (which may require energies of MeVs).

Several possibilities exists for this technique: H_2 plasma [72] or Ar plasma (usually obtained in a ICP-RIE) [73]–[84].

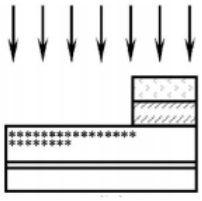

Figure 2.6: Example of Ar^+ plasma exposure [81]

2.4 Photoabsorption-induced disordering (PAID)

The photoabsorption-induced disordering exploits the light absorption in the quantum well region when the material is excited with a proper wavelength. In this way it's possible to have a localized heating that leads to the intermixing.

This technique can be used both with continuous wave (CW) and pulsed lasers (p-PAID) and it's reported to be really effective in InGaAsP semiconductors due to their limited thermal stability. However, the main issue is the need for a laser with the appropriate wavelength to induce the heating. Moreover this approach requires the etching of the top absorbing layers of the epi-structure. [22], [85]–[98]

2.5 Numerical modelling

Quantum well intermixing can be evaluated through numerical models that can be divided between a more phenomenological approach and a more theoretical one. The former assumes a certain distribution of the compound atoms (usually for the IFVD) [99], while the latter solves numerically the diffusion of the III-group vacancies (usually IID) [100]. However, both approaches share a few elements, in particular they assume that the III-group vacancy diffusion is described by Fick's law and both require the solution of Schrödinger equation for a finite potential well.

In the following, both the compositional intermixing and the bound state evaluation will be treated more in detail, and the result of a simple phenomenological model will be explained. Also a theoretical model, developed with the help of Prof. Amr Helmy from University of Toronto, will be illustrated. These models make use of experimental results that will be treated in chapter 3.

2.5.1 Compositional intermixing

The cause of quantum well intermixing is the generation and diffusion of III-group vacancies during RTA, so the profile of each diffusing element can be obtained solving the so-called second Fick law [101]

$$\frac{\partial}{\partial t}C(z,t) = \frac{\partial}{\partial z}\left(D\frac{\partial}{\partial z}C(z,t)\right) \tag{2.1}$$

where $C(z,t)$ is the concentration of diffusing atoms and D is their diffusion coefficient. Assuming that D doesn't depend on the concentration nor on position, eq. (2.1) can be simplified to

$$\frac{\partial}{\partial t}C(z,t) = D\frac{\partial^2}{\partial z^2}C(z,t) \tag{2.2}$$

Assuming infinitely thick barriers, the solution of eq. (2.2) is given the sum of erf functions [101]

$$C(z,t) = \frac{1}{2}\left(\operatorname{erf}\left(\frac{z-d}{\sqrt{4D_{\text{III}}t}}\right) - \operatorname{erf}\left(\frac{z+d}{\sqrt{4D_{\text{III}}t}}\right)\right) \tag{2.3}$$

where D_{III} is the diffusion coefficient of III-group atoms (Ga, Al, In). Equation (2.3) can be directly applied to the intermixing in GaAs/AlAs heterostructures while, in the case of the $In_{1-x}Ga_xAs/Al_{1-x}Ga_xAs$ heterostructure used in this thesis, both the diffused molar fraction of Al and Ga are assumed to be related to eq. (2.3) according to

$$C_{\text{Ga}}(z,t) = x_{\text{well}} \cdot C(z,t) + x_{\text{barrier}} \cdot (1 - C(z,t)) \tag{2.4}$$
$$C_{\text{Al}}(z,t) = y_{\text{well}} \cdot C(z,t) + y_{\text{barrier}} \cdot (1 - C(z,t)) \tag{2.5}$$

The diffusion coefficient D_{III} is assumed to be the same for both species thus implying the lattice matching of the diffused quantum well.

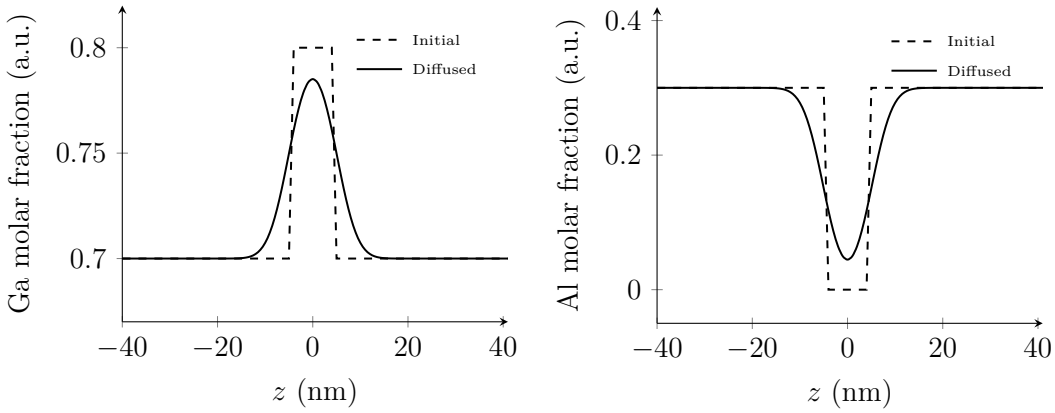

(a) Ga molar faction

(b) Al molar fraction

Figure 2.7: Example of compositional disordering with $D_{\text{III}} = 1 \times 10^{-15}\,\text{cm}^2/\text{s}$ at 950 °C for 60 s

From these equations it's possible to evaluate both the band diagram and the effective masses of electrons, heavy and light holes [102] needed to determine the bound states of the well.

So, given an initial molar fraction distribution of both Al (y) and Ga (x), intermixing takes place according to a common diffusion coefficient D_{III} for the III-group atoms of the compound. Since the intermixed alloy is $\text{In}_{1-x-y}\text{Ga}_x\text{Al}_y\text{As}$ it's possible to obtain also the molar fraction of In $(1-x-y)$. The diffusion coefficient D_{III} is assumed to not depend on position or concentration but no hypothesis was made on its dependence on time.

2.5.2 Evaluation of the bound states

The bound states of an arbitrary-shaped quantum well can be obtained solving the stationary Schrödinger equation

$$-\frac{\hbar^2}{2}\frac{\partial}{\partial z}\left(\frac{1}{m^*(z)}\frac{\partial\psi(z)}{\partial z}\right)+V(z)\psi(z)=E_n\psi(z) \tag{2.6}$$

were $V(z)$ is the potential profile, $m^*(z)$ is the effective mass and E_n the bound state energies.

To solve eq. (2.6) for an arbitrary-shaped quantum well several numerical methods are available, for example Runge-Kutta-type algorithms (RK) [45], [103], [104], finite differences (FDM) [105], finite elements (FEM) [106]–[111], transfer matrices (TFM) [112], [113] or even iterative techniques [114]. In this study the FEM procedure was used to solve the generalized eigenvalue problem derived from the weak formulation of eq. (2.6) (as shown in appendix B). Being a variational method, a known weakness of this technique is gradual loss of accuracy for higher eigenvalues. However, comparing the results of the FEM solver with those of a few test cases, this error was deemed acceptable. Finally each test case has been compared with the results obtained using the transfer matrix method and, in all cases, the difference between the two methods (FEM and TFM) was negligible.

Parabolic QW

The bound state energies of an infinite parabolic quantum well (or, equivalently, an harmonic oscillator) are given by

$$E_n=\hbar\omega\left(n+\frac{1}{2}\right)$$

with $n=0,1,\ldots$. So these states are all equally spaced in energy $E_{n+1}-E_n=\hbar\omega/2$.

Using a parabolic potential the stationary Schrödinger equation eq. (2.6) was solved and the resulting energies were properly spaced within 10^{-5} eV for the highest eigenvalues.

Rectangular QW

Another test case consisted of two rectangular quantum wells made by $\text{Al}_{0.2}\text{Ga}_{0.8}\text{As}/\text{GaAs}$ of width, respectively, 20 nm and 2 nm.

Even though the highest eigenenergies slightly differed from the expected values, the bound states evaluation was deemed satisfactory since, in high-power laser diodes, the optical transition of interest is the fundamental one between electrons and heavy holes.

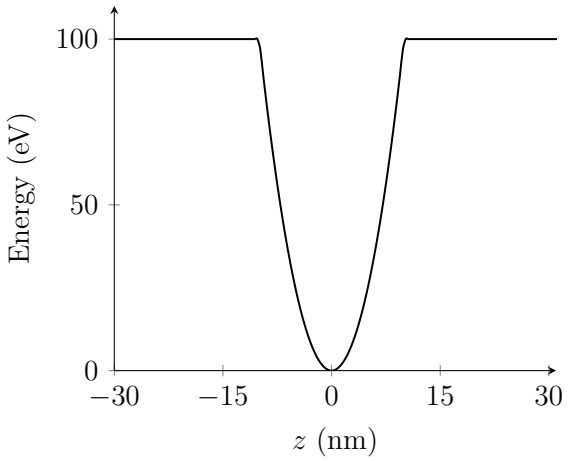

Figure 2.8: Parabolic quantum well

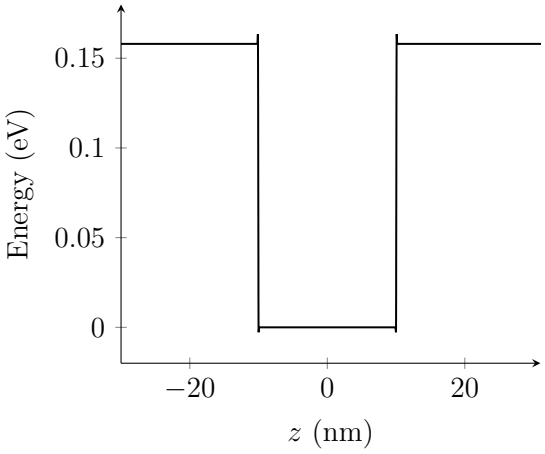

Expected (eV)	FEM (eV)
0.01400	0.01400
0.04109	0.04109
0.08998	0.08998
0.14866	0.14866

Table 2.1: Potential profile of 20 nm quantum well and its bound states

Intermixed QW

Finally an intermixed structure defined using eqs. (2.3) and (2.4) was used in the FEM solver to evaluate its capability to solve arbitrary-shape quantum wells with position-dependent effective mass.

The considered quantum well is represented in fig. 2.9 and is obtained with a diffusion coefficient $D_{\text{III}} = 10^{-15}\text{cm}^2/\text{s}$ and RTA 950 °C, 60 s. Its bound state energies were evaluated to be 83 meV and 152 meV, the corresponding wavefunctions are shown in fig. 2.9b. The comparison of these results with those obtained using the transfer matrix method was considered satisfactory.

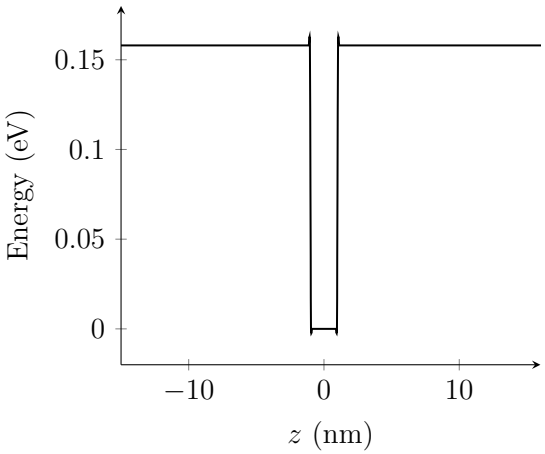

Expected (eV)	FEM (eV)
0.12706	0.12706

Table 2.2: Potential profile of 2 nm quantum well and its bound states

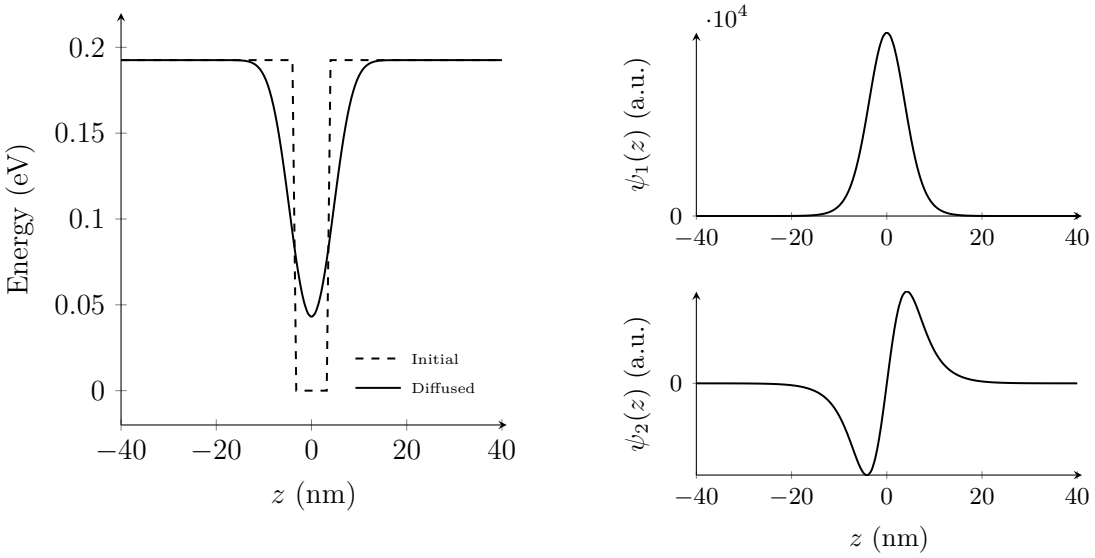

(a) Intermixed quantum well

(b) Wavefunctions

Figure 2.9: Intermixing with $D_{\text{III}} = 10^{-15}$ cm^2/s and RTA 950 °C, 60 s

2.5.3 Phenomenological model

This approach assumes, as previously explained, that the diffusion of III-group atoms is given by eq. (2.4) and was originally used only to characterize intermixing experiments in terms of diffusivity of Al atoms [45] or Ga vacancies [115]. However, carrying out several experiments, this method can be used to extrapolate a "calibration curve", shown in fig. 2.11, which gives a limited predictive capability.

Another assumption is that the lattice matching is conserved after the annealing, meaning there is a single diffusion coefficient D_{III} for all atomic species [116]. A more rigorous approach

would be to consider different diffusivities for each element thus introducing also the effect of strain [117]–[119].

Algorithm

This model requires wavelength shifts from a series of experiments in order to determine iteratively a diffusion coefficient for the quantum well. The only requirement is the knowledge of both initial molar fraction and functional form of the diffused molar fraction.

The initial quantum well is realized with $Al_{1-x}Ga_xAs$ barriers while the well itself is made by $In_{1-x}Ga_xAs$ in order to obtain an emission wavelength compatible with the optical pumping of the fiber laser. The diffused profile is evaluated according to eq. (2.4).

So the main steps of the algorithm are:

1. Measure of $\Delta\lambda_{\text{exp}}$ from PL
2. Assume D_{III} and evaluate the intermixed profile
3. From the molar fraction evaluate the band diagram
4. Evaluate the $\Delta\lambda_{\text{num}}$ of the intermixed quantum well with respect to the initial quantum well
5. Compare $\Delta\lambda_{\text{exp}}$ and $\Delta\lambda_{\text{num}}$, if they differ more than a certain convergence threshold assume a new D_{III} and repeat.

Numerical issues

From the numerical point of view, the main issues are the order of convergence and the threshold. The former is therefore related to the computational time, while the latter depends on the accuracy of the PL measures and on the computational time.

The original paper [45] used a simple loop in which the diffusivity D is increased by small steps until $|\lambda_{\text{exp}} - \lambda_{\text{num}}| \leq 0.2$ nm. However, this approach may extremely increase the time to reach convergence if the step is too small or it may even fail to converge if the step is too large. However, if the method is evaluated as a root-finding problem using as threshold $|\Delta\lambda_{\text{exp}} - \Delta\lambda_{\text{num}}|$, where each $\Delta\lambda_{\text{num}}$ is computed with respect to the initial quantum well, it's possible to use numerical techniques such as bisection or secant method to increase significantly the order of convergence. Finally it was used a false position method which has higher convergence order with respect to bisection while maintaining the properties of a bracketing method.

The threshold value is related to the PL measurement accuracy (1 nm), so any threshold less or equal than the accuracy can be used without introducing a significant error. Moreover the threshold also affects the computational time but its impact becomes negligible when root-finding algorithms are used.

Temperature and time dependence

The main parameter of this model is the diffusion coefficient D_{III} but its dependence on time and temperature was not known. So a group of samples, each annealed at different

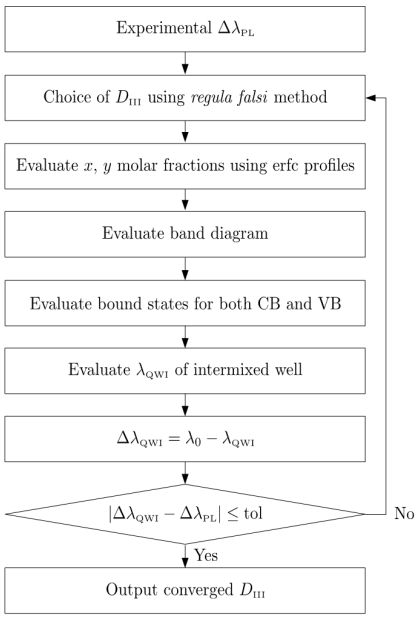

Figure 2.10: Schematic representation of the algorithm

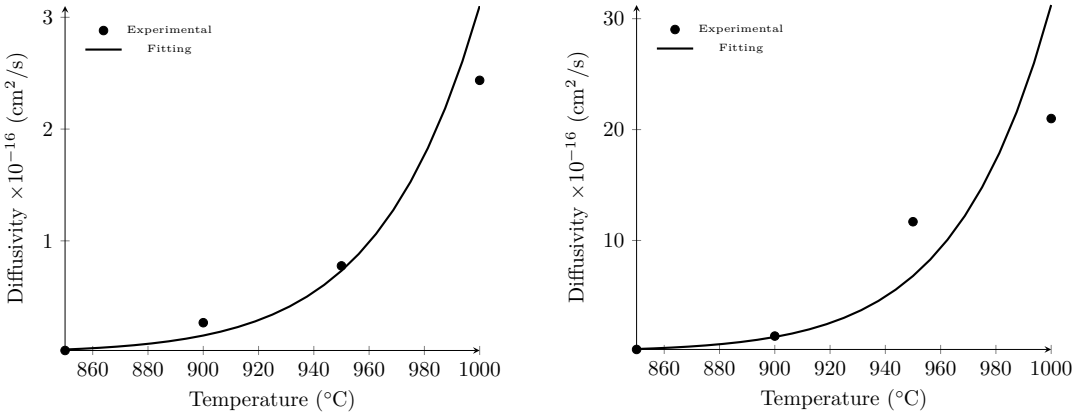

(a) Si_3N_4 samples (b) SiO_2 samples

Figure 2.11: Diffusivity in samples annealed for 1 minute

temperatures and times, were prepared using the SiO_2-over-Si_3N_4 dielectric structure, explained in chapter 3.

As seen in fig. 2.11, the diffusion coefficient D_{III} presents an exponential behaviour for samples annealed between 850 °C and 1000 °C for 1 minute. Moreover the SiO_2 diffusivity is one order of magnitude greater than the Si_3N_4 one as expected from the enhancement or suppression of the intermixing.

For what concerns the time dependence, instead, the amount of intermixing $\Delta\lambda$ increases almost linearly with time, meaning the diffusivity is nearly independent from time as shown in table 3.6.

Validity

This modelling approach is extremely simple and, given a sufficient number of comparable samples, it should be possible to predict the observed $\Delta\lambda$. Moreover, being so simple, it can be used both for IFVD and IID but it cannot give any insight about the vacancy profile.

2.5.4 Theoretical model

The quantum well intermixing can be also described with more theoretical approaches, in particular [99], [120], [121]. These models couple the vacancy profile with the compositional disorder and, therefore, with the wavelength shift of the quantum well. They can be applied both to the IFVD and the IID process but require some knowledge of the material properties.

From the physical point of view, the intermixing process can therefore be described as the diffusion of both vacancies and III-group atomic species, each with their own diffusion coefficient D_{Ga}, D_{Al} and D_{In} [122]–[124].

$$\begin{aligned}
\frac{\partial V}{\partial t} &= D_{\mathrm{V}} \frac{\partial^2 V}{\partial z^2} \\
\frac{\partial C_{\mathrm{Ga}}}{\partial t} &= \overline{D_{\mathrm{Ga}}} \frac{\partial^2 C_{\mathrm{Ga}}}{\partial z^2} \\
\frac{\partial C_{\mathrm{Al}}}{\partial t} &= \overline{D_{\mathrm{Al}}} \frac{\partial^2 C_{\mathrm{Al}}}{\partial z^2} \\
\frac{\partial C_{\mathrm{In}}}{\partial t} &= \overline{D_{\mathrm{In}}} \frac{\partial^2 C_{\mathrm{In}}}{\partial z^2}
\end{aligned}$$

The intermixing requires coupling the vacancy diffusion with that of the III-group atoms and it is done by considering effective diffusion coefficients as follows [121]:

$$\begin{aligned}
\overline{D_{\mathrm{Ga}}} &= D_{\mathrm{Ga}} \cdot \frac{V(z,t)}{V_{\mathrm{eq}}} \\
\overline{D_{\mathrm{Al}}} &= D_{\mathrm{Al}} \cdot \frac{V(z,t)}{V_{\mathrm{eq}}} \\
\overline{D_{\mathrm{In}}} &= D_{\mathrm{In}} \cdot \frac{V(z,t)}{V_{\mathrm{eq}}}
\end{aligned}$$

where V_{eq} as the equilibrium vacancy concentration which is strongly dependent on the annealing temperature.

It's possible to assume that the crystal lattice matching is conserved during diffusion and therefore all the involved atomic species diffuse with the same coefficient D_{III}. Moreover, assuming that the quantum well barriers are infinitely thick, eq. (2.4) can be used to describe the compositional disordering in the quantum well. Finally Schrödinger equation with a position-dependent mass can be solved numerically to obtain the bound states for both CB and VB.

In the case of IFVD process, the vacancies contributing to the compositional disordering are generated by the out-diffusion of Ga atoms into the dielectric cap [40], [125]. Therefore the vacancy flux should depend on RTA conditions, diffusivity D_{Ga} and solubility limit C_{sol} of Ga in the cap.

Therefore, considering a SiO_2 dielectric layer of thickness d and solubility limit C_{sol} and assuming that the Ga concentration at the interface is equal to C_{sol} during the whole RTA, the partial differential equation (PDE) and its boundary conditions can be expressed as [99]

$$\begin{cases} \frac{\partial}{\partial t} C_{\mathrm{Ga}} = D_{\mathrm{Ga}} \frac{\partial^2}{\partial z^2} C_{\mathrm{Ga}}(z,t) & 0 \leq z \leq d,\ 0 \leq t \leq t_{\mathrm{RTA}} \\ C_{\mathrm{Ga}} = C_{\mathrm{sol}} & z = 0,\ 0 \leq t \leq t_{\mathrm{RTA}} \\ \frac{\partial C_{\mathrm{Ga}}}{\partial z} = 0 & z = d,\ 0 \leq t \leq t_{\mathrm{RTA}} \\ C_{\mathrm{Ga}}(z,0) = 0 & t = 0,\ 0 \leq z \leq d \\ C_{\mathrm{Ga}}(z, t \to \infty) = C_{\mathrm{sol}} & t \to \infty,\ 0 \leq z \leq d \end{cases} \tag{2.7}$$

The vacancy profile in the epi-structure can be obtained solving the following PDE [99]

$$\begin{cases} \frac{\partial}{\partial t} V(z,t) = D_v \frac{\partial^2}{\partial z^2} V(z,t) & 0 \leq z \leq L,\ 0 \leq t \leq t_{\mathrm{RTA}} \\ \frac{\partial V}{\partial z} = 0 & z = L,\ 0 \leq t \leq t_{\mathrm{RTA}} \\ D_v \frac{\partial V}{\partial z} = D_{\mathrm{Ga}} \frac{\partial C_{\mathrm{Ga}}}{\partial z} & z = 0,\ 0 \leq t \leq t_{\mathrm{RTA}} \\ V(z, t=0) = 0 & t = 0,\ 0 \leq z \leq d \end{cases} \tag{2.8}$$

where the boundary condition $D_v \frac{\partial V}{\partial z}\Big|_{z=0} = D_{\mathrm{Ga}} \frac{\partial C_{\mathrm{Ga}}}{\partial z}\Big|_{z=0}$ relates the Ga out-diffusion and the vacancy generation. Therefore, solving both eqs. (2.7) and (2.8) it's possible to estimate the vacancy profile introduced by the IFVD process as shown in fig. 2.12.

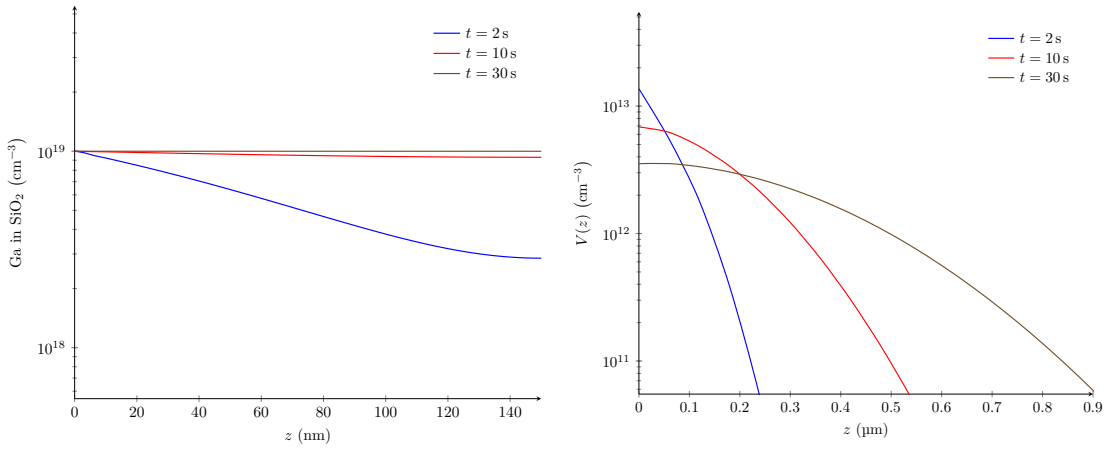

(a) Out-diffused Ga atoms

(b) Vacancies generated

Figure 2.12: Example of IFVD process

It can be noted that the Ga concentration in SiO_2 tends to reach very rapidly the solubility limit so the vacancy flux toward the epi-structure should decrease in time.

In particular, applying this model to the structure used in the experiments reported in this thesis, the dielectric cap consists of 150 nm SiO_2 layer deposited over the epitaxial structure. Both the solubility limit with $C_{\text{sol}} = 1 \times 10^{19}\,\text{cm}^{-3}$ and diffusion coefficient $D_{\text{Ga}} = 5.2 \cdot \exp(-1.77/k_B T)\ \text{cm}^2/\text{s}$ are reported in literature [99], [115], [119]. The resulting vacancy profile is shown in fig. 2.13.

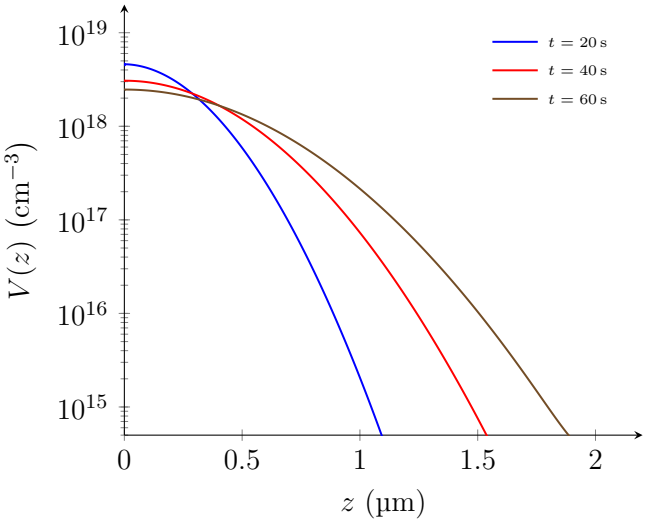

Figure 2.13: Diffused IFVD vacancy profile at 950 °C. At the interface the vacancy flux is reduced due to the saturation of SiO_2 cap.

At the interface between the material and the dielectric cap ($z = 0$) the flux of vacancies decreases after an initial transient due to the saturation of Ga atoms in the SiO_2 layer.

Therefore, using a 150 nm SiO_2 dielectric cap and annealing at 950 °C for 60 s the amount of vacancy generated at the quantum well depth $V(d_{\text{QW}})$ is approximately $6 \times 10^{16}\,\text{cm}^{-3}$. This approximation can be used only as an indication since the diffusion coefficients D_{Ga} and D_v may not accurately represent neither dielectric layer nor epi-structure.

2.5.5 Conclusions on modelling

The phenomenological model is able to correctly predict the intermixing process once the results of a series of experiments are available. Due to its simplicity, this model can be applied both to IFVD and IID processes but doesn't give any information about the physical phenomenon of the composition disordering.

The theoretical model, instead, is able to couple the vacancy profile with the intermixing process but it requires the knowledge of diffusion coefficient D_{III} that is not known in this phase. However it's possible to determine D_{III} from the comparison with experiments, in the same way of the phenomenological model. By doing this, it was possible to obtain $\Delta\lambda$ comparable with those reported in table 3.6, in particular 10.2 nm at 925 nm and 41.4 nm at 950 nm, both annealed for 1 minute. Obviously the needed phenomenological approach and the differences with respect to the measured wavelength shift give this model only a limited predictive ability.

Therefore, while in principle able to predict the amount of intermixing for a given RTA and process, the theoretical model requires the knowledge of each diffusion coefficient and, in literature, their proposed values may vary by orders of magnitude between different articles. So these models, at least at the present stage, can only give an indication of the compositional disordering and require a comparison against experimental results.

Chapter 3

IFVD experimental activity

Among the several techniques explained in chapter 2 to induce quantum well intermixing (QWI) in InGaAs/AlGaAs alloys, impurity free vacancy diffusion (IFVD) and inductively-coupled Ar plasma (ICP-Ar) were investigated being the needed technology already available in the production facility of Prima Electro/Convergent Photonics (fig. 3.1). The ICP-Ar technique was abandoned after the pre-investigation phase since it did not produce promising results (see section 3.4).

(a) Photolithography equipment (b) Plasma equipments

Figure 3.1: Part of the facilities in the laboratories of Prima Electro/Convergent Photonics

The aim of the whole experimental activity was to obtain a wavelength shift exceeding 20 nm (27 meV), suitable for the fabrication of non-absorbing mirrors (NAMs) at the facet of the laser diodes: the absorption reduction induced by this shift is in excess of 95%. Both the process flow and the technological tools were chosen to maintain compatibility with the current production.

The main parameters for IFVD process that were investigated are:

- the material stability to rapid thermal annealing (RTA) which gives the limits over which unwanted intermixing takes place;
- the choice of the dielectric material caps [104] which allows both spatial selectivity of

the process and suppression or enhancement [40], [42], [49], [126] of the compositional intermixing;

- the deposition conditions and the thickness of the dielectric caps that are further degrees of freedom to tune the wavelength shift [53], [127]–[130];
- the dielectric pattern/sequence, in particular the overlapping of dielectric layers, which eases the whole fabrication;
- the annealing conditions, in terms of time and temperature, that must be optimized in order to obtain the maximum possible shift in the NAM regions and minimum shift in the nominally non-intermixed regions;
- the mechanical stability of the wafers during RTA which became a major concern while transferring the process from small samples to whole wafers.

Room temperature photoluminescence (PL) was used to evaluate the wavelength shift. This requires the removal of the dielectric layers and around 1 µm of semiconductor to allow the detection of the PL emission from the intermixed quantum well.

The whole experimental activity has been carried out on samples from 4-in wafers (100 mm diameter) grown either by metal-organic chemical vapour deposition (MOCVD) or by molecular beam epitaxy (MBE). The available wafers differed from the ones used in current production, in particular their epi-structure, but they were considered equivalent to production wafers for what concerns quantum well intermixing. Two growth batches were used, one older with respect to the other, with the newer epi-structure having around 30% more Al in the barrier layers which causes an increased intermixing, thus explaining the variability in the results of different wafers in the same experiment.

The QWI parameters were investigated on samples of area around 2 cm^2 and, finally, the optimized process conditions were tested on whole 4-in wafers, denominated RD006, RD007 and RD008. Mechanical issues arisen in this phase have been overcome with proper adjustments which finally led to an optimised process.

3.1 Thermal stability

The thermal stability of both MOCVD and MBE material to RTA have been tested on 2 cm^2 samples. Samples were covered with a GaAs cap to prevent desorption of As and were annealed for 1 minute each in temperatures ranging from 800 °C to 1000 °C without any dielectric cap.

The wavelength shift became significant only for temperatures above 900 °C, as it can be seen in fig. 3.2. This poses a serious technological issue since the undesired diffusion of dopant atoms and the mechanical instability could arise at such high temperatures.

3.2 Dielectric caps

In literature [40], [42], [49], [126] is reported that intermixing can be enhanced or inhibited using different dielectric layers through IFVD while providing spatial selectivity. From the technological point of view, the main advantages of IFVD are the relative simplicity

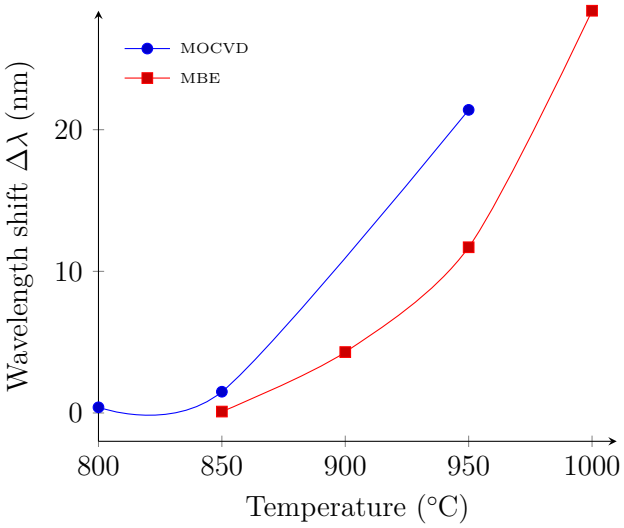

Figure 3.2: Thermal stability of bare samples

of the process and its promise of significant wavelength shift and spatial selectivity. In the present work, the technology that was used to deposit all the dielectric layers was the plasma enhanced chemical vapour deposition (PECVD).

3.2.1 Effect of different dielectrics

The dielectrics chosen to be deposited were Si_3N_4 and SiO_2 since in literature [104] they are reported to be able to, respectively, suppress and enhance the amount of intermixing in AlGaAs alloys. For what concerns the deposition parameters, both dielectrics were grown with recipes already established for the diode fabrication process.

Sample of 2 cm^2 were cleaved from MOCVD and MBE 4-in wafers and layers of 156 nm Si_3N_4 or 330 nm SiO_2 were deposited using PECVD. These samples were then annealed for 1 minute at temperatures ranging from 750 °C to 1000 °C.

As shown in figs. 3.3a and 3.3b the SiO_2 cap significantly enhanced the intermixing while Si_3N_4 cap effectively suppressed it.

Different deposition conditions are reported [127]–[130] to be able modify the amount of intermixing due to the different structure of the dielectric, in particular a more porous SiO_2 was shown to further enhance the intermixing under the same annealing conditions. So 440 nm less compressive SiO_2 layer were deposited by varying the deposition conditions and annealed between 800 °C and 950 °C for 1 minute.

However, with a maximum $\Delta\lambda$ of 48.6 nm at 950 °C, this non-standard SiO_2 did not prove to be more effective in inducing intermixing and the results were not deemed worth the increased complexity in the deposition parameters. So it was decided to only use the standard SiO_2 deposition with its consolidated and reliable recipe.

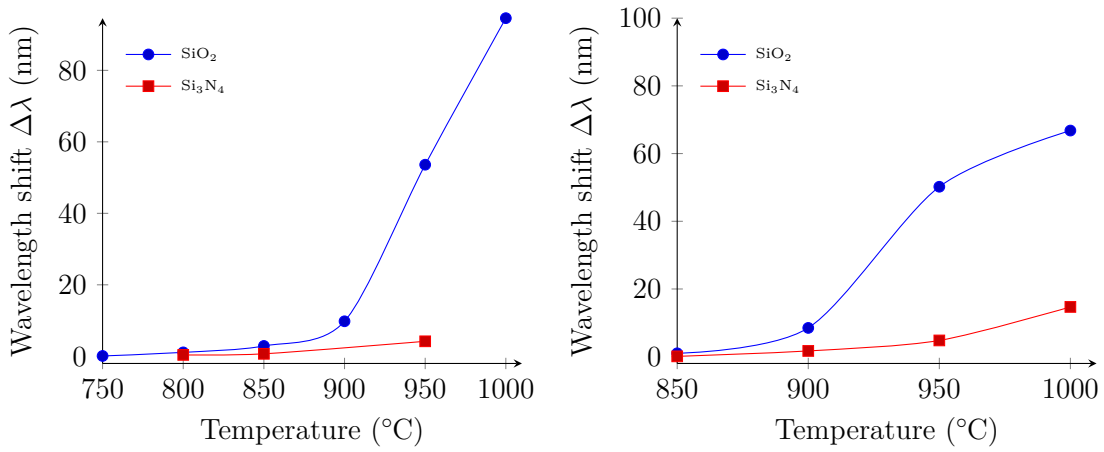

(a) MOCVD samples (b) MBE samples

Figure 3.3: Effect of different dielectric caps

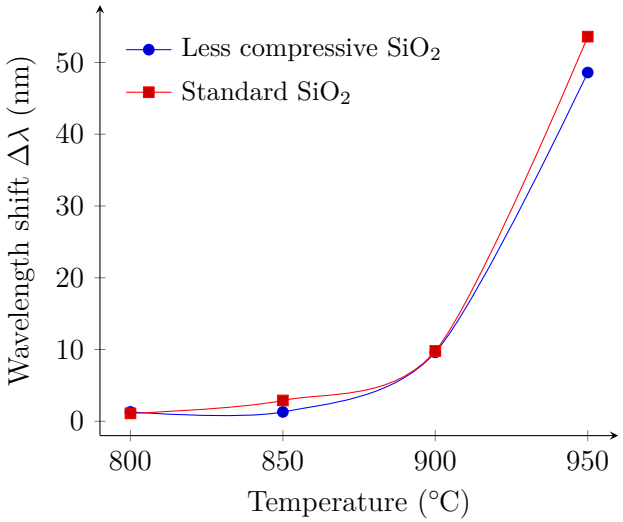

Figure 3.4: Wavelength shift caused by less compressive SiO_2 cap

3.2.2 Effect of different dielectrics configurations

The previous experiments used only a single dielectric layer to evaluate its capability to control the quantum well intermixing. However, intermixed laser diode fabrication requires spatial selectivity capability. So, samples of 2 cm^2 were patterned to have side-by-side or overlapping dielectrics in order to determine if the same wavelength shift could be observed while providing spatial selectivity to the process. In order to maximise the wavelength shift, the annealing condition was 950 °C for 1 minute, determined from the results shown in fig. 3.3. To pattern the dielectric layers a mechanical mask was used during the deposition to avoid the layer growth on roughly half the sample surface. In this way it was possible to

realize three different dielectric configurations: Si_3N_4-over-SiO_2, side-by-side Si_3N_4-SiO_2 and SiO_2-over-Si_3N_4.

Si_3N_4-over-SiO_2 structure

440 nm less-compressive or 330 nm standard SiO_2 layer were patterned on the samples through mechanical masking, then 156 nm of Si_3N_4 were deposited onto the whole surface. In both cases strong delamination of Si_3N_4 took place during the annealing (fig. 3.5).

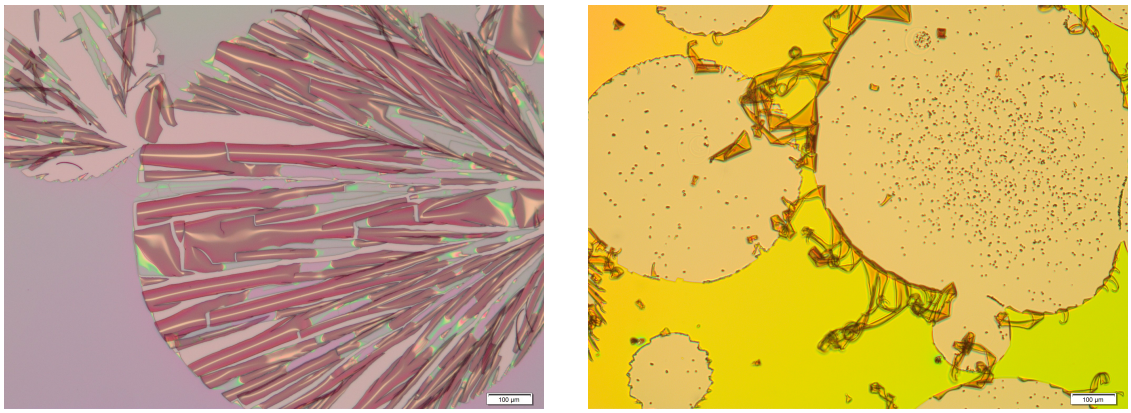

Figure 3.5: Delamination of Si_3N_4 from SiO_2

The cause of the delamination has been attributed to the difference in the thermal expansion coefficients of the dielectric layers. Measuring the stress caused by the each layer on the GaAs substrate the thermal expansion coefficient has been estimated according to [126]

$$\Delta\sigma = \left(\frac{E_f}{1-\nu_f}\right)\Delta\alpha\Delta T \tag{3.1}$$

where E_f is the Young modulus of the thin film, ν_f the Poisson coefficient of the film, σ is the stress and $\Delta\alpha$ is the difference of expansion coefficient between GaAs and layer. Considering $\Delta T = 650\,°C$ between RTA and layer deposition, the expansion has been estimated as $\Delta T \cdot \alpha_f$.

	$\frac{E_f}{1-\nu_f}$ (GPa)	α ($°C^{-1}$)	Expansion $\Delta T \cdot \alpha$
GaAs	-	6.86×10^{-6}	4.459×10^{-3}
Si_3N_4	370	6.172×10^{-6}	4.012×10^{-3}
SiO_2	85.4	5.914×10^{-6}	3.844×10^{-3}

Table 3.1: Estimation of thermal expansion of the dielectric layers during RTA

The intermediate layer of the Si_3N_4-over-SiO_2 structure expanded less than the top layer, as seen in table 3.1, thus introducing a strong mismatch between Si_3N_4 film and substrate. Therefore, to avoid the delamination, alternative structures were considered and the pattern Si_3N_4-over-SiO_2 was abandoned.

Side-by-side structure

The side-by-side configuration consisted in the deposition of 330 nm SiO_2 beside 156 nm Si_3N_4. The samples were annealed with temperatures ranging from 900 °C to 950 °C and no delamination took place.

Temperature (°C)	Time (s)	$\Delta\lambda_{Si_3N_4}$ (nm)	$\Delta\lambda_{SiO_2}$ (nm)	$\Delta\lambda_{Net}$ (nm)
900	60	0.1	-0.1	-0.2
925	60	1.6	11.3	9.7
950	60	4.0	23.4	19.4

Table 3.2: "Side-by-side" samples with older epi-structure

This experiment proved that a spatially-selective quantum well intermixing could be realized with regions protected by Si_3N_4 caps and others where the intermixing was enhanced by the SiO_2 layer, each region with its own amount of wavelength shift thus the important parameter is the net wavelength shift $\Delta\lambda_{Net}$. Tables 3.2 and 3.3 show the side-by-side results achieved on two different epi-structures.

Temperature (°C)	Time (s)	$\Delta\lambda_{Si_3N_4}$ (nm)	$\Delta\lambda_{SiO_2}$ (nm)	$\Delta\lambda_{Net}$ (nm)
925	60	0.3	25.9	25.6
950	60	4.5	57.8	53.3
950	60	-0.1	60.5	60.6
950	60	3.9	57.3	53.4

Table 3.3: "Side-by-side" samples with newer epi-structure

SiO_2-over-Si_3N_4 structure

Finally the overlapping of SiO_2 (150 nm or 330 nm) onto Si_3N_4 (156 nm) was investigated with samples annealed at 900 °C or 950 °C. As expected from the estimation of the thermal expansion in table 3.1, these samples did not suffered any delamination. The measured wavelength shift, instead, was less significant than expected due to the older epitaxial structure that was used (table 3.4).

This series of experiments proved that it's possible to realize a spatially-selective quantum well intermixing with a SiO_2-over-Si_3N_4 structure which simplifies the eventual fabrication process with respect to a side-by-side configuration. However, the rapid thermal annealing changes the SiO_2 structure [43], [44] in such a way that the etch rate in HF solutions is significantly reduced therefore, to remove the layer, a dry attack becomes necessary, followed by a O_2 plasma and a de-oxidation.

3.2.3 Effect of SiO_2 thickness

According to literature [41], [131] the SiO_2 thickness affects the amount of intermixing so a series of experiments was performed to evaluate this possible degree of freedom in the

SiO_2 (nm)	Temperature (°C)	$\Delta\lambda_{Si_3N_4}$ (nm)	$\Delta\lambda_{SiO_2}$ (nm)	$\Delta\lambda_{Net}$ (nm)
150	900	0.2	2.3	2.1
150	950	3.4	21.1	17.7
330	900	0.5	1.4	0.9
330	950	2.4	15.6	13.2

Table 3.4: SiO_2-over-Si_3N_4 samples annealed for 60 s

process. From table 3.4 it can be noted that, within the same epi-structure, the wavelength shift doesn't depend significantly on the SiO_2 thickness.

A few sample with overlapped dielectrics, SiO_2 over patterned Si_3N_4, were prepared to investigate the effect of the SiO_2 thickness and to compare their wavelength shift with the side-by-side configuration. The Si_3N_4 thickness was kept 156 nm, while the SiO_2 one varied between the samples: two had 150 nm while another two 330 nm. All samples were annealed at 950 °C for 1 minute.

SiO_2 (nm)	Temperature (°C)	$\Delta\lambda_{Si_3N_4}$ (nm)	$\Delta\lambda_{SiO_2}$ (nm)	$\Delta\lambda_{Net}$ (nm)
150	950	2.7	48.5	45.8
150	950	6.5	56.7	50.2
330	950	8.5	59.6	51.1
330	950	3.5	49.4	45.9

Table 3.5: Effect of SiO_2 thickness

From this run of rapid thermal annealing again no delamination was observed and from the results reported in table 3.5 it's possible to notice that the wavelength shift is comparable with those in table 3.3. Therefore this experiment proved that the overlapping of Si_3N_4 and SiO_2 does not compromise the ability of the Si_3N_4 layer to suppress the intermixing. Moreover, under these annealing conditions, the net $\Delta\lambda$ was consistently above 40 nm and the thickness of PECVD SiO_2 didn't affect the amount of intermixing. This difference with respect to literature has been attributed to the rapid saturation of Ga atoms in the SiO_2 cap during RTA.

3.2.4 Effects of RTA conditions

Since the temperatures needed to achieve a significant intermixing are particularly elevated, the possibility to do an annealing at lower temperatures but for longer times was explored. Several samples were prepared with the deposition of SiO_2 on patterned Si_3N_4 and the chosen annealing conditions ranged from 850 °C and 950 °C between 1 and 5 minutes.

From this experiment it's clear that the wavelength shift increases linearly with time, however it was impossible to reach the desired net $\Delta\lambda$ at 850 °C. Moreover annealing at 900 °C for 5 minutes is not useful since the shift in the Si_3N_4 region is excessive.

Temperature (°C)	Time (s)	$\Delta\lambda_{\text{Net}}$ (nm)
850	300	7.5
900	60	5.8
900	120	10.6
900	180	20.3
900	300	42.6
925	120	21.3
925	180	35.9

Table 3.6: $\Delta\lambda$ for different RTA conditions

3.3 Conclusions on dielectric caps

The experiments carried out on $2\,\text{cm}^2$ samples show that a wavelength shift exceeding 40 nm can be achieved using a SiO_2-over-Si_3N_4 dielectric pattern and annealing condition 950 °C for 1 minute. This may significantly damage the material itself, however, the experiments performed at lower temperatures for longer times did not prove satisfying for the realization of NAMs. Therefore these conditions were transferred to a 4-in wafer for a complete fabrication process.

3.4 ICP-Ar bombardment

In parallel to the experiments on the effects of dielectrics, the effect of Ar^+ bombardment on intermixing was investigated. An inductively coupled plasma reactive ion etching (ICP-RIE) was used to realize two opposite conditions: high V_{bias} / low plasma density, high ion energy but low dose, and, vice versa, low V_{bias} / high plasma density. The Ar^+ bombardment took place on bare samples and after the attack it was decided to deposit 330 nm SiO_2 on half of the sample surface in order to evaluate the possibility of coupling Ar plasma and dielectrics to eventually reduce the annealing temperature. The samples underwent rapid thermal annealing at 950 °C for 1 minute.

Condition	$\Delta\lambda_{\text{Ar}}$ (nm)	$\Delta\lambda_{\text{SiO}_2\ +\ \text{Ar}}$ (nm)
High plasma density, low V_{bias}	0.2	21.6
Low plasma density, high V_{bias}	2.9	42.6

Table 3.7: ICP-Ar bombardment with RTA 950 °C for 1 minute

These experiments were challenging since the ICP-RIE is not designed to induce such Ar^+ bombardment, so the machine had trouble to keep under control the process parameters. The results were not satisfying since the ion bombardment did not induce significant intermixing in both samples and no cumulative effect was observed in the regions where SiO_2 was also deposited. More interestingly, in the high plasma density/low ion energy condition, the measured $\Delta\lambda$ was half with respect to the other condition. It is possible that a very shallow slight implantation of Ar^+ ions took place and blocked the out-diffusion of

Ga atoms from the material, therefore reducing the intermixing. However more experiments are needed to demonstrate such effect.

3.5 Complete fabrication process (RD006)

From previous experiments $\Delta\lambda$s exceeding 40 nm were obtained with rapid thermal annealing at 950 °C for 1 minute using the overlapped dielectrics. So it was decided to test the effect on a 4-in wafer, denominated RD006, performing a complete fabrication process.

3.5.1 Wafer preparation

A single wafer (RD006) was prepared for the intermixing process. Both diodes with and without intermixing have been fabricated on the same wafer in order to evaluate the quantum well intermixing effectiveness on devices that underwent the same treatment. Using electron beam lithography a mask was prepared in such a way to have non-absorbing mirrors (NAMs) on both AR and HR facets of half the final devices.

After a first weak etching to realize alignment marks for the process, 150 nm of Si_3N_4 were deposited onto the wafer. Through photolithography (see fig. 3.6) and RIE this first dielectric layer was patterned in order to open the intermixing windows. Finally 156 nm of SiO_2 were deposited onto the whole wafer thus realizing the dielectric overlapping.

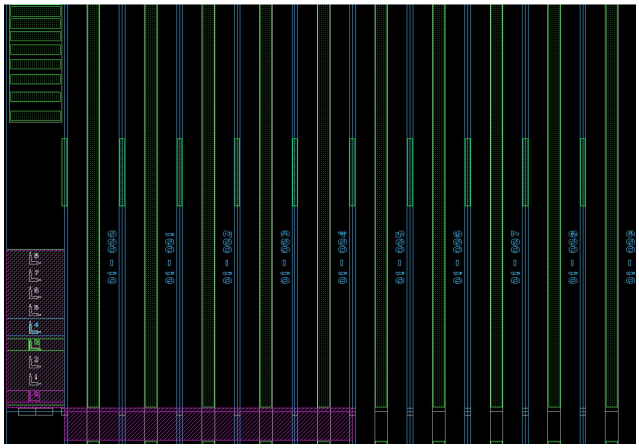

Figure 3.6: CAD of photolithography mask, in magenta the NAM region

A stack of three 4-in (100 mm) wafers was inserted in the RTA chamber: a silicon carrier, the process wafer and a GaAs cap onto which 500 nm of Si_3N_4 were deposited to prevent As desorption. This proved challenging since the wafers tended to slid from one another and no practical way was found to keep them in place.

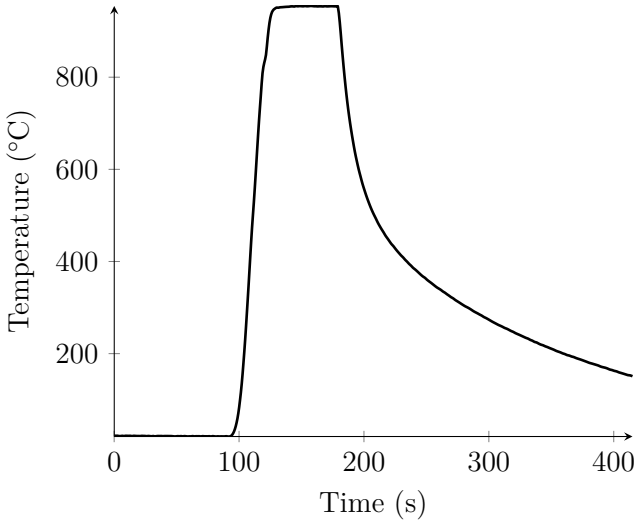

Figure 3.7: Rapid thermal annealing of RD006

3.5.2 Issues

Once the RTA was completed several serious issues emerged immediately: first of all the wafers moved during the annealing as can be seen in fig. 3.8. So it's possible that the whole wafer did not reach the same temperature, moreover its backside was exposed thus liberating As in the chamber.

Figure 3.8: Wafer stack after RD006 RTP

More importantly the process wafer was visibly deformed by the annealing so a bowing measure was attempted using a mechanical profilometer. However the deformation was beyond the measurement range of the instrument (325 µm). After the removal of the dielectric layers with RIE, the wafer had partially recovered but the deformation still exceeded the measurement limits. The resist spinner was unable to keep the wafer under

vacuum so, to continue with the fabrication process, a part of the wafer was cleaved. This deformation significantly increased the difficulty of the rest of the process. Furthermore cracks of 10 mm appeared from the border of the wafer toward the center.

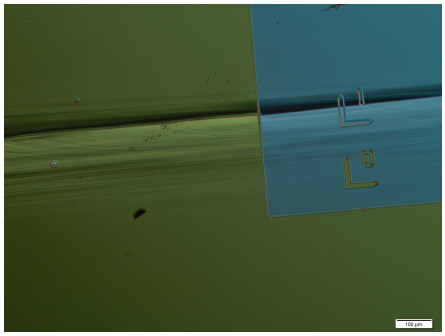

Figure 3.9: Typical cracks extending from the border to the center of the wafer for 10 mm after RTA

Moreover the wavelength shift measured from the cleaved part of the wafer was significantly reduced with respect to the previous experiments reaching a net $\Delta\lambda$ of 15 nm as seen in fig. 3.10.

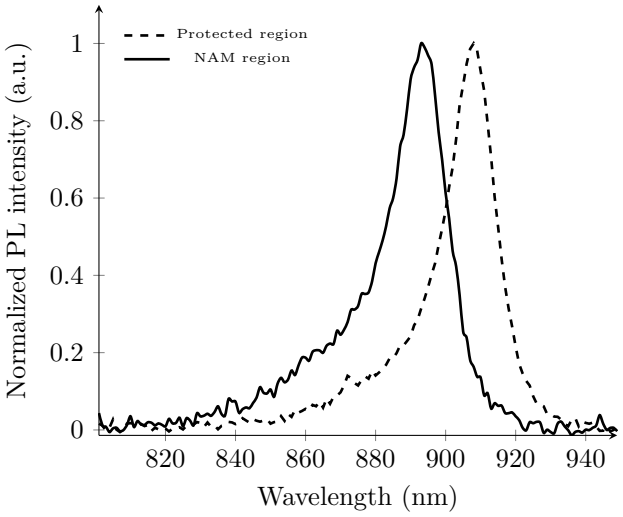

Figure 3.10: PL spectra from RD006

3.5.3 Diode testing

Even though the final diodes presented a significant variability in their electrical parameters probably due to the compromised fabrication process, it was possible to select diodes of both groups (QWI, NO-QWI) with comparable characteristics with respect to the standard production in number sufficient to have statistical significance.

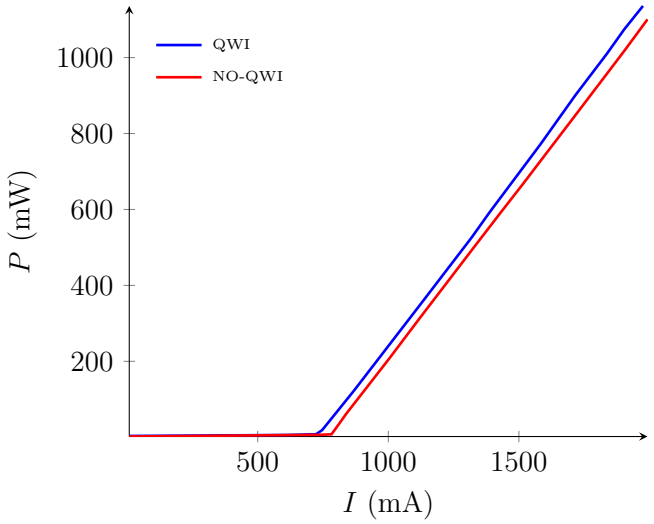

Figure 3.11: Typical PI characteristics of QWI and NO-QWI diodes of RD006 process

The difference in the threshold current I_{th} between the two groups, visible in figs. 3.11 and 3.12, is an indication of the effectiveness of the NAMs: in standard diodes the facets are non-injected absorbing regions thus an higher current is needed to have laser emission, while in intermixed diodes the same region is transparent to the laser wavelength so the threshold current is reduced.

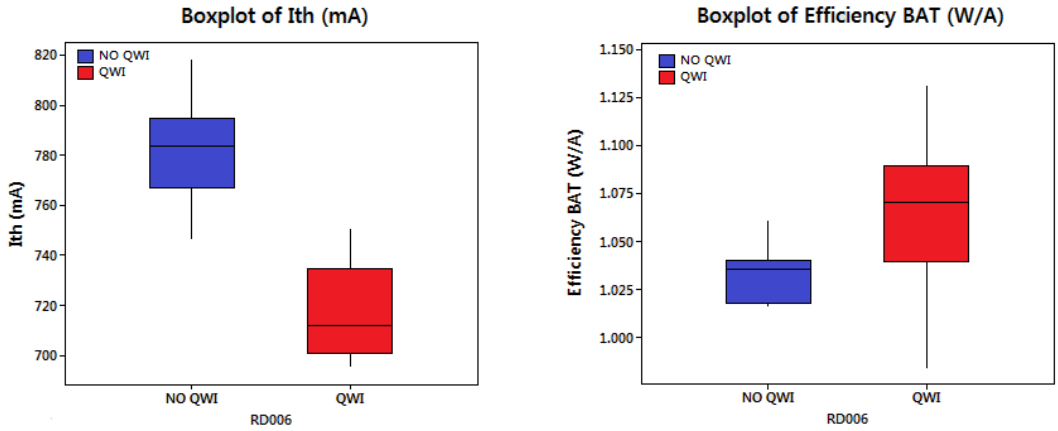

(a) Threshold current I_{th}

(b) Efficiency η

Figure 3.12: RD006 electrical parameters

Finally the diodes underwent the burn-in, in which they are subjected to accelerated aging conditions for several hours in order to eliminate the early failures. The results of this tests were extremely noteworthy since yield of the NO-QWI diodes was 25%, while the yield of the QWI group was 82%. These values were below the yield of the standard production but this was attributed to the compromised fabrication process.

3.5.4 Results

The photoluminescence spectrum of the NAM region showed a net $\Delta\lambda = 15\,\text{nm}$ which, while less than expected, induced a significant reduction of the absorption profile. In fact, as a first estimate, the material absorption profile (obtained from photocurrent measures) is assumed to be rigidly shifted by $\Delta\lambda$ as shown in fig. 3.13. Thus the absorption reduction was estimated to be around 96% with respect to the initial material. From this result a net $\Delta\lambda$ of 20 nm was deemed sufficient for future experiments on whole wafers.

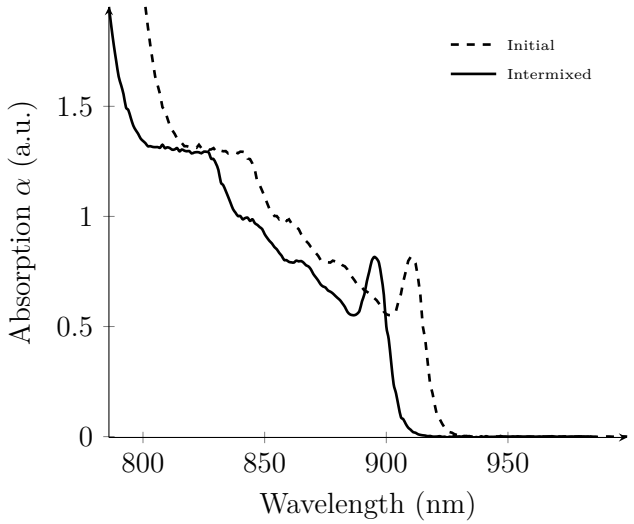

Figure 3.13: Estimation of the absorption profile from photocurrent measures

As previously explained, the QWI diodes presented significant differences in both threshold current and survivability during burn-in with respect to "standard" diodes realized from wafer RD006. So the intermixed diodes proved to be more robust than their standard counterpart from the same wafer. Although the QWI diodes didn't show improvements with respect to the standard production, possibly due to the deformation during RTA, the results were deemed promising to further investigate NAM processes.

3.6 Mechanical stability

Since the wafer RD006 was extremely deformed after the annealing, the mechanical stability of the wafer was investigated in order to evaluate the maximum annealing temperature that could be used both in a IFVD process and in a IID one.

Two MBE wafers were used as samples, onto the p-side of each of them a 156 nm Si_3N_4 layer was deposited to prevent As desorption during the process. A silicon wafer was used as support.

As can be seen in figs. 3.14 and 3.15 the material is not deformed after the annealing at 600 °C but at 800 °C the deformation is already beyond the measurement limits of the profilometer (325 µm), probably sufficient to compromise the processing of the wafer.

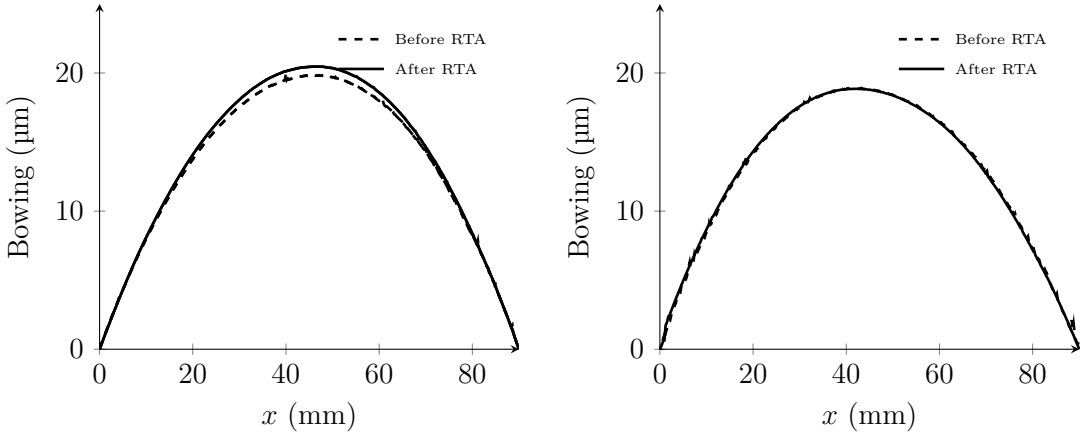

(a) 0° (b) 90°

Figure 3.14: Wafer MBE23N with RTA 600 °C for 1 minute

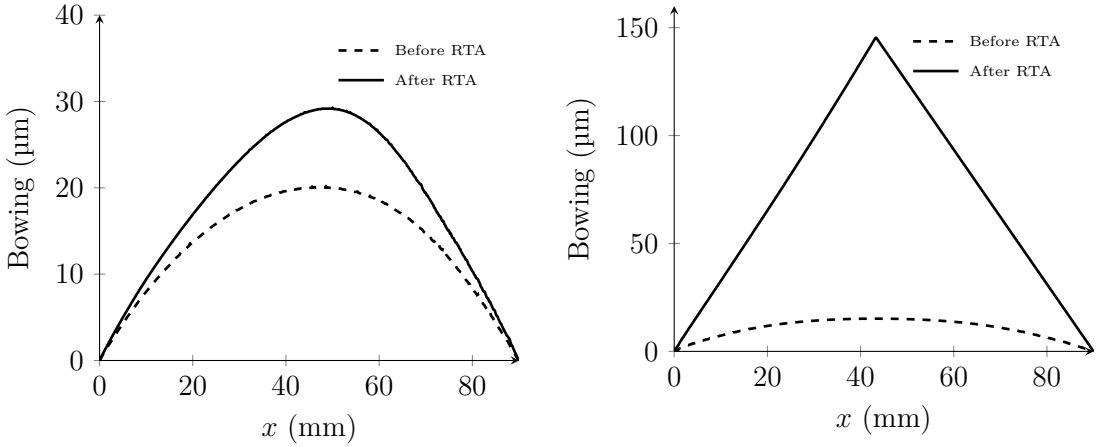

(a) 0° (b) 90°

Figure 3.15: Wafer MBE23C with RTA 800 °C for 1 minute. The profilometer was unable to complete the bowing measure in the 90°direction due to the excessive deformation of the wafer.

3.6.1 Double dielectrics

Since the IFVD process is quite simple and can be realized using machinery readily available, the possibility of controlling the wafer deformation through the deposition of dielectrics was investigated. The same dielectric structure used for the RD006 process, 150 nm of SiO_2 over 156 nm of Si_3N_4, had been deposited on both sides of two wafers (RD007, RD008). This, in principle, should compensate the stress of the dielectrics during the annealing.

Moreover, the deposition of dielectrics on both sides of the wafer made unnecessary the use of the Si carrier wafer and of the GaAs cap wafer since the dielectrics prevented the As desorption. Thus, to evaluate the deformation of the wafer, several measures of bowing

were performed in different stages of the experiment:

1. before any deposition
2. after the Si_3N_4 deposition on top side
3. after the Si_3N_4 deposition on back side
4. after the SiO_2 deposition on top side
5. after the SiO_2 deposition on back side
6. after the RTA
7. after the removal of dielectric layers from the backside
8. after the removal of dielectric layers from the topside

Finally it was also possible, thanks to the photolithography used to pattern the top Si_3N_4 layer, to evaluate the $\Delta\lambda$ shift in the intermixing region.

Two different wafers were prepared and both underwent an annealing at 950 °C but for different times, one for 60 s and the other for 120 s. However, due to a mistake while operating the rapid thermal annealer, both samples briefly reached 965 °C. The following measures at the profilometer showed that the bowing of the wafers was actually reduced once the dielectrics were removed from both sides.

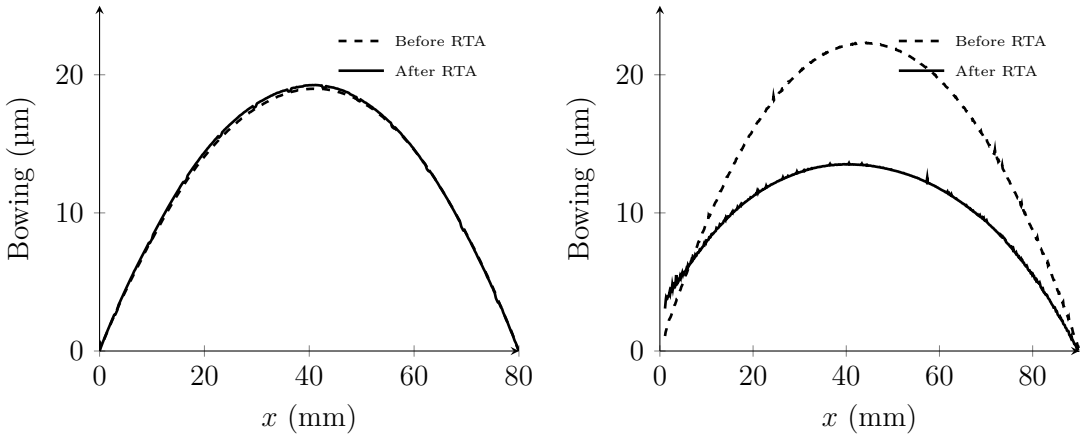

(a) 0° (b) 90°

Figure 3.16: Wafer bowing with RTA 950 °C, 120 s

As can be seen in fig. 3.16 the wafer only slightly deformed during the annealing, reducing its bowing from 23 µm to 12 µm along one direction, and a complete fabrication process was, therefore, considered viable. Moreover it was possible to evaluate also the $\Delta\lambda$ after RTA as can be seen in table 3.8.

The wavelength shift in the wafer annealed for 1 minute was comparable with that of the RD006 process while the wafer annealed for two minutes presented an significant reduction of the PL intensity.

Temperature (°C)	Time (s)	$\Delta\lambda_{Si_3N_4}$ (nm)	$\Delta\lambda_{SiO_2}$ (nm)	$\Delta\lambda_{Net}$ (nm)
950	60	4.7	20.9	16.2
950	120	9.6	42.4	32.8

Table 3.8: Intermixing with double dielectrics

3.7 Improved fabrication process (RD007, RD008)

Two MOCVD wafers, denominated RD007 and RD008, were used for an improved fabrication process that makes use of the double dielectrics in order to control the mechanical deformation during the annealing. Moreover using this procedure it was possible to completely avoid the use of both GaAs cap and Si carrier that moved during the RTA of the RD006 (fig. 3.8).

The annealing conditions were 950 °C for 1 minute as the RD006 process, the wafer were prepared with the deposition of the dielectric layers on both top and backside. Finally the top side was patterned using the mask realized for the RD006 wafer (fig. 3.6).

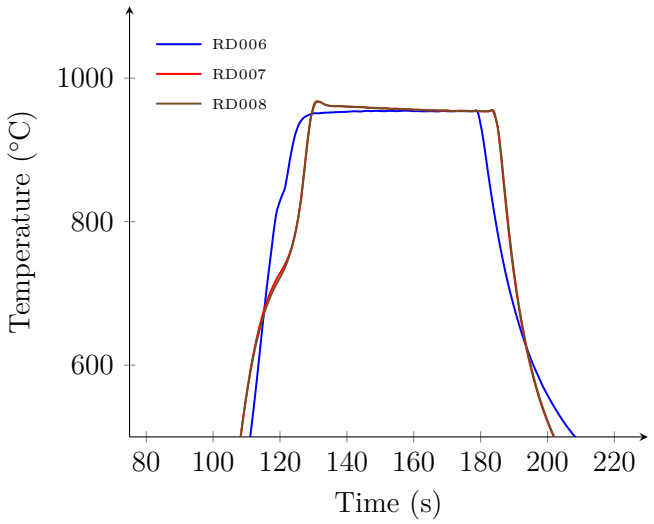

Figure 3.17: Comparison of RTA processes of RD006, RD007, RD008

Before performing the annealing, a self-calibration of the machine was attempted using a single GaAs wafer to simulate the thermal load seen in the process. However, this procedure did not improve the temperature ramp and the wafers reached higher temperatures, specifically 965 °C, with respect to the RD006 as seen in fig. 3.17.

To evaluate the effectiveness of the double dielectrics technique, the bowing of the wafers was measured before and after the RTA as seen in figs. 3.18 and 3.19 and, as previous experiments showed, the deformation was kept under control thus allowing to continue the process without cleaving.

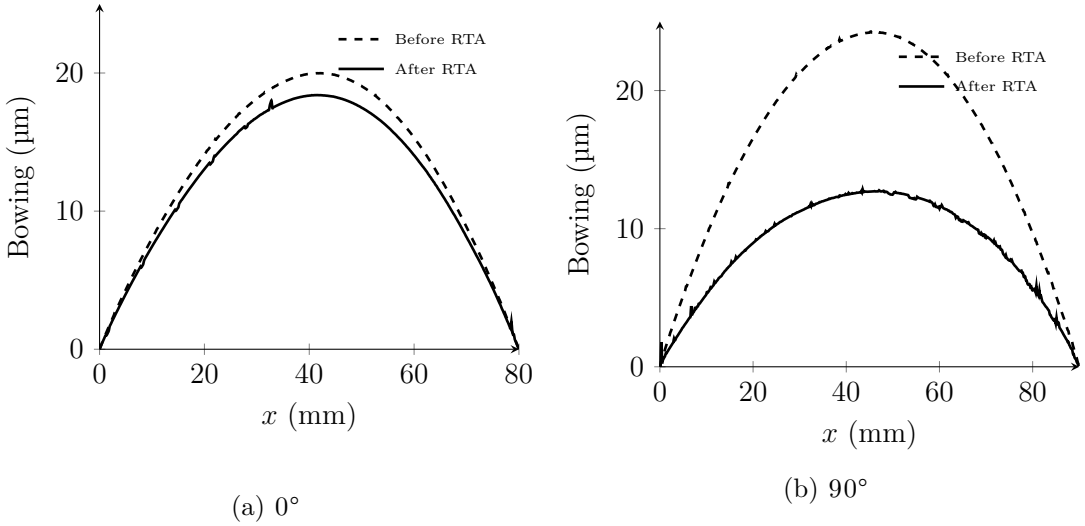

(a) 0° (b) 90°

Figure 3.18: Bowing of wafer RD007

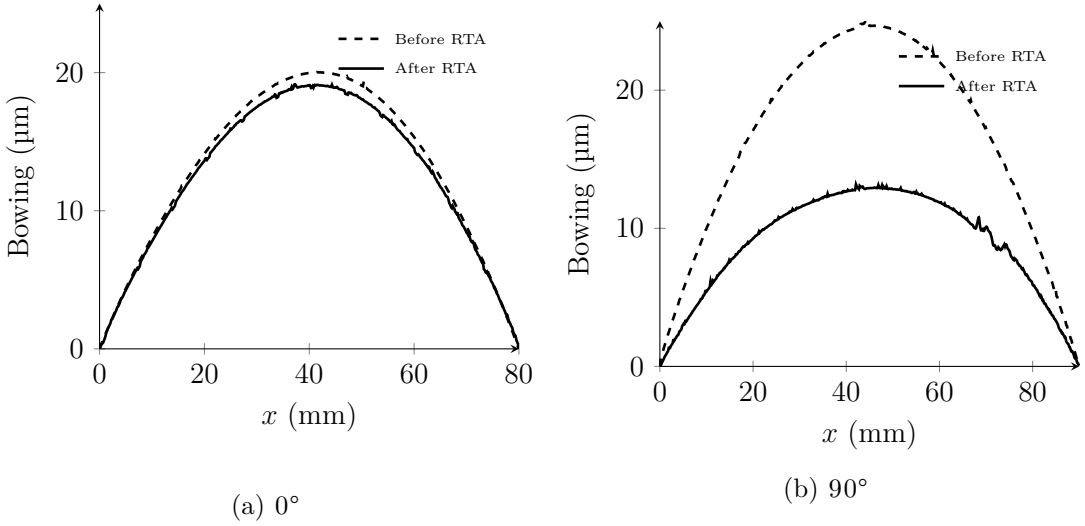

(a) 0° (b) 90°

Figure 3.19: Bowing of wafer RD008

As in the case of the RD006 process the diodes belonging to both groups, QWI and NO-QWI, were characterized in terms of efficiency and threshold, as shown in fig. 3.20. As observed in the previous process, the threshold current I_{th} of the intermixed diodes was lower with respect to the NO-QWI diodes, thus showing the first effects of the NAM regions.

The yield of the burn-in test presented significant differences with respect to the RD006 process. In particular the yield of the NO-QWI diodes was 71%, therefore the process within the production specifications. In this group COMD took place in the first 10 hours of the test.

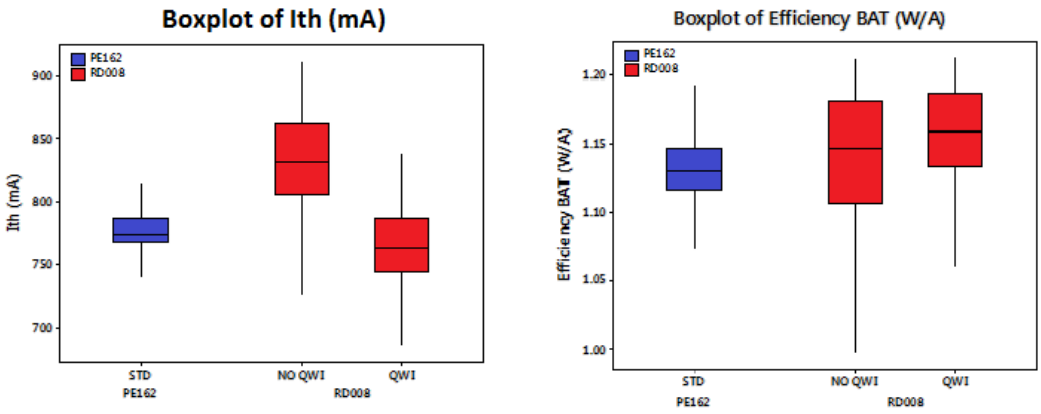

(a) Threshold current I_{th} (b) Efficiency η

Figure 3.20: RD008 electrical parameters

The NO-QWI diodes, instead, presented a yield of 78% with the first COMD almost at the end of the burn-in test. The results look promising and further reliability tests are ongoing.

Chapter 4

IID preliminary considerations

The quantum well intermixing induced by dielectric caps gave promising results, but the required temperature to achieve $\Delta\lambda = 15\,\text{nm}$ on 4-in wafers was deemed too extreme. So the impurity-induced disordering (IID) was considered as an alternative process, in order to obtain a similar or greater blueshift at lower temperatures due to vacancy generation closer to the quantum well. The simulations reported in this chapter were used to determine the IID conditions of future ion implantation experiments.

The IID process is realized through an ion implantation and the main parameters of this approach are

- the implanted species;
- the implantation energy;
- the ion dose;
- the annealing conditions.

Since this process should not introduce recombination centers inside the NAM region, the best choice is to implant atoms already present in the crystalline matrix, in particular As ions. From literature [132] the minimum dose to have an appreciable intermixing was 10^{13} ions/cm^2 so several simulations have been performed to evaluate the vacancy profile caused by the implantation followed by RTA. These results have been compared with the simulations carried out in the implanting facility of Surrey University (its equipment is shown in fig. 4.1). The implantation energy determines the depth at which As are implanted but, if the energy is excessive, can also form non-radiative recombination centers or causing unacceptable damage in the epitaxial structure.

Since the compositional intermixing is mediated by the diffusion of III-group vacancies during RTA, a comparison between the vacancy profiles obtained with IFVD or IID can give an insight on the efficiency of quantum well intermixing.

The IID investigation is carried out in cooperation with the implanting facility of Surrey University which provides both simulations of the introduced vacancy profiles and performs the ion implantation.

Figure 4.1: Surrey 2 MeV implanter (up to 4 MeV if double ionized atoms are used)

4.1 SRIM simulations

The software SRIM [133] was used to evaluate the conditions to be used in an IID process on a simplified epitaxial structure. The main parameters were the ion energy, the generated vacancy profile and its diffusion in order to compare the IID process with the IFVD one. The IFVD reference is the simulation shown in fig. 2.13 which gave around 10^{17} vacancies/cm^3.

4.1.1 Implantation depth

The implantation energy determines the depth reached by the As ions during the implantation and controls also the generated vacancy profile. Since the implantation may cause unrecoverable crystalline damage to the structure, it's desirable to use an energy as low as possible and exploit the vacancy diffusion to reach the quantum well.

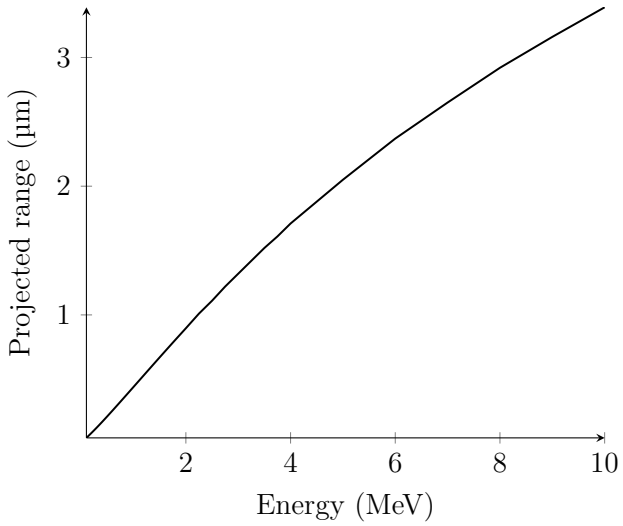

Figure 4.2: SRIM implantation range in GaAs

The implantation depth as function of ion energy is shown in fig. 4.2. In order to avoid the implantation of As directly in the quantum well layer but, at the same time, to allow vacancies to reach the well with a RTA at lower temperature, the most interesting energy was between 2 and 3 MeV.

4.1.2 Generated vacancies

The vacancy profile caused by As ion implantation can be estimated using the SRIM. These simulations have been performed varying the energy in 2 MeV ÷ 3 MeV and for three different doses.

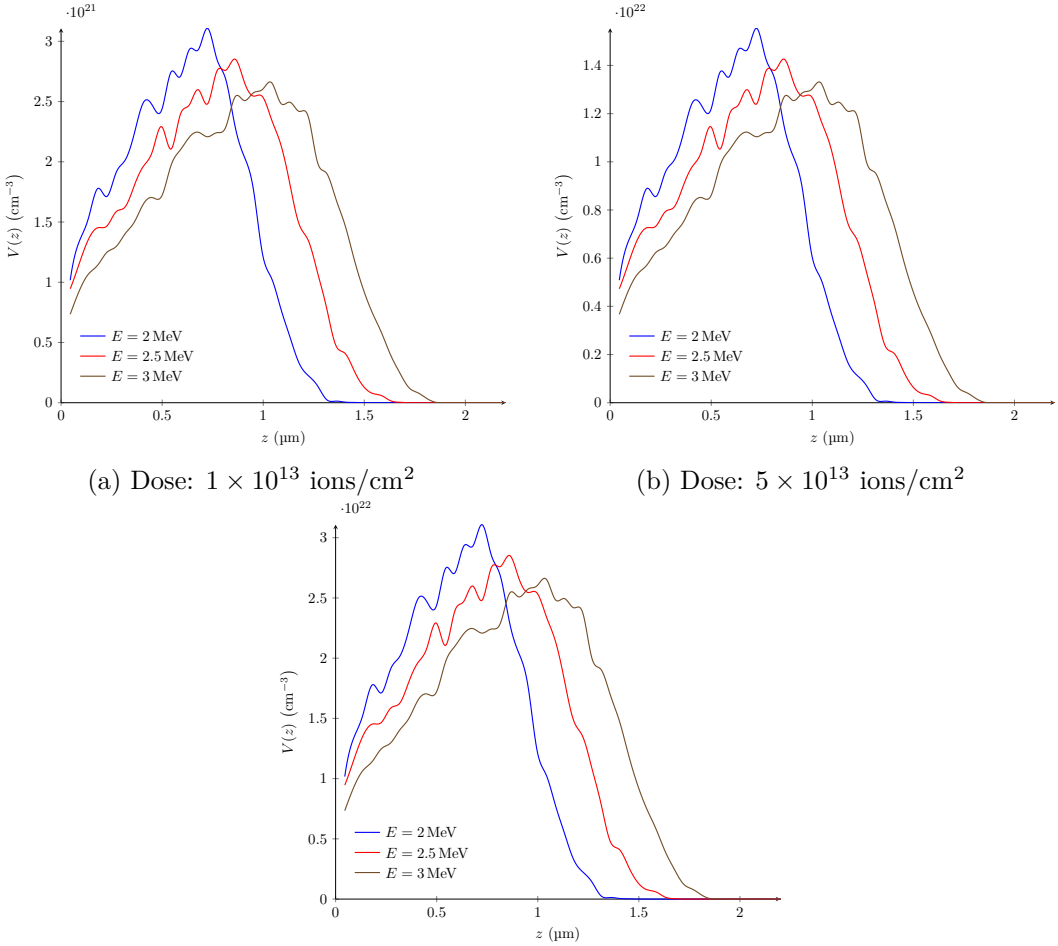

(a) Dose: 1×10^{13} ions/cm^2

(b) Dose: 5×10^{13} ions/cm^2

(c) Dose: 1×10^{14} ions/cm^2

Figure 4.3: SRIM vacancy profiles

4.1.3 Vacancy diffusion

The SRIM vacancy concentrations shown in fig. 4.3 were diffused to consider the effect of RTA conditions and the profiles at the quantum well depth were compared with the IFVD process at 950 °C. The diffusion is assumed to follow

$$\frac{\partial}{\partial t}V(z,t) = D_v \frac{\partial^2}{\partial z^2}V(z,t) \tag{4.1}$$

with diffusion coefficient given by $D_v(T) = 2.886 \cdot \exp(-2.72/k_B T)$ cm^2/s [99]. This partial differential equation(PDE) was solved numerically using FEM as explained in appendix B with RTA 800 °C for 60 s.

From the comparison of fig. 2.13, fig. 4.4 and table 4.1 it's evident that both the amount and flux of vacancies generated in the IFVD process is extremely reduced with respect to the IID one. So it may be possible to use much lower annealing temperatures since the vacancies are much closer to the quantum well.

Dose $\left(\text{ions/cm}^2\right)$	$V(d_{\text{QW}})$ at 2 MeV	$V(d_{\text{QW}})$ at 2.5 MeV	$V(d_{\text{QW}})$ at 3 MeV
1×10^{13}	2.2×10^{20} cm^{-3}	1.2×10^{21} cm^{-3}	2.2×10^{21} cm^{-3}
5×10^{13}	1.1×10^{21} cm^{-3}	6.1×10^{21} cm^{-3}	1.1×10^{22} cm^{-3}
1×10^{14}	2.2×10^{21} cm^{-3}	1.2×10^{22} cm^{-3}	2.2×10^{22} cm^{-3}

Table 4.1: SRIM vacancy concentration at quantum well depth after annealing at 800 °C for 60 s. These values must be compared with $V(d_{\text{QW}}) = 6 \times 10^{16}$ cm^{-3} of the IFVD process.

4.2 Experiment preparation

The SRIM results were compared with the simulation performed at the implanting facility of Surrey University to understand if a more detailed computation confirms the evaluation of the vacancy profiles. From figs. 4.5a to 4.5c it's possible to notice the SRIM overestimated the concentrations by two orders of magnitude.

The vacancy profiles obtained from Surrey University were diffused under the same conditions of the SRIM concentrations and in the quantum well region the vacancies introduced by IID are confirmed to exceed by orders of magnitude the IFVD ones as seen in fig. 4.6.

Dose $\left(\text{ions/cm}^2\right)$	$V(d_{\text{QW}})$ at 2 MeV	$V(d_{\text{QW}})$ at 2.5 MeV	$V(d_{\text{QW}})$ at 3 MeV
1×10^{13}	1.3×10^{19} cm^{-3}	3.6×10^{19} cm^{-3}	4.3×10^{19} cm^{-3}
5×10^{13}	6.1×10^{19} cm^{-3}	1.7×10^{20} cm^{-3}	2.2×10^{20} cm^{-3}
1×10^{14}	1.2×10^{20} cm^{-3}	3.5×10^{20} cm^{-3}	4.3×10^{20} cm^{-3}

Table 4.2: Surrey vacancy concentration at quantum well depth after annealing at 800 °C for 60 s. These values must be compared with $V(d_{\text{QW}}) = 6 \times 10^{16}$ cm^{-3} of the IFVD process.

From these considerations the chosen implantation conditions were 2 MeV and 3 MeV, each with two doses, 10^{13} and 10^{14} ions/cm^2. Preparing the 4in-wafers for the experiment

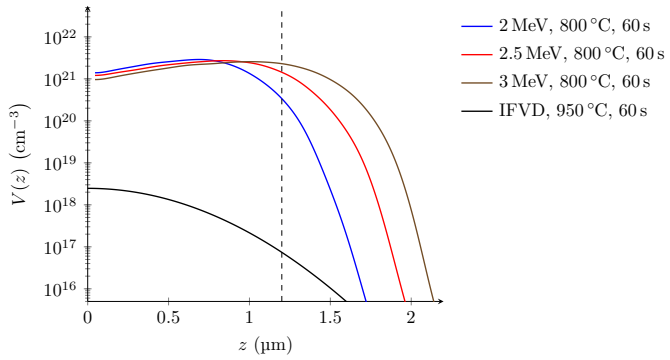

(a) Dose: 1×10^{13} ions/cm^2

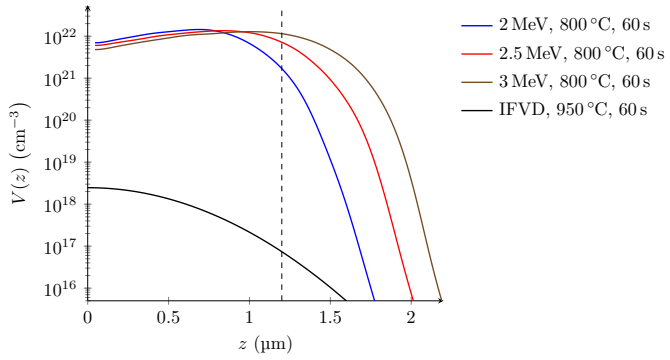

(b) Dose: 5×10^{13} ions/cm^2

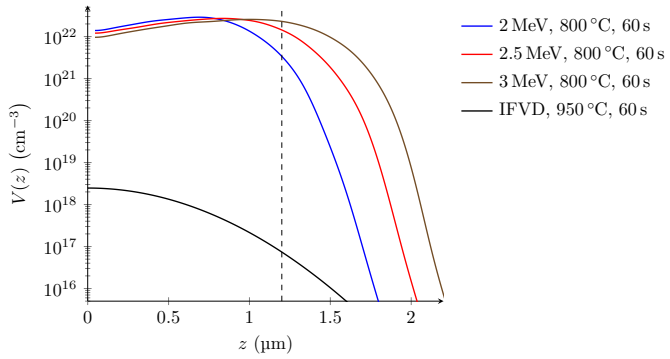

(c) Dose: 1×10^{14} ions/cm^2

Figure 4.4: Diffusion of SRIM vacancies with RTA 800 °C for 60 s. The dashed line represents the quantum well depth

requires both a 300 nm Si_3N_4 layer to prevent superficial damage and a hard mask to stop the As ions, thus providing spatial selectivity to the quantum well intermixing process.

To determine the thickness of the hard mask new simulations were performed and showed that with 300 nm of Si_3N_4 and 1.5 µm of Au the As ions are unable to reach the epi-structure as seen in fig. 4.7.

The hard mask is realized using titanium (Ti) and gold (Au) grown over the Si_3N_4 layer. In particular:

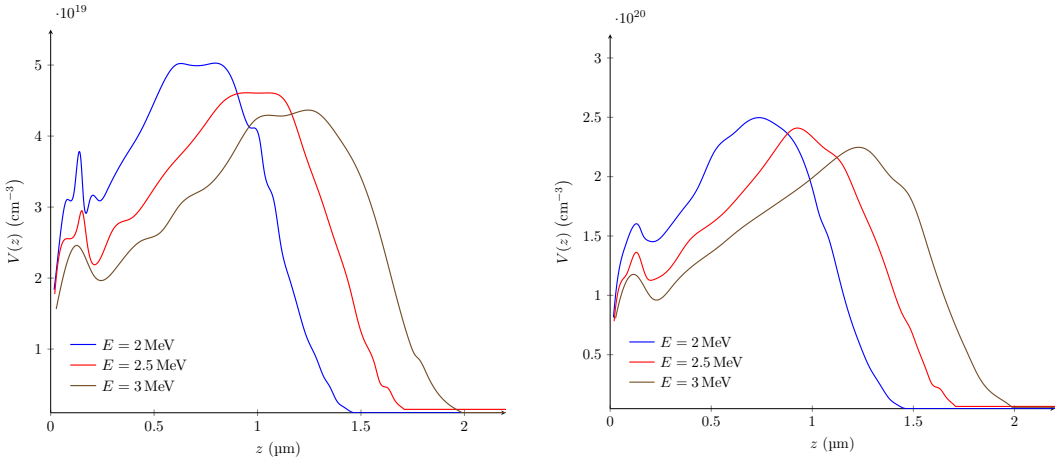

(a) Dose: 10^{13} ions/cm^2

(b) Dose: 5×10^{13} ions/cm^2

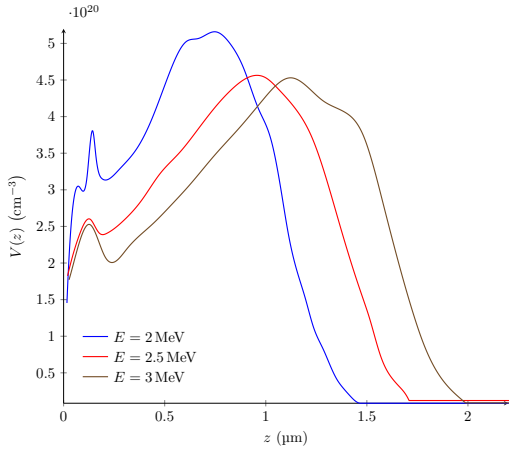

(c) Dose: 10^{14} ions/cm^2

Figure 4.5: Vacancy profiles, courtesy of Surrey University

- 30 nm-Ti/100 nm-Au deposited by evaporation to improve adhesion of electroplated Au;
- $>$ 1.5 µm of Au grown by electroplating;

However, due to the Si_3N_4 protective layer, additional simulations were carried out to verify that the vacancy concentration doesn't change dramatically as seen in fig. 4.8.

Therefore the structure to be used in the experiment is shown in fig. 4.9

It was decided to prepare several wafers to evaluate the following implanting conditions:

- energy 2 MeV, dose 1×10^{13} ions/cm^2
- energy 2 MeV, dose 1×10^{14} ions/cm^2
- energy 3 MeV, dose 1×10^{13} ions/cm^2
- energy 3 MeV, dose 1×10^{14} ions/cm^2

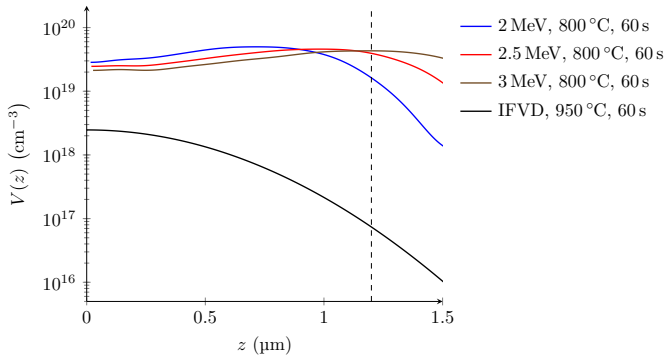

(a) Dose: 1×10^{13} ions/cm^2

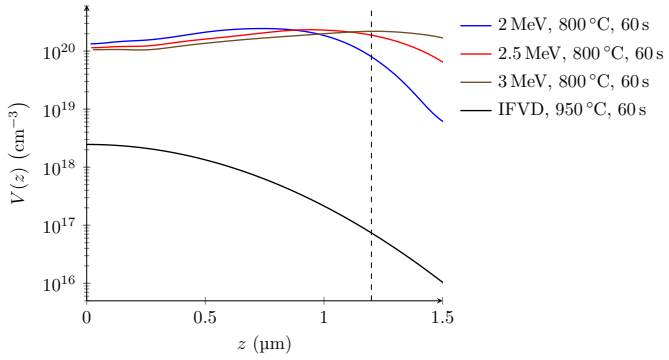

(b) Dose: 5×10^{13} ions/cm^2

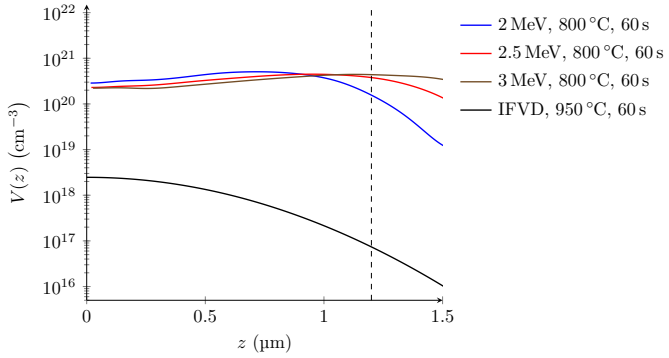

(c) Dose: 1×10^{14} ions/cm^2

Figure 4.6: Diffusion of Surrey vacancies with RTA 800 °C for 60 s. The dashed line represents the quantum well depth

After the implantation, both the Au mask and the Si_3N_4 protective layer will be removed. Samples will be cleaved from the wafers and, after the deposition of Si_3N_4 layers, they will be used to determine the optimal annealing conditions with temperatures ranging from 750 °C and 850 °C. Finally a whole fabrication process will be completed using these wafers and, from the resulting diodes, the different IID conditions will be compared.

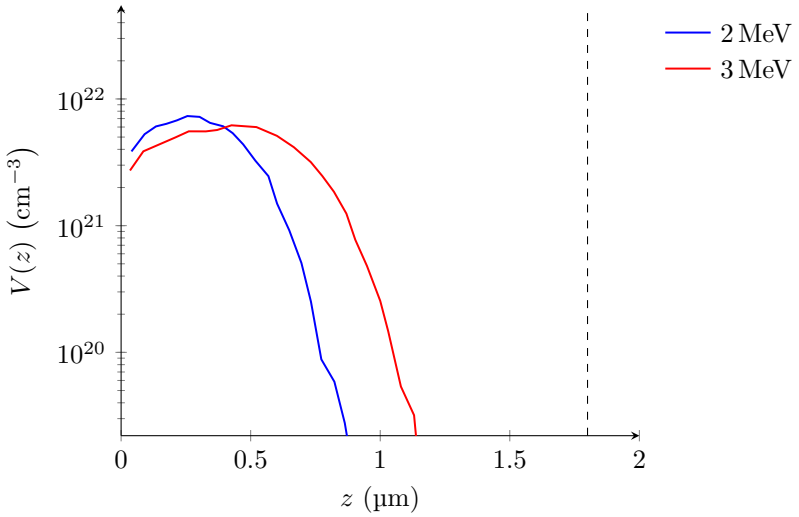

Figure 4.7: As implantation range in Au hard mask. The dashed line represent the surface of the Si_3N_4 layer

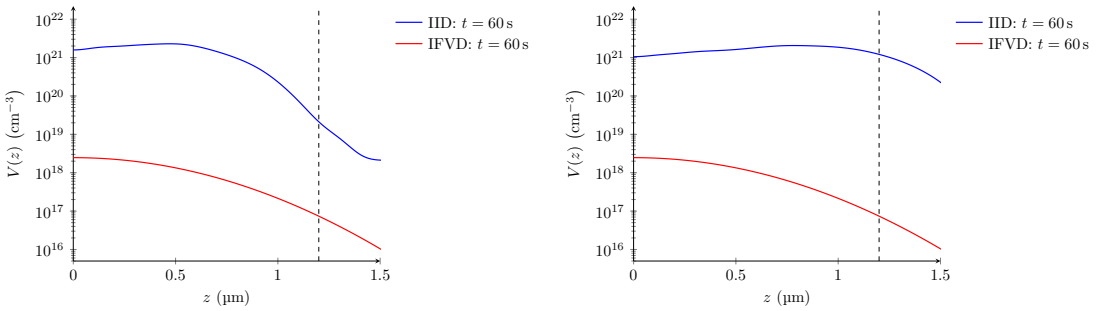

(a) Energy: 2 MeV, dose: 1×10^{13} ions/cm^2 (b) Energy: 3 MeV, dose: 1×10^{13} ions/cm^2

Figure 4.8: Vacancy profile through with 300 nm Si_3N_4 protective layer

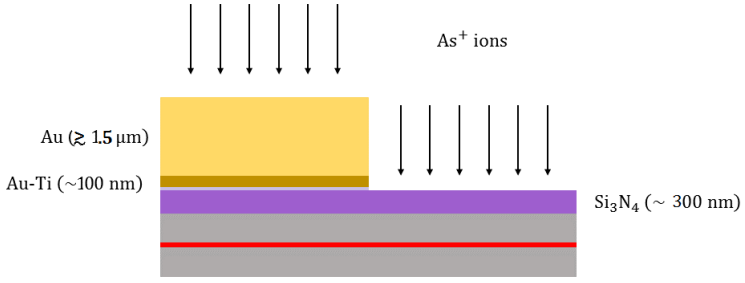

Figure 4.9: Structure for the IID process

Chapter 5

Experimental results

In the following sections the most significant measurements are reported: the thermal stability of the bare material, a comparison between side-by-side and SiO_2-over-Si_3N_4 dielectric structures and measurements on whole wafers.

5.1 Thermal stability

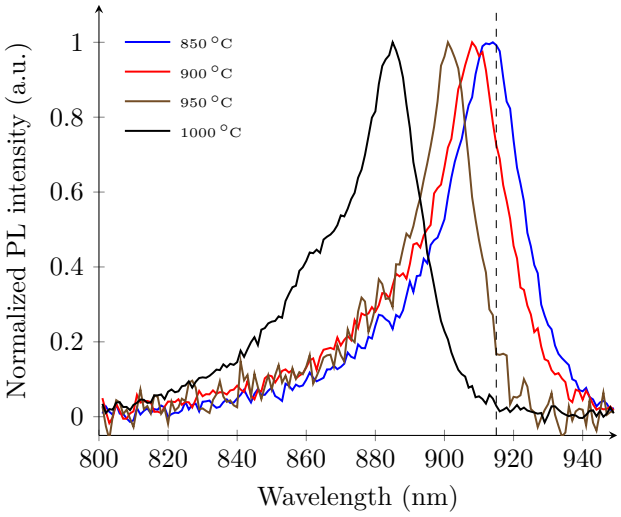

Figure 5.1: Example of PL measure on bare MBE side samples. The dashed line represents the initial PL emission wavelength

In fig. 5.1 is shown the increasing wavelength shift in MBE sample without dielectric caps. This experiment showed that the intermixing induced only by RTA reached up to 28.4 nm (45 meV) at 1000 °C. This results made clear that, to achieve significant intermixing in the NAM region while keeping the $\Delta\lambda$ in the cavity unchanged, techniques such as IFVD and IID were required.

5.2 Samples with patterned dielectrics

The measurements shown in figs. 5.2 and 5.3 presented respectively $\Delta\lambda_{SiO_2} = 56.7\,\text{nm} = 97.7\,\text{meV}$, $\Delta\lambda_{SiO_2} = 60.5\,\text{nm} = 105.2\,\text{meV}$ after annealing at 950 °C for 60 s. Although in literature [18] the reported wavelength shift were up to 130 meV, this experiment still showed a significant intermixing without compromising the Si_3N_4 protected region.

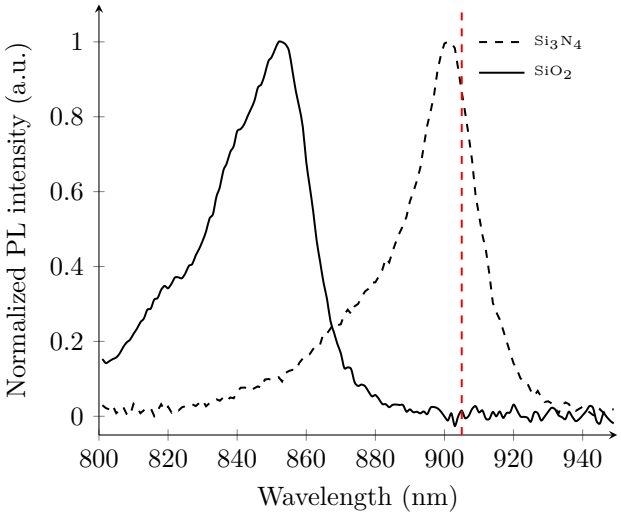

Figure 5.2: SiO_2-over-Si_3N_4 sample with $\Delta\lambda_{Net} = 50.2\,\text{nm}$

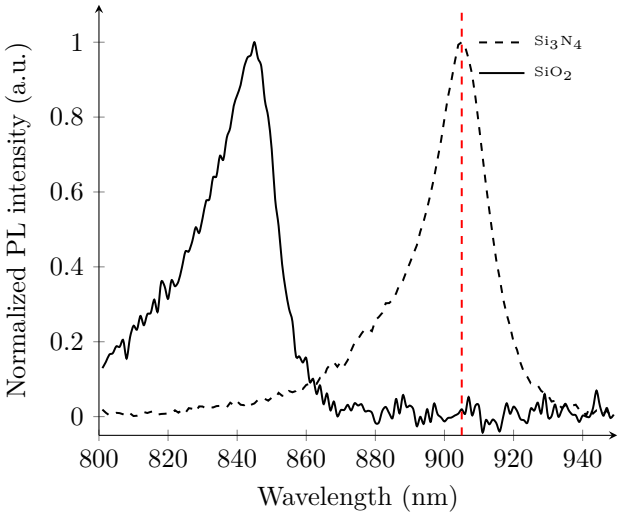

Figure 5.3: Side-by-side sample with $\Delta\lambda_{Net} = 60.5\,\text{nm}$

Moreover the two dielectric configurations proved to be almost equivalent, but the SiO_2-over-Si_3N_4 structure was preferred to simplify the fabrication process. Moreover, using these annealing conditions, $\Delta\lambda$ in excess of 40 nm were consistently achieved.

5.3 Whole wafers

The main results obtained on whole wafers were the control of the deformation during RTA, the wavelength shift and the performance of diodes with NAMs. More specifically the improved mechanical stability allowed to complete the whole-wafer fabrication process without cleaving part of the wafer and the measured wavelength shift corresponds to a significant reduction in the absorption of the NAM regions.

5.3.1 Mechanical stability

Wafers used to deform during RTA, possibly due to temperature gradients on the wafer caused by non-uniformity in the illumination within the RTA chamber.

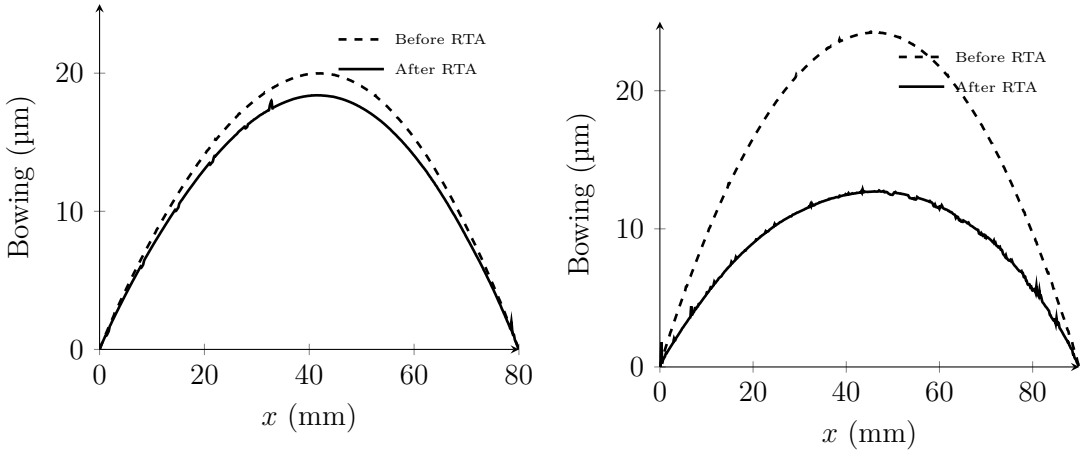

(a) 0°

(b) 90°

Figure 5.4: Wafer bowing

Depositing dielectric layers on both top and backside of the wafers, as explained in chapter 3, made possible the strong reduction of the deformation as seen in fig. 3.18 (figure duplicated here as fig. 5.4 for clarity). With this technique the wafers remain almost flat and manufacturable without complication for the fabrication process and also avoiding the desorption of As atoms from the material during RTA. It's also possible that properly configuring the rapid thermal annealer the deformation of the wafer could be completely avoided.

Even though the wafers are, in this way, able to mechanically withstand temperatures in excess of 950 °C, the current research is now focused on the IID process since it promises to achieve even greater intermixing with much lower temperatures. Moreover heating a InGaAs/AlGaAs at 950 °C may induce unwanted defects in the material so it should be possibly avoided.

5.3.2 PL shift

The wavelength shift measured on whole wafers was less than expected from the preliminary experiments on small samples, reaching only 15 nm (20.6 meV) on the RD006 wafer and 16.2 nm (22.1 meV) on the RD007 wafer. This is significantly less than the results reported in refs. [18], [20], [134]. A possible explanation is that the rapid thermal annealer was unable to reach 950 °C uniformly on the whole wafer due to the absence of graphite susceptors. This issue is currently under investigation.

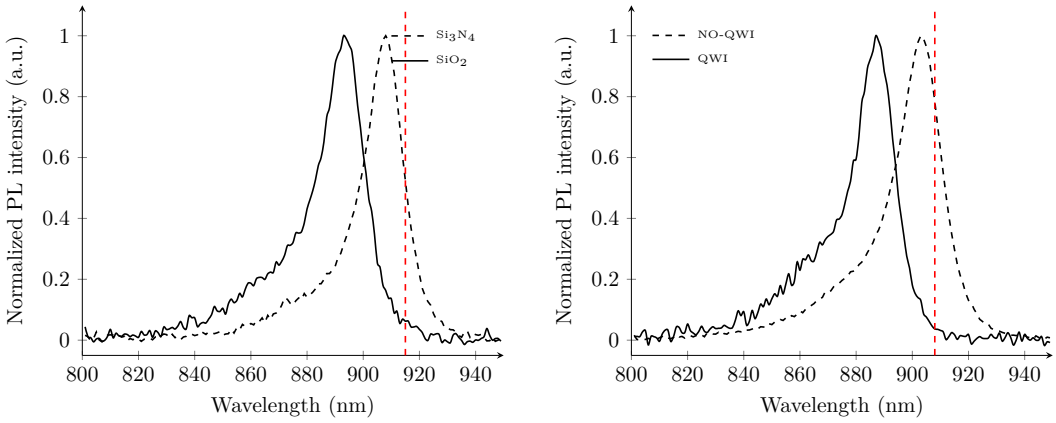

(a) RD006 (b) RD007

Figure 5.5: PL measurements on whole wafers

Even though the $\Delta\lambda$ was relatively small, the absorption reduction was estimated to be around 96% with respect to non-treated material. Both wafers in fig. 5.5 were annealed at 950 °C for 60 s and, depositing dielectrics on both top and backside, the flatness of the wafer RD007 was significantly improved with respect to the wafer RD006. In fact the deformation of wafer RD007 did not compromise the fabrication process.

5.4 Performance of intermixed diodes

The diodes from the RD006 process were characterized and their PI characteristic was measured under pulsed and CW operation.

In fig. 5.6 the PI characteristic was measured under pulsed operation in almost adiabatic conditions and around 30 W were achieved at 28 A. Comparing with ref. [18], in which 25.6 W were reached in pulsed (10 µs) operation with 28 A, the PI achieved in this work is slightly greater.

The diodes were then mounted on carriers and their characteristic was measured in CW operation, resulting in more stressing conditions due to the heating of the diodes. In this case only 50% of the NO-QWI diodes survived the test while all the QWI diodes successfully passed it.

Finally, diodes from both groups underwent burn-in tests and, as previously showed, 82% of the QWI diodes passed the test while the NO-QWI ones showed a yield of 25%.

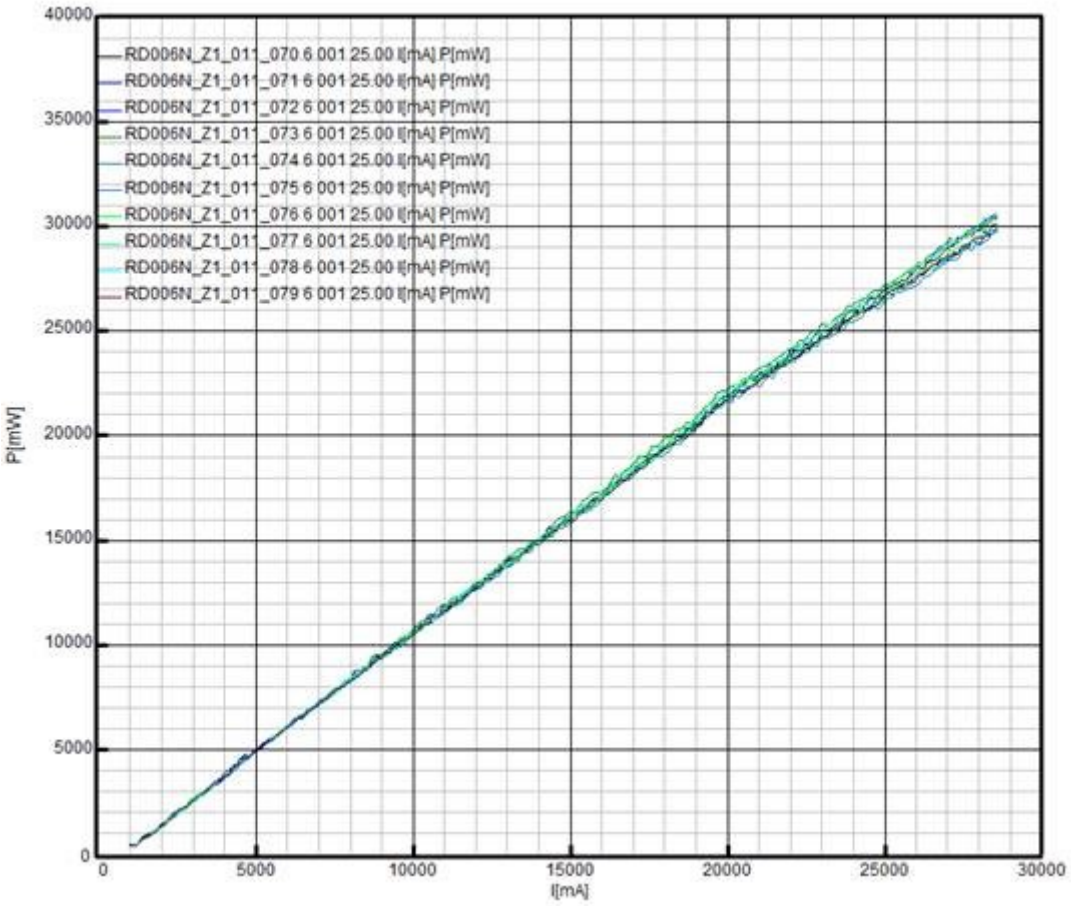

Figure 5.6: RD006: PI measurement under pulsed operation

The RD008 process, in which the deformation during RTA was kept under control through the deposition of dielectric layers on both side of the wafer, was completed and diodes from both QWI and NO-QWI groups underwent the burn-in tests. The NO-QWI devices presented a yield of 71%, thus within the production specifications, with COMD taking place in the first 10 hours. Finally, QWI diodes had an yield of 78% and the first COMD took place almost at the end of the test. So the NAM devices showed an increased resistance with respect to standard ones from the same wafer in a non-compromised process.

Conclusions and future work

The aim of this thesis was the investigation of different techniques to realize non-absorbing mirrors (NAMs) in InGaAs/AlGaAs high power-laser diodes, with a particular attention for the eventual integration of this technology in the current industrial production. From the study of literature three different approaches to induce compositional disordering have been selected: impurity-free vacancy diffusion (IFVD), Ar plasma bombardment and impurity-induced disordering (IID). In particular the IFVD process, due its simplicity, was the most promising technique.

The effect of quantum well intermixing has been evaluated on samples of $2\,cm^2$ using room temperature PL measurements in order to determine the optimal process parameters and annealing conditions to achieve the maximum intermixing, while striving to maintain compatibility with the current production process. The main investigated parameters were the dielectric material used for the cap, its thickness, the dielectric pattern and the RTA conditions.

The optimal process conditions were determined to be a SiO_2-over-Si_3N_4 dielectric structure, both layers with thickness around 150 nm and annealing for 60 s at 950 °C. These conditions allowed to consistently reach over 40 nm shift of the PL wavelength in region covered only by the SiO_2 layer, while in those with the SiO_2-over-Si_3N_4 structure the $\Delta\lambda$ did not exceed 5 nm. These conditions were transferred to whole 4-in wafers and a complete fabrication process was carried out to evaluate the effectiveness of the NAM regions in the high-power laser diodes.

The wavelength shift was inferior to the expectations, achieving only $\Delta\lambda_{Net} = 15\,nm$, but it allowed the realization of NAM with 96% reduction of the absorption at the laser emission wavelength. Moreover, the wafer presented a significant deformation which compromised the fabrication process. Although several issues were present, the NAM devices were able to reach around 30 W at 28 A under pulsed operation.

Adjustments to control the wafer deformation were investigated and a new whole-wafer process was carried out. These adjustments improved the mechanical stability of the wafers during RTA without complicating the fabrication process. This, in turn, makes possible to continue the investigation of quantum well intermixing using IID as an alternative technique.

The ongoing and future work is mainly focused on IID, using high-energy As^+ implantation, possibly coupled with IFVD [132]; however other investigations can prove useful to increase the catastrophic optical mirror damage (COMD) threshold in high-power laser diodes. In particular improving the IFVD process by increasing the wavelength shift seems possible: reducing the intermixing in Si_3N_4-protected region through an oxygen plasma

treatment [93], [135], [136] would allow to achieve greater $\Delta\lambda_{\text{Net}}$ while also reducing the wavelength shift in the nominally non-intermixed regions. Another improvement to the IFVD process would be using sputtering, instead of PECVD, to deposit SiO_2 that in literature [137] is reported to achieve greater $\Delta\lambda$ with lower RTA temperatures. Another possible investigation area would be using only Si_3N_4 layers both to suppress and enhance the intermixing according to the deposition conditions [18], [49]. Finally, other possibilities could be photo-absorption induced disordering (PAID, p-PAID), that was used in academia to achieve quantum well intermixing in InGaAsP materials [87], [138], and using multiple RTAs [139].

In conclusion the results obtained during this thesis were promising and the research is continuing to achieve more effective NAMs without compromising nor excessively complicating the current fabrication process.

Appendix A

Equipment

A.1 RF-PECVD

The plasma enhanced chemical vapour deposition (PECVD) is a widely used deposition technique that allows the growth of amorphous and micro-crystalline thin films at low temperature.

The equipment, schematically represented in fig. A.1, consists of

- a vacuum chamber with a basis pressure in the low 1e-4mTorr, in which reactive gases are injected with a controlled flow;
- two electrodes inside the chamber at which a RF (radiofrequency) potential, usually 13.56 MHz is applied.

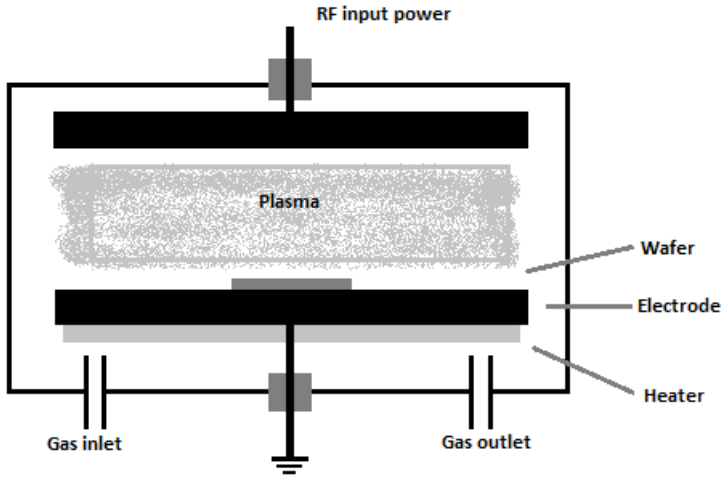

Figure A.1: PECVD schematic representation

The RF potential is used to ignite and sustain the cold plasma between to parallel electrodes. The precursor gases injected in the chamber are excited to plasma state forming

radicals that react together and the resulting compound is deposited to both reactor walls and substrate. The characteristics of the deposited film depend on the deposition conditions, in particular on the RF power and frequency, partial pressures of the gases, gas flows, etc. The stress of the film can be controlled using a second generator at 108 kHz.

This technique is an improvement on the traditional chemical vapour deposition (CVD) since the energy needed for the reaction is given only partially by the substrate heating, but more significantly by the plasma state which provides the ionization of the gases. In this way it's possible to realize depositions at much lower temperatures, which is fundamental for processes on III-V semiconductors.

In this work the PECVD shown in fig. A.2 has been used to deposit both Si_3N_4 and SiO_2 obtained from the reaction of silane SiH_4, nitrogen N_2 and nitrous oxide N_2O.

Figure A.2: PECVD

A.2 RIE and ICP-RIE

The reactive ion etching (RIE) is a dry etching technology where a RF potential is used to excite the formation of a plasma. Reactive gases injected into the chamber are excited to plasma state forming neutral and ionized radicals thus realizing both chemical and physical etching of the material. Applying a bias potential to the electrodes it's possible to have an highly anisotropic etching. The interaction between substrate and neutral radicals forms volatile compounds removed by the pumping system.

The inductively coupled RIE (ICP-RIE) allows to control independently the plasma density and the ion acceleration. The ICP coupling exploits the fields (magnetic and electric) generated by a RF current flowing in a solenoid and the resulting plasma densities can be increased by a factor 10^3 while the independent ion acceleration is achieved by applying a RF bias. In this way it's possible to have conditions such as high plasma density but low ion bombardment and vice versa.

(a) RIE

(b) ICP-RIE

Figure A.3: Reactive ion etching equipment

In this work the RIE (fig. A.3a) has been used extensively to prepare samples for the photoluminescence measure while the ICP-RIE (fig. A.3b) was used to investigate the intermixing induced by Ar^+ bombardment.

A.3 Rapid thermal annealing (RTA)

The rapid thermal annealing (RTA) uses lamp heating to rapidly heat wafer to extremely high temperatures, exceeding 1000 °C, with ramps of 150 °C s^{-1}. In this way the processing time is extremely reduced with respect to to more conventional annealing furnaces which, in turn, limits the redistribution of dopant atoms in the material. However it's also possible to have excessive temperature gradients across the wafer that may result in a significant deformation. This equipment was initially developed for ion implantation since it allows both to activate the dopants and to recover the crystalline damage. It can also be used for thermal oxidation, silicide formation and other applications.

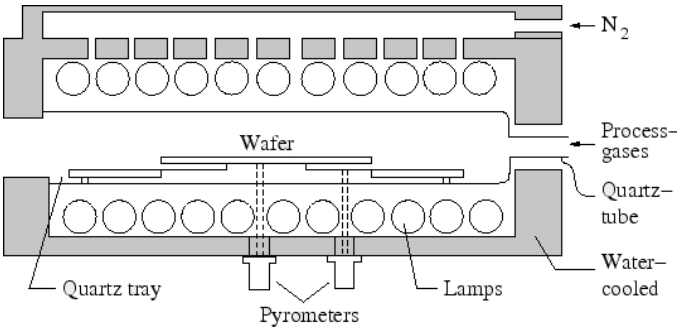

Figure A.4: RTA schematic representation from http://www.iue.tuwien.ac.at/phd/hollauer/node13.html

RTP systems consist generally of tungsten-halogen lamps that act as heat sources and

placed all around the process wafer in order to have a good uniformity in the heat treatment. The temperature can be measured by thermocouples in direct contact with the wafer or optically using pyrometers.

In this work RTA has been extensively used to activate the compositional intermixing caused by IFVD using ramps of 25 °C/s under N_2 flow.

Figure A.5: Rapid thermal annealer from www.ssi-rtp.com

Since As atoms tend to evaporate from the material at temperatures around 950 °C, the process wafer is sandwiched between a Si carrier and GaAs with a Si_3N_4 cap.

A.4 Filmetrics

The Filmetrics shown in fig. A.6 is an instrument used to measure thin-film characteristics from the spectral reflectance of the sample, in particular thin-film thickness and refractive index. This technique is non-destructive, requires little sample preparation and it's very accurate measuring single layer or multilayers with layer thickness greater than 50 nm, otherwise the spectral reflectance measure may be unable to give a satisfactory result.

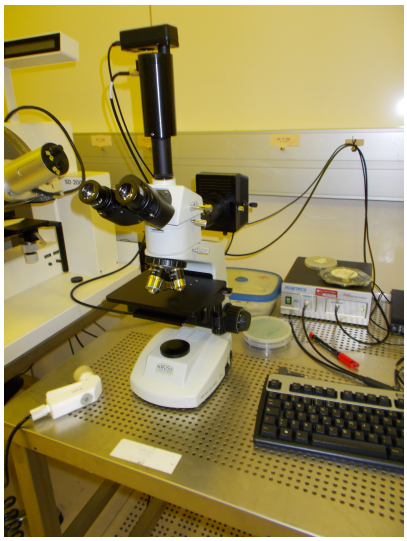

Figure A.6: Filmetrics

In this thesis the instrument has been used to evaluate the thickness of deposited SiO_2 and Si_3N_4 thickness ranging from 150 nm up to 500 nm.

A.5 Photoluminescence (PL)

Photoluminescence (PL) is a measurement technique for the optical characterization of semiconductor materials evaluating the bandgap and the defectivity of the crystal. Its principle is the absorption of incident light with energy higher than the bandgap which excites electrons from the valence band (VB) to the conduction band (CB). These electrons go through thermalization and reach the bound states of the quantum well under analysis, finally photons are emitted through radiative recombination and collected. Using a monochromator a spectral measurement is performed while the PL intensity is related to the defectivity of the material.

In this work PL has been used to evaluate the wavelength shift caused by the compositional disordering by measuring the PL spectrum. This requires the removal of 1 µm of p-doped absorbing material from the sample in order to enhance the radiative recombination in the quantum well layer. The used experimental set-up consists of a visible laser source used to excite the PL, a monochromator to measure separately each spectral component and a photodetector. A lock-in amplifier is used to detect low photocurrent signal.

A.6 PL set-up

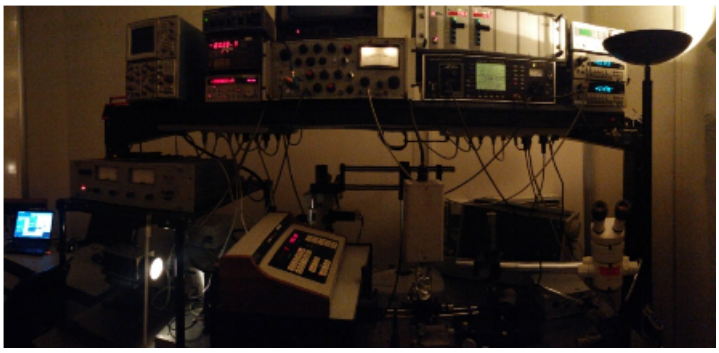

Figure A.7: Photoluminescence set-up

The PL set-up shown in fig. A.7 has been used in this thesis to perform single-point measurements of PL spectra. It consists of a visible laser source emitting around 660 nm, a chopper connected to a lock-in amplifier, a camera for the alignment of the sample and a monochromator for the spectral analysis.

A.6.1 Spatially-resolved photoluminescence

In intermixed wafers for high-power laser fabrication the wavelength shift needs to be spatially localized, so a measurement set-up for the PL-map was developed. It consists of a

808 nm laser source, a monochromator controlled with an Arduino board and a XY-translator for the sample movement.

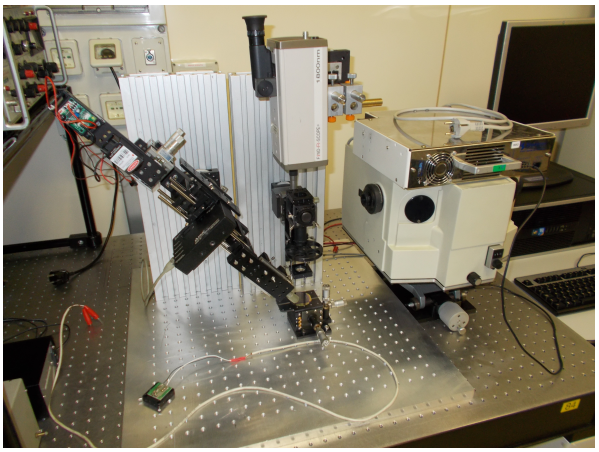

Figure A.8: Experimental set-up without the XY-translator

Arduino-controlled monochromator

A monochromator Jobin-Yvon HR250 was available for the experimental set-up, controlled by a stepper motor with step angle 0.36°and pulse-per-second PPS $= 0 \div 280$. In order to automate spectral measurements it was decided to control its stepper motor through an external Arduino board.

The Arduino was programmed to receive as input the number of steps and to send a digital signal to a stepper motor driver TB6600 (fig. A.9). In this way it was possible to interface the device with a LabView program which controls both the monochromator movement and the measurement instruments.

Calibration

Once it became possible to control the monochromator movement using a LabView program, the instrument needed to be calibrated using sources of known wavelength: a 632.8 nm He-Ne laser and a 780 nm semiconductor laser.

Therefore the system was configured to acquire photocurrent from a photodiode as a function of the number of steps made by the motor from a reference laser source as seen in fig. A.11. In order to do a linear fit three peaks were measured corresponding to the first two harmonics of the He-Ne laser and the first harmonic of the semiconductor laser.

From fig. A.12 the calibration curve of the monochromator was determined using a linear fit

$$\lambda(x) = 40.146\,\mathrm{pm/step} \cdot x + 341.24\,\mathrm{nm} \tag{A.1}$$

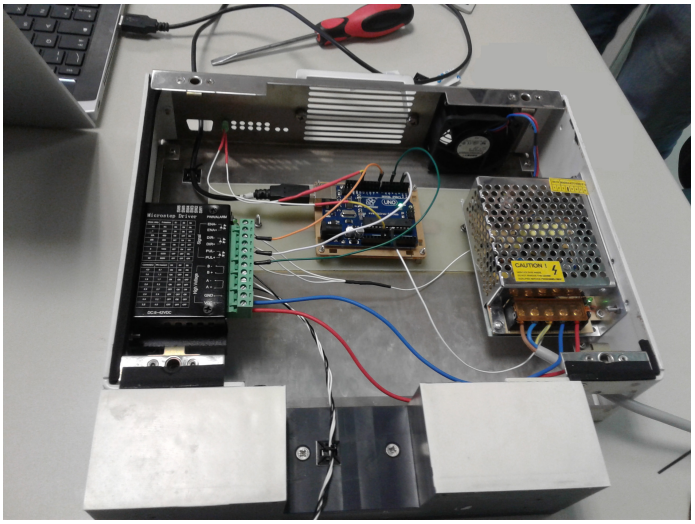

Figure A.9: Stepper motor control with Arduino board

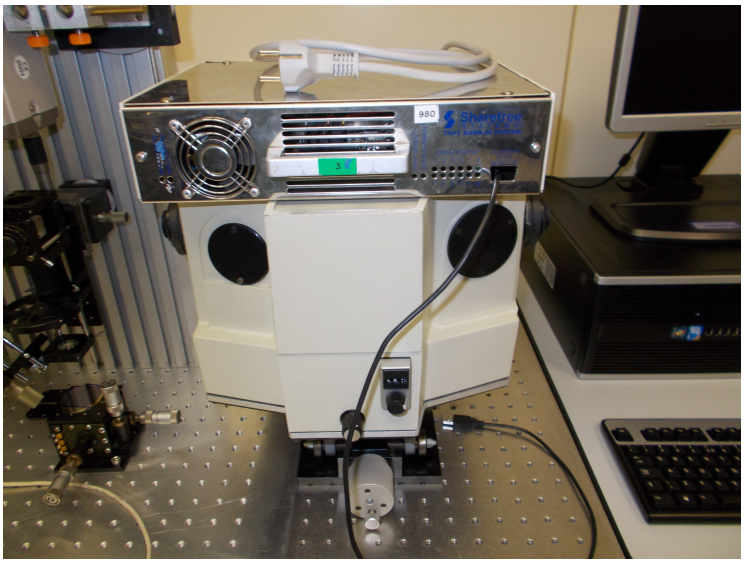

Figure A.10: Monochromator controlled by Arduino

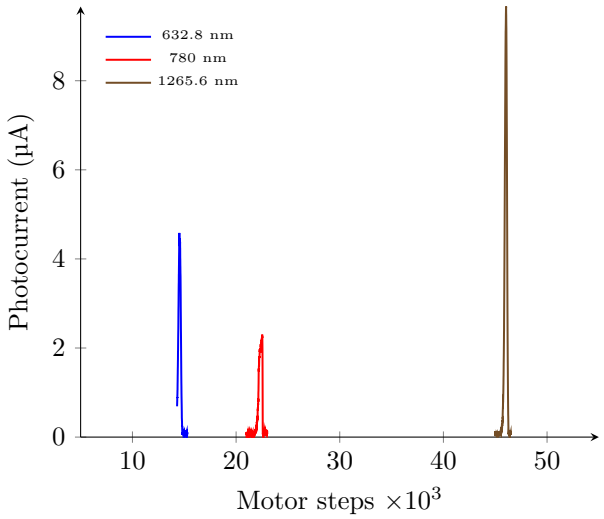

Figure A.11: Monochromator calibration

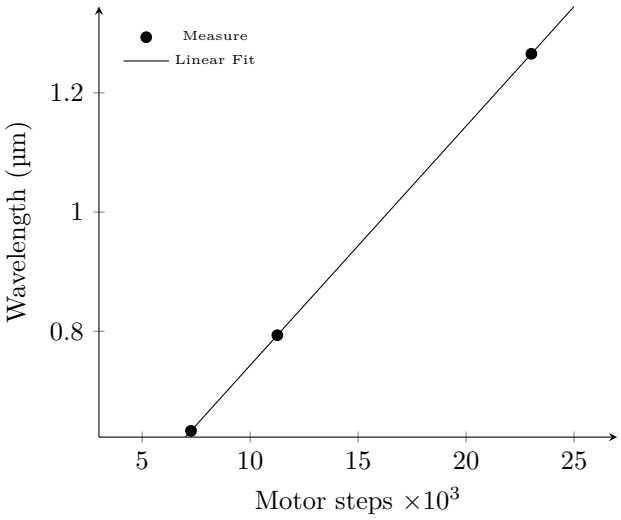

Figure A.12: Monochromator calibration curve $\lambda(x) = 40.146\,\mathrm{pm/step} \cdot x + 341.24\,\mathrm{nm}$

Appendix B

Finite element method

The finite element method (FEM) is a numerical technique used solve a wide spectrum of problem described by partial differential equations (PDEs), ranging from structural mechanics to electromagnetics. The solution of the problem is approximated as a system of algebraic (steady-state problems) or ordinary differential equations (transient problems) obtained from the discretization of the domain. In this way FEM can handle complex geometries with relative ease and include local effects.

In this work FEM has been used to solve both eigenvalue problems, the 1D-stationary Schrödinger equation [140], and transient problems [141] in the form of diffusion equation.

B.1 Basics

The stages involved in the FEM solution of PDEs can be described as follows:

1. identify the PDE associated with a physical phenomenon and the relevant boundary and initial conditions;

2. express the PDE in an equivalent integral form known as weak formulation;

3. discretize the weak form over the domain of interest;

4. solve a system of ODEs or algebraic equation.

As an example, the FEM procedure is applied to the following 1D-problem defined in the interval [0,1]

$$-u''(x) = f(x) \tag{B.1}$$

The known term $f(x)$ is assumed to square-integrable in (0,1) that is

$$f(x) \in L^2(0,1) \longleftrightarrow \int_0^1 |f(x)|^2 \, \mathrm{d}x < \infty$$

which implies the continuity of both u and u' is this domain.

B.1.1 Weak formulation

The solution of variational problem, which is approximated using FEM, belongs to the Sobolev space defined as

$$H^k(0,1) = \left\{ u(x) : \int_0^1 \left| u^{(i)}(x) \right|^2 \mathrm{d}x < \infty,\ 0 \le i \le k \right\}, \quad k \ge 1$$

so u and all its derivatives up to the $k-1$ order are continuous in (0,1).

Equation (B.1) can be reformulated in an integral form (weak form) by multiplying each term with a test function $v(x)$ also belonging to the H^1. Depending on the boundary conditions (Dirichlet boundary conditions), v instead can belong to the subset of H^1 where $v(0) = v(1) = 0$.

$$-\int_0^1 u''(x)v(x)\,\mathrm{d}x = \int_0^1 f(x)v(x)\,\mathrm{d}x$$

Applying the integration by parts the weak formulation is derived

$$\int_0^1 u'(x)v'(x)\,\mathrm{d}x - u'(x)v(x)\Big|_0^1 = \int_0^1 f(x)v(x)\,\mathrm{d}x \tag{B.2}$$

So the test function v acts a weight function and the problem is relaxed to an averaged version of the initial PDE and the solution u is searched in $H^1(a,b)$.

B.1.2 Galerkin discretization

Since a numerical solution is searched, it is not possible to use the infinite-dimension Sobolev spaces H^2 and H^1 but the solution space is restricted to their finite subspace H_h^1. Therefore the Galerkin discretization can be obtained as follows

$$\int_0^1 u_h'(x)v_h'(x)\,\mathrm{d}x - u_h'(x)v_h(x)\Big|_0^1 = \int_0^1 f(x)v(x)\,\mathrm{d}x \tag{B.3}$$

where $h > 0$, $h \to 0$ so that $u \approx u_h$ and $v \approx v_h$.

Since both u_h and v_h belong to the linear space H_h^1 they can be expressed as a linear combination of basis elements $\varphi_{i,j}$ where N is the number of subintervals of the spatial mesh:

$$u(x) \approx x_h(x) = \sum_{j=1}^{N} c_j \varphi_j(x)$$
$$v(x) \approx v_h(x) = \sum_{i=1}^{N} c_i \varphi_i(x)$$

so the eq. (B.3) is now finding the proper coefficients $\{c_j\}$.

$$\sum_{j=1}^{N} c_j \int_0^1 \varphi_j'(x)\varphi_i'(x)\,\mathrm{d}x - \sum_{j=1}^{N} c_j \varphi_j'(x)\varphi_i(x)\Big|_0^1 = \sum_{j=1}^{N} \int_0^1 f(x)\varphi_i(x)\,\mathrm{d}x \quad \forall i = 1:N \tag{B.4}$$

This equation can be equivalently cast in matrix form

$$[K]\{u\} = \{f\}$$

where $[K]$ is called stiffness matrix and all its element are the result of an integral.

B.1.3 Piecewise polynomial approximation

The basis elements φ in eq. (B.4) belong to $H_h^1 \subset H^1$ and, in order to reduce the computational complexity in the assembling of each matrix element, the stiffness and mass matrices should be highly sparse, meaning the basis elements must have very small support. So a proper choice of the basis will simplify the evaluation of the matrix elements.

Several possible choices exist, the simplest being the Lagrangian basis which belongs to the space of piecewise polynomial functions. In this work only the 1st order polynomials have been used and they are given by

$$\varphi_1(z) = \begin{cases} \frac{z_2 - z}{z_2 - z_1} & z_1 \leq z \leq z_2 \\ 0 & \text{else} \end{cases}$$

$$\forall i = 2 : N \qquad \varphi_i(z) = \begin{cases} \frac{z - z_{i-1}}{z_i - z_{i-1}} & z_{i-1} \leq z \leq z_i \\ \frac{z_{i+1} - z}{z_{i+1} - z_i} & z_i \leq z \leq z_{i+1} \\ 0 & \text{else} \end{cases}$$

$$\varphi_{N+1}(z) = \begin{cases} \frac{z - z_N}{z_{N+1} - z_N} & z_N \leq z \leq z_{N+1} \\ 0 & \text{else} \end{cases}$$

which make the stiffness matrix tridiagonal, symmetric and positive definite.

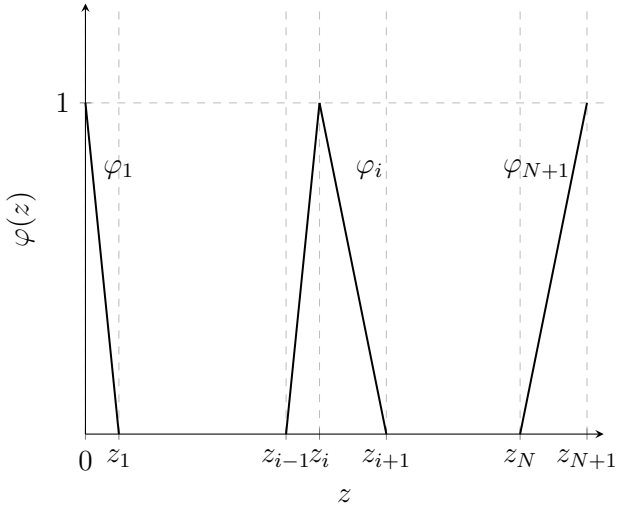

Figure B.1: 1st order Lagrangian basis

So the solution u is approximated in each mesh element assuming by the basis functions interpolate the unknown variables, schematically represented in fig. B.2.

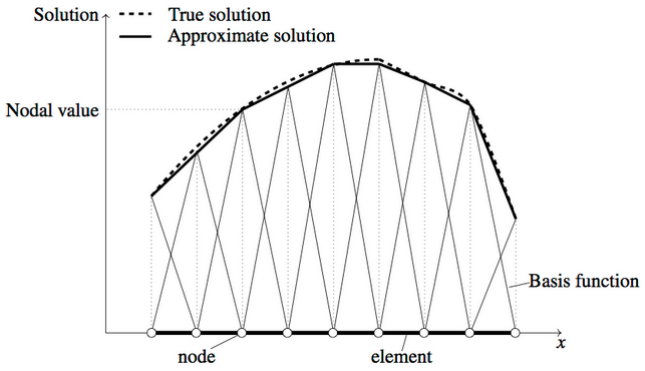

Figure B.2: Schematic representation of the FEM approximation

According to the chosen basis the error can be estimated as

$$\|u - u_h\|_{H^1} = \mathcal{O}\left(h^1\right)$$

B.2 Stationary Schrödinger equation

The bound states of a finite potential well can be determined solving the 1D-stationary Schrödinger equation according to the FEM procedure explained previously. So the PDE is expressed by

$$-\frac{\hbar^2}{2}\frac{\partial}{\partial z}\left(\frac{1}{m^*}\frac{\partial \psi}{\partial z}\right) + U\psi = E_n\psi \;\; \frac{1}{m^*}\frac{\partial \psi}{\partial z}\bigg|_{z_1}^{z_N} = 0 \tag{B.5}$$

where effective mass m^*, potential U and wavefunction ψ depend on the position z. The eigenvalues E_n of this equation are the bound state energies of the quantum well. The weak formulation is obtained multiplying with the test function $v(z)$ belonging to $H^1(a,b)$ and integrating over the whole domain with homogeneous Neumann boundary conditions

$$-\frac{\hbar^2}{2}\int_a^b \frac{\partial}{\partial z}\left(\frac{1}{m^*}\frac{\partial}{\partial \psi}\right) v \,\mathrm{d}z + \int_a^b U\psi v \,\mathrm{d}z = E\int_a^b \psi v \,\mathrm{d}z$$
$$\frac{1}{m^*}\frac{\partial \psi}{\partial z}\bigg|_a^b = 0$$

Also homogeneous Dirichlet boundary conditions could be used, however this requires an additional manipulation of the final matrices. Finally applying the integration by part the variational form is derived:

$$\frac{\hbar^2}{2}\int_a^b \frac{1}{m^*}\frac{\partial \psi}{\partial z}\frac{\partial v}{\partial z}\,\mathrm{d}z + \int_a^b U\psi v \,\mathrm{d}z = E\int_a^b \psi v \,\mathrm{d}z \tag{B.6}$$

This equation is then discretized

$$\frac{\hbar^2}{2}\int_a^b \frac{1}{m^*}\frac{\partial \psi_h}{\partial z}\frac{\partial v_h}{\partial z}\,\mathrm{d}z + \int_a^b U\psi_h v_h \,\mathrm{d}z = E\int_a^b \psi_h v_h \,\mathrm{d}z \tag{B.7}$$

where $h > 0$, $h \to 0$ so that $\psi \approx \psi_h$ and $v \approx v_h$.

Since both ψ_h and v_h belong to the linear space H_h^1 they can be expressed as a linear combination of basis elements $\varphi_{i,j}$ where N is the number of subintervals of the spatial mesh:

$$\psi(z) \approx \psi_h(z) = \sum_{j=1}^{N} c_j \varphi_j(z)$$
$$v(z) \approx v_h(z) = \sum_{i=1}^{N} c_i \varphi_i(z)$$

which leads to

$$\frac{\hbar^2}{2} \sum_{j=1}^{N} c_j \int_a^b \frac{1}{m^*} \varphi_j' \varphi_i' \,\mathrm{d}z + \sum_{j=1}^{N} c_j \int_a^b U \varphi_j \varphi_i \,\mathrm{d}z = E \sum_{j=1}^{N} c_j \int_a^b \varphi_j \varphi_i \,\mathrm{d}z \quad \forall i = 1 : N \tag{B.8}$$

Restricting (B.8) within a single mesh element and assuming that the effective mass and the potential are constant in each element

$$\frac{\hbar^2}{2m_e^*} \sum_{j=1}^{N} c_j \int_e \varphi_j' \varphi_i' \,\mathrm{d}z + \sum_{j=1}^{N} c_j U_e \int_e \varphi_j \varphi_i \,\mathrm{d}z = E \sum_{j=1}^{N} c_j \int_e \varphi_j \varphi_i \,\mathrm{d}z \quad \forall i = 1 : N \tag{B.9}$$

This equation can be equivalently cast in matrix form

$$\frac{\hbar^2}{2m_e^*} \Big([K]_e + U_e [M]_e \Big) \{c_j\}_e = E [M]_e \{c_j\}_e$$

and by summing over the mesh elements a generalized eigenvalue problem is finally obtained

$$\sum_e \left(\frac{\hbar^2}{2m_e^*} \Big([K]_e + U_e [M]_e \Big) \right) \{c_j\}_e = E \sum_e [M]_e \{c_j\}_e \tag{B.10}$$

where $[K]$ and $[M]$ are, respectively, stiffness and mass matrix.

Using 1st order Lagrangian polynomials as basis functions each mesh element contributes to these matrices with

$$[M]_e = \frac{l_e}{6} \begin{bmatrix} 2 & 1 \\ 1 & 2 \end{bmatrix}$$
$$[K]_e = \frac{1}{l_e} \begin{bmatrix} 1 & -1 \\ -1 & 1 \end{bmatrix}$$

where l_e is the length of each mesh element.

B.3 Diffusion

The diffusion equation is solved using the method of lines, in which the spatial variable is discretized using FEM and the time variable is left continuous thus leading to a system of ordinary differential equations (ODEs).

Considering the following diffusion equation and its boundary conditions in the domain $[0, d]$

$$\frac{\partial}{\partial t}C(z,t) = D\frac{\partial^2}{\partial z^2}C(z,t) \tag{B.11}$$

$$\frac{\partial}{\partial z}C(z,t)\bigg|_{z=0} = 0 \quad \forall t \leq 0 \tag{B.12}$$

$$\frac{\partial}{\partial z}C(z,t)\bigg|_{z=d} = 0 \quad \forall t \leq 0 \tag{B.13}$$

$$C(z, t=0) = C_0(x) \quad \forall x \tag{B.14}$$

The weak formulation is given by

$$\int_0^d \frac{\partial C}{\partial t} v \, \mathrm{d}z = -D \int_0^d \frac{\partial C}{\partial z}\frac{\partial v}{\partial z} \, \mathrm{d}z \tag{B.15}$$

thus discretizing the space variable

$$\sum_{j=1}^{N} \frac{\partial c_j}{\partial t} \int_0^d \varphi_j \varphi_i \, \mathrm{d}z = -D \sum_{j=1}^{N} c_j \int_0^d \frac{\partial \varphi_j}{\partial z}\frac{\partial \varphi_i}{\partial z} \, \mathrm{d}z \quad i = 1 : N \tag{B.16}$$

Equation (B.16) can be expressed in matrix form

$$[M]\,\frac{\partial}{\partial t}\{c\} = -D\,[K]\,\{c\} \tag{B.17}$$

with $[K]$ and $[M]$ respectively stiffness and mass matrix. So a system of ODEs has been obtained which approximates the original transient problem. To solve each ODE several numerical methods are available, in this work the time variable has been approximated using the Crank-Nicolson method [142] so eq. (B.17) can be expressed as

$$\left(\frac{1}{\Delta t}[M] + \frac{1}{2}[K]\right)\{C_{k+1}\} = \left(\frac{1}{\Delta t}[M] - \frac{1}{2}[K]\right)\{C_k\} \tag{B.18}$$

Appendix C

Experiments summary

Wafer	T (°C)	t (min)	Dielectrics	Si_3N_4 (nm)	SiO_2 (nm)	$\Delta\lambda_{Net}$ (nm)
MOCVD (9)	800	1	-	-	-	0.4
MOCVD (9)	850	1	-	-	-	1.5
MOCVD (9)	950	1	-	-	-	21.4
MBE (10)	850	1	-	-	-	0.1
MBE (10)	900	1	-	-	-	4.3
MBE (10)	950	1	-	-	-	11.7
MBE (10)	1000	1	-	-	-	28.4
MOCVD (9)	750	1	-	-	330	0.1
MOCVD (9)	800	1	-	-	330	1.1
MOCVD (9)	850	1	-	-	330	2.9
MOCVD (9)	900	1	-	-	330	9.8
MOCVD (9)	950	1	-	-	330	53.3
MOCVD (9)	1000	1	-	-	330	94.6
MOCVD (9)	800	1	-	156	-	0.4
MOCVD (9)	850	1	-	156	-	0.7
MOCVD (9)	950	1	-	156	-	4.2
MBE (10)	850	1	-	-	150	1.0
MBE (10)	900	1	-	-	150	8.5
MBE (10)	950	1	-	-	150	50.2
MBE (10)	1000	1	-	-	150	66.8
MBE (10)	850	1	-	156	-	0.1
MBE (10)	900	1	-	156	-	1.7
MBE (10)	950	1	-	156	-	4.8
MBE (10)	1000	1	-	156	-	14.7
MOCVD (9)	800	1	-	-	330 (T)	1.3
MOCVD (9)	850	1	-	-	330 (T)	1.3
MOCVD (9)	900	1	-	-	330 (T)	9.6
MOCVD (9)	950	1	-	-	330 (T)	48.6

Table C.1: Thermal stability and single dielectric

Wafer	T (°C)	t (min)	Dielectrics	Si_3N_4 (nm)	SiO_2 (nm)	$\Delta\lambda_{Net}$ (nm)
MOCVD (7b)	900	1	side-by-side	156	330	-0.2
MOCVD (7b)	925	1	side-by-side	156	330	9.7
MOCVD (7b)	950	1	side-by-side	156	330	19.4
MOCVD (10)	925	1	side-by-side	156	330	25.6
MOCVD (10)	950	1	side-by-side	156	330	53.3
MOCVD (10)	950	1	side-by-side	156	330	60.6
MOCVD (10)	950	1	side-by-side	156	330	53.4
MOCVD (7b)	900	1	SiO_2-over-Si_3N_4	156	150	2.1
MOCVD (7b)	950	1	SiO_2-over-Si_3N_4	156	150	17.7
MOCVD (7b)	900	1	SiO_2-over-Si_3N_4	156	330	0.9
MOCVD (7b)	950	1	SiO_2-over-Si_3N_4	156	330	13.2
MOCVD (10)	950	1	SiO_2-over-Si_3N_4	156	150	45.8
MOCVD (10)	950	1	SiO_2-over-Si_3N_4	156	150	50.2
MOCVD (10)	950	1	SiO_2-over-Si_3N_4	156	330	51.1
MOCVD (10)	950	1	SiO_2-over-Si_3N_4	156	330	45.9

Table C.2: Dielectric pattern

Wafer	T (°C)	t (min)	Dielectrics	Si_3N_4 (nm)	SiO_2 (nm)	$\Delta\lambda_{Net}$ (nm)
MOCVD (10)	850	5	SiO_2-over-Si_3N_4	156	150	7.5
MOCVD (10)	900	5	SiO_2-over-Si_3N_4	156	150	42.6
MBE (10)	900	1	SiO_2-over-Si_3N_4	156	150	5.8
MBE (10)	900	2	SiO_2-over-Si_3N_4	156	150	10.6
MBE (10)	900	3	SiO_2-over-Si_3N_4	156	150	20.3
MBE (10)	925	2	SiO_2-over-Si_3N_4	156	150	21.3
MBE (10)	950	3	SiO_2-over-Si_3N_4	156	150	35.9

Table C.3: RTA conditions: temperature T and time t

Wafer	T (°C)	t (min)	Dielectrics	Si_3N_4 (nm)	SiO_2 (nm)	$\Delta\lambda_{Net}$ (nm)
RD006 (10)	950	1	SiO_2-over-Si_3N_4	156	150	15
MBE_A (9)	950	1	SiO_2-over-Si_3N_4	156	150	16.2
MBE_B (9)	950	2	SiO_2-over-Si_3N_4	156	150	32.8
RD007 (9)	950	1	SiO_2-over-Si_3N_4	156	150	-
RD008 (9)	950	1	SiO_2-over-Si_3N_4	156	150	-

Table C.4: Whole 4-in wafers

Appendix D

Listings

D.1 Arduino code to control the stepper motor

```
#include <math.h>

// defines pins numbers
const int stepPin = 5;
const int dirPin = 2;
const int enPin = 8;

const float k = 1;                                          // calibration parameter [steps/nm]
const float Epsilon = 0;                                    // initial error
const float pps = 280;                                      // motor pulse-per-second
float CurrentPosition;


void setup(){
    Serial.begin(9600);
    // Set pins type and status
    pinMode(stepPin, OUTPUT);
    pinMode(dirPin, OUTPUT);
    pinMode(enPin, OUTPUT);
    digitalWrite(enPin, HIGH);
    // Set starting variables
    Serial.print("/*****************************************/\n");
    Serial.print("          Open program  \n");
    Serial.print("Current position [nm]: ");
    while (Serial.available()==0) {
    }
    CurrentPosition = Serial.parseFloat();                  // read current postion
    Serial.print(String(CurrentPosition) + " nm \n");
}

void loop(){
    float Error;
    float time1,time2;
    long int Num_steps;
    float parsed_Pos_nm, Pos_nm, fNum_steps;

    // Configure movement
    Error = Epsilon;
    Serial.print("/*****************************************/\n");
    Serial.print("Insert position to be reached [um]: ");
    while (Serial.available()==0) {
    }
    parsed_Pos_nm = Serial.parseFloat();
    Pos_nm = parsed_Pos_nm * 1000;
    Serial.print(String(Pos_nm) + " nm \n");
    fNum_steps = CalibrationCurve(k, Pos_nm-CurrentPosition);   // !! Affected by error
    Num_steps = NumberOfSteps(fNum_steps, Error);               // !! Purged of error
    Error = StepError(fNum_steps, Num_steps);

    if (Num_steps != 0){
        StartEnable();
        time1 = micros();
        Movement(Num_steps,pps);
        time2 = micros();
        StopEnable();

        time1 = (time2-time1)/1000000.;
        Serial.print("/----------  Observed parameters ----------/\n");
        Serial.print("Done " + String(Num_steps) + " steps\n");
```

```
        Serial.print("Delta t: " + String(time1) + " s\n");
        Serial.print("pps: "+ String(abs(Num_steps)/time1)+"\n");
        Serial.print("/-----------------------------------------/\n");
    }
    Pos_nm = InverseCalibrationCurve(k, Num_steps + Error);
    CurrentPosition = CurrentPosition + Pos_nm;
    Serial.print("Current position [nm]: " + String(CurrentPosition) + "\n");
    Serial.print("/*****************************************/\n\n\n");
}

/*=============================================================================*/
//                                  FUNCTIONS                                  //
/*=============================================================================*/

float CalibrationCurve(float k, float D_nm){
    // Convert from nm to steps with error
    // Input:
    //      * (float) k        -> [steps/nm], calibration coefficient
    //      * (float) D_nm     -> [nm], position to be converted
    // Output:
    //      * (float) D_steps -> [steps]
    float D_steps;

    D_steps = k * D_nm;
    return D_steps;
}

float InverseCalibrationCurve(float k, float D_steps){
    // Convert from steps to nm
    // Input:
    //      * (float) k        -> [steps/nm], calibration coefficient
    //      * (float) D_steps -> [steps], position to be converted
    // Output:
    //      * (float) D_nm     -> [nm]
    float D_nm;

    D_nm = D_steps / k;
    return D_nm;
}

long int NumberOfSteps(float D_steps, float Epsilon){
    // Convert to actual steps
    // Input:
    //      * (float) D_steps    -> [steps], wanted steps
    //      * (float) Epsilon    -> [steps], position error
    // Output:
    //      * (long int) D_steps -> [steps], possible steps
    long int N;

    N = round(D_steps + Epsilon);
    return N;
}

float StepError(float D_steps, long int N){
    // Evaluate the position error
    // Input:
    //      * (float) D_steps -> [steps], wanted steps
    //      * (long int) N    -> [steps], possible steps
    // Output:
    //      * (float) Epsilon -> [steps], position error
    float Epsilon;

    Epsilon = D_steps - float(N);
    return Epsilon;
}

void StartEnable(){
    digitalWrite(enPin, LOW);
}

void StopEnable(){
    digitalWrite(enPin, HIGH);
}

//muove di un certo numero di step.
void Movement(long int stepNum, float pps){
    // Movement cotrol
    // Input:
    //      * (long int) stepNum -> [steps], steps to be executed
    //      * (float) pps        -> [1/s], motor pulse-per-second
    DirectionControl(stepNum);
    for(int x = 0; x < abs(stepNum); x++){
        if (fmod(x, 30) == 0){
          Serial.print("\t" + String(x) + "\n");
        }
        digitalWrite(stepPin, HIGH);
        delayMicroseconds(500000/pps);
        digitalWrite(stepPin, LOW);
        delayMicroseconds(500000/pps);
    }
}
```

```
void DirectionControl(long int stepNum){
    // Define the movement direction according to the sign of the step number
    // Input:
    //      * (long int) stepNum -> [steps], possible steps
    if (stepNum < 0){
        digitalWrite(dirPin, LOW);
    }else{
        digitalWrite(dirPin, HIGH);
    }
}
```

Bibliography

[1] A. Müller, S. Marschall, O. B. Jensen, J. Fricke, H. Wenzel, B. Sumpf, and P. E. Andersen, "Diode laser based light sources for biomedical applications", *Laser & Photonics Reviews*, vol. 7, no. 5, pp. 605–627, Dec. 2012. DOI: 10.1002/lpor.201200051.

[2] A. Klimpel, D. Janicki, A. Lisiecki, and Z. Wilk, "Laser welding technologies: high power diode laser application examples", *Welding International*, vol. 24, no. 9, pp. 689–698, Sep. 2010. DOI: 10.1080/09507111003655077.

[3] J. Ming-Liu, *Photonic Devices*. Cambridge University Press, 2005. DOI: 10.1017/cbo9780511614255.

[4] L. A. Coldren, S. W. Corzine, and M. L. Mašanović, *Diode Lasers and Photonic Integrated Circuits*. Wiley John + Sons, Apr. 17, 2012, 744 pp., ISBN: 978-0-470-48412-8. DOI: 10.1002/9781118148167.

[5] G. Ghione, *Semiconductor Devices for High-Speed Optoelectronics*. Cambridge University Press, 2009. DOI: 10.1017/cbo9780511635595.

[6] P. Unger, "Introduction to Power Diode Lasers", in *Topics in Applied Physics*, Springer Berlin Heidelberg, 2000, pp. 1–54. DOI: 10.1007/3-540-47852-3_1.

[7] M. Behringer, "High-Power Diode Laser Technology and Characteristics", in *High Power Diode Lasers*, Springer New York, 2007, pp. 5–74. DOI: 10.1007/978-0-387-34729-5_2.

[8] A. Baranov, *Semiconductor Lasers: Fundamentals and Applications*. WOODHEAD PUB, 2013, 664 pp., ISBN: 9780857091215.

[9] C. L. Walker, A. C. Bryce, and J. H. Marsh, "Improved catastrophic optical damage level from laser with nonabsorbing mirrors", *IEEE Photonics Technology Letters*, vol. 14, no. 10, pp. 1394–1396, Oct. 2002. DOI: 10.1109/lpt.2002.802080.

[10] C. H. Henry, P. M. Petroff, R. A. Logan, and F. R. Merritt, "Catastrophic damage of $Al_xGa_{1-x}As$ double-heterostructure laser material", *Journal of Applied Physics*, vol. 50, no. 5, pp. 3721–3732, May 1979. DOI: 10.1063/1.326278.

[11] M. Hempel, "Defect mechanisms in diode lasers at high optical output power", en, PhD thesis, Humboldt-Universität zu Berlin, Mathematisch-Naturwissenschaftliche Fakultät I, Oct. 13, 2013. DOI: 10.18452/16834.

[12] J. W. Tomm, M. Ziegler, and T. Elsaesser, "Catastrophic optical mirror damage of high power diode lasers", in *2009 IEEE LEOS Annual Meeting Conference Proceedings*, IEEE, Oct. 2009. DOI: 10.1109/leos.2009.5343130.

[13] B. W. Hakki and F. R. Nash, "Catastrophic failure in GaAs double-heterostructure injection lasers", *Journal of Applied Physics*, vol. 45, no. 9, pp. 3907–3912, Sep. 1974. DOI: 10.1063/1.1663885.

[14] M. B. Sanayeh, "Catastrophic Optical Damage in High-Power AlGaInP Diode Lasers", Master's thesis, Universität Duisburg-Essen, Aug. 13, 2008.

[15] Y. Ueno, "Increased Catastrophic-Optical-Damage Output Power for High-Power Semiconductor Lasers Coated with High-Refractive-Index Films", *Japanese Journal of Applied Physics*, vol. 37, no. Part 2, No. 6A, pp. 646–648, Jun. 1998. DOI: 10.1143/jjap.37.l646.

[16] M. Silver, S. Hill, G. Masterton, and S. D. McDougall, "Experimental observation of the effect of laser standing wave pattern on the Catastrophic Optical Mirror Damage threshold for high-power single mode laser diodes.", in *LEOS 2008 - 21st Annual Meeting of the IEEE Lasers and Electro-Optics Society*, IEEE, Nov. 2008. DOI: 10.1109/leos.2008.4688912.

[17] C. L. Walker, A. C. Bryce, and J. H. Marsh, "Non absorbing mirror laser with improved catastrophic optical damage level", in *The 15th Annual Meeting of the IEEE Lasers and Electro-Optics Society*, IEEE, 2002. DOI: 10.1109/leos.2002.1159470.

[18] H. Taniguchi, H. Ishii, R. Minato, Y. Ohki, T. Namegaya, and A. Kasukawa, "25-W 915-nm Lasers With Window Structure Fabricated by Impurity-Free Vacancy Disordering (IFVD)", *IEEE Journal of selected topics in quantum electronics*, vol. 13, no. 5, pp. 1176–1179, 2007. DOI: 10.1109/jstqe.2007.903373.

[19] H. Yonezu, M. Ueno, T. Kamejima, and I. Hayashi, "An AlGaAs window structure laser", *IEEE Journal of Quantum Electronics*, vol. 15, no. 8, pp. 775–781, Aug. 1979. DOI: 10.1109/jqe.1979.1070102.

[20] T. Morita, T. Nagakura, K. Torii, M. Takauji, J. Maeda, M. Miyamoto, H. Miyajima, and H. Yoshida, "High-Efficient and Reliable Broad-Area Laser Diodes With a Window Structure", *IEEE Journal of Selected Topics in Quantum Electronics*, vol. 19, no. 4, pp. 1 502 104–1 502 104, Jul. 2013. DOI: 10.1109/jstqe.2013.2245103.

[21] P. J. Hughes, B. L. Weiss, and H. E. Jackson, "Composition and confinement energies of interdiffused AlGaAs/GaAs single quantum well structures", *Semiconductor Science and Technology*, vol. 12, no. 7, pp. 808–812, Jul. 1997. DOI: 10.1088/0268-1242/12/7/009.

[22] R. Beal, V. Aimez, and J. J. Dubowski, "Excimer laser induced quantum well intermixing: a reproducibility study of the process for fabrication of photonic integrated devices", *Optics Express*, vol. 23, no. 2, p. 1073, Jan. 2015. DOI: 10.1364/oe.23.001073.

[23] D. Hofstetter, B. Maisenholder, and H. P. Zappe, "Quantum-well intermixing for fabrication of lasers and photonic integrated circuits", *IEEE Journal of Selected Topics in Quantum Electronics*, vol. 4, no. 4, pp. 794–802, 1998. DOI: 10.1109/2944.720492.

[24] L. Hou and J. H. Marsh, "Photonic Integrated Circuits Based on Quantum well Intermixing Techniques", *Procedia Engineering*, vol. 140, pp. 107–114, 2016. DOI: 10.1016/j.proeng.2015.10.152.

[25] E. H. Li, "Advances in intermixed quantum well devices", in *Proceedings 1998 Hong Kong Electron Devices Meeting (Cat. No.98TH8368)*, IEEE, 1998. DOI: 10.1109/hkedm.1998.740188.

[26] W. C. H. Choy and E. H. Li, "Interdiffused AlGaAs-GaAs quantum well for improved electroabsorptive modulation", *IEEE Journal of Quantum Electronics*, vol. 34, no. 7, pp. 1162–1170, Jul. 1998. DOI: 10.1109/3.687859.

[27] J. S. Yu, J. D. Song, Y. T. Lee, and H. Lim, "Influence of impurity-free vacancy diffusion on the optical and optoelectronic properties of the $In_{0.53}Ga_{0.47}As/In_{0.52}Al_{0.48}As$ multiple quantum wells electroabsorption modulator structure", *Semiconductor Science and Technology*, vol. 20, no. 8, pp. 851–855, Jul. 2005. DOI: 10.1088/0268-1242/20/8/039.

[28] Y. Huang, C. Lien, and T.-F. Lei, "The enhanced Stark effects of coupled quantum wells and their application to tunable IR photodetectors", *Journal of Applied Physics*, vol. 74, no. 4, pp. 2598–2604, Aug. 1993. DOI: 10.1063/1.355293.

[29] M. D. Camras, N. Holonyak, R. D. Burnham, W. Streifer, D. R. Scifres, T. L. Paoli, and C. Lindström, "Wavelength modification of AlxGa1-xAs quantum well heterostructure lasers by layer interdiffusion", *Journal of Applied Physics*, vol. 54, no. 10, pp. 5637–5641, Oct. 1983. DOI: 10.1063/1.331825.

[30] S. Charbonneau, P. J. Poole, P. G. Piva, M. Buchanan, R. D. Goldberg, and I. V. Mitchell, "Bandgap tuning of semiconductor Quantum Well laser structures using high energy ion implantation", *Nuclear Instruments and Methods in Physics Research Section B: Beam Interactions with Materials and Atoms*, vol. 106, no. 1-4, pp. 457–460, Dec. 1995. DOI: 10.1016/0168-583x(95)00752-0.

[31] A. A. Al-Jabr, M. A. Majid, M. S. Alias, D. H. Anjum, T. K. Ng, and B. S. Ooi, "Large bandgap blueshifts in the InGaP/InAlGaP laser structure using novel strain-induced quantum well intermixing", *Journal of Applied Physics*, vol. 119, no. 13, p. 135 703, Apr. 2016. DOI: 10.1063/1.4945104.

[32] A. A. Al-Jabr, "Development of strain-induced quantum well intermixing technique on InGaP/InAlGaP laser structures and demonstration of first orange laser diode", PhD thesis, King Abdullah University of Science and Technology, 2016.

[33] O. Hulko, D. A. Thompson, and J. G. Simmons, "Quantitative compositional profiles of enhanced intermixing in GaAs/AlGaAs quantum well heterostructures annealed with and without a SiO_2cap layer", *Semiconductor Science and Technology*, vol. 24, no. 4, p. 045 015, Mar. 2009. DOI: 10.1088/0268-1242/24/4/045015.

[34] S. C. Du, L. Fu, H. H. Tan, and C. Jagadish, "Investigations of impurity-free vacancy disordering in (Al)InGaAs(P)/InGaAs quantum wells", *Semiconductor Science and Technology*, vol. 25, no. 5, p. 055 014, Apr. 2010. DOI: 10.1088/0268-1242/25/5/055014.

[35] M. Kuzuhara, T. Nozaki, and T. Kamejima, "Characterization of Ga out-diffusion from GaAs into SiO_xN_y films during thermal annealing", *Journal of Applied Physics*, vol. 66, no. 12, pp. 5833–5836, Dec. 1989. DOI: 10.1063/1.343603.

[36] J. F. Hazell, D. A. Thompson, N. Bertsch, J. G. Simmons, B. J. Robinson, and G. I. Sproule, "Intermixing of InGaAsP/InGaAsP quantum-well structures using dielectric films", *Semiconductor Science and Technology*, vol. 16, no. 12, pp. 986–991, Nov. 2001. DOI: 10.1088/0268-1242/16/12/307.

[37] J. S. Yu, J. D. Song, Y. T. Lee, and H. Lim, "Dependence of band gap energy shift of $In_{0.2}Ga_{0.8}As$/GaAs multiple quantum well structures by impurity-free vacancy disordering on stoichiometry of SiO_x and SiN_x capping layers", *Journal of Applied Physics*, vol. 91, no. 7, pp. 4256–4260, Apr. 2002. DOI: 10.1063/1.1448878.

[38] J. Choi, S. M. Han, S. I. Shah, S. G. Choi, D. H. Woo, S. Lee, S. H. Kim, J. I. Lee, K. N. Kang, and J. Cho, "Dependence of dielectric-cap quantum-well disordering of GaAs-AlGaAs quantum-well structure on the hydrogen content in SiN_x capping layer", *IEEE Journal of Selected Topics in Quantum Electronics*, vol. 4, no. 4, pp. 624–628, 1998. DOI: 10.1109/2944.720472.

[39] L. J. Guido, J. S. Major, J. E. Baker, W. E. Plano, N. Holonyak, K. C. Hsieh, and R. D. Burnham, "Column III vacancy- and impurity-induced layer disordering of $Al_xGa_{1-x}As$-GaAs heterostructures with SiO_2 or Si_3N_4 diffusion sources", *Journal of Applied Physics*, vol. 67, no. 11, pp. 6813–6818, Jun. 1990. DOI: 10.1063/1.345070.

[40] T. Haga, N. Tachino, Y. Abe, J. Kasahara, A. Okubora, and H. Hasegawa, "Out-diffusion of Ga and As atoms into dielectric films in SiOx/GaAs and SiNy/GaAs systems", *Journal of Applied Physics*, vol. 66, no. 12, pp. 5809–5815, Dec. 1989. DOI: 10.1063/1.343651.

[41] S. Bürkner, M. Maier, E. C. Larkins, W. Rothemund, E. P. O'reilly, and J. D. Ralston, "Process parameter dependence of impurity-free interdiffusion in $GaAs/Al_xGa_{1-x}As$ and $In_xGa_{1-x}As$/GaAs multiple quantum wells", *Journal of Electronic Materials*, vol. 24, no. 7, pp. 805–812, Jul. 1995. DOI: 10.1007/bf02653328.

[42] L. J. Guido, N. Holonyak, K. C. Hsieh, R. W. Kaliski, W. E. Plano, R. D. Burnham, R. L. Thornton, J. E. Epler, and T. L. Paoli, "Effects of dielectric encapsulation and As overpressure on Al-Ga interdiffusion in $Al_xGa_{1-x}As$-GaAs quantum-well heterostructures", *Journal of Applied Physics*, vol. 61, no. 4, pp. 1372–1379, Feb. 1987. DOI: 10.1063/1.338116.

[43] M. Katayama, Y. Tokuda, N. Ando, Y. Inoue, A. Usami, and T. Wada, "X-ray photoelectron spectroscopic study of rapid thermal processing on SiO_2/GaAs", *Applied Physics Letters*, vol. 54, no. 25, pp. 2559–2561, Jun. 1989. DOI: 10.1063/1.101544.

[44] M. Katayama, Y. Tokuda, Y. Inoue, A. Usami, and T. Wada, "Ga out-diffusion in rapid-thermal-processed GaAs with SiO_2 encapsulants", *Journal of Applied Physics*, vol. 69, no. 6, pp. 3541–3546, Mar. 1991. DOI: 10.1063/1.348496.

[45] I. Gontijo, T. Krauss, J. H. Marsh, and R. M. D. L. Rue, "Postgrowth control of GaAs/AlGaAs quantum well shapes by impurity-free vacancy diffusion", *IEEE Journal of Quantum Electronics*, vol. 30, no. 5, pp. 1189–1195, May 1994, ISSN: 0018-9197. DOI: 10.1109/3.303680.

[46] K. J. Beernink, D. Sun, D. W. Treat, and B. P. Bour, "Differential Al–Ga interdiffusion in AlGaAs/GaAs and AlGaInP/GaInP heterostructures", *Applied Physics Letters*, vol. 66, no. 26, pp. 3597–3599, Jun. 1995. DOI: 10.1063/1.113799.

[47] H.-S. Kim, J. W. Park, D. K. Oh, K. R. Oh, S. J. Kim, and I.-H. Choi, "Quantum well intermixing of $In_{1-x}Ga_xAs/InP$ and $In_{1-x}Ga_xAs/In_{1-x}Ga_xAs_{1-y}P_y$ multiple-quantum-well structures by using the impurity-free vacancy diffusion technique", *Semiconductor Science and Technology*, vol. 15, no. 10, pp. 1005–1009, Sep. 2000. DOI: 10.1088/0268-1242/15/10/314.

[48] J. S. Yu, J. D. Song, Y. T. Lee, and H. Lim, "Fabrication of multi-wavelength $In_{0.2}Ga_{0.8}As/GaAs$ multiple quantum well laser diodes by area-selective impurity-free vacancy disordering using SiO_x capping layers with different stoichiometries", *Applied Physics A*, vol. 80, no. 4, pp. 847–850, Feb. 2005. DOI: 10.1007/s00339-003-2323-1.

[49] S. Arslan, A. Demir, S. Şahin, and A. Aydınlı, "Conservation of quantum efficiency in quantum well intermixing by stress engineering with dielectric bilayers", *Semiconductor Science and Technology*, vol. 33, no. 2, p. 025 001, Jan. 2018, ISSN: 0268-1242. DOI: 10.1088/1361-6641/aaa04d.

[50] A. Kahraman, "Impurity-free Quantum Well Intermixing for High-Power Laser Diodes", Master's thesis, Graduate school of engineering and science of Bilkent University, Aug. 2015. [Online]. Available: http://hdl.handle.net/11693/29064.

[51] A. Kahraman, E. Gür, and A. Aydınlı, "Impurity-free quantum well intermixing for large optical cavity high-power laser diode structures", *Semiconductor Science and Technology*, vol. 31, no. 8, p. 085 013, Jul. 2016. DOI: 10.1088/0268-1242/31/8/085013.

[52] P. W. Epperlein, *Semiconductor Laser Engineering, Reliability and Diagnostics*. John Wiley & Sons Ltd, Feb. 2013. DOI: 10.1002/9781118481882.

[53] J. S. Yu, J. D. Song, Y. T. Lee, and H. Lim, "Influence of dielectric deposition parameters on the $In_{0.2}Ga_{0.8}As/GaAs$ quantum well intermixing by impurity-free vacancy disordering", *Journal of Applied Physics*, vol. 92, no. 3, pp. 1386–1390, Aug. 2002. DOI: 10.1063/1.1486027.

[54] M. Ying, P. Liu, Y. Xia, X. Liu, M. Zhao, S. Xiao, Y. Sun, and J. Pan, "Investigation of intermixing induced by sputtering and annealing in multiple quantum well", *Applied Surface Science*, vol. 205, no. 1-4, pp. 182–187, Jan. 2003. DOI: 10.1016/s0169-4332(02)01059-0.

[55] L. Pi-Jun, X. Yue-Yuan, L. Xiang-Dong, Y. Feng-Po, P. Jiao-Qing, X. Cheng-Shan, L. Yu-Guo, Z. Ming-Wen, and M. Yu-Chen, "Lattice Strain Induced by Ion Implantation in AlGaAs/AlGaInAs Quantum Well Samples", *Chinese Physics Letters*, vol. 19, no. 4, pp. 599–601, Mar. 2002. DOI: 10.1088/0256-307x/19/4/346.

[56] J. H. Marsh, S. A. Bradshaw, A. C. Bryce, R. Gwilliam, and R. W. Glew, "Impurity induced disordering of GaInAs quantum wells with barriers of AlGaInAs or of GaInAsP", *Journal of Electronic Materials*, vol. 20, no. 12, pp. 973–978, Dec. 1991. DOI: 10.1007/bf03030191.

[57] M. O'Neill, A. C. Bryce, J. H. Marsh, R. M. D. L. Rue, J. S. Roberts, and C. Jeynes, "Multiple quantum well optical waveguides with large absorption edge blue shift produced by boron and fluorine impurity-induced disordering", *Applied Physics Letters*, vol. 55, no. 14, pp. 1373–1375, Oct. 1989. DOI: 10.1063/1.101597.

[58] A. C. Bryce, J. H. Marsh, R. Gwilliam, and R. W. Glew, "Impurity induced disordering in InGaAs/InGaAlAs quantum wells using implanted fluorine and boron", *IEE Proceedings J Optoelectronics*, vol. 138, no. 2, p. 87, 1991. DOI: 10.1049/ip-j.1991.0015.

[59] S. I. Hansen, J. H. Marsh, J. S. Roberts, and R. Gwilliam, "Refractive index changes in a GaAs multiple quantum well structure produced by impurity-induced disordering using boron and fluorine", *Applied Physics Letters*, vol. 58, no. 13, pp. 1398–1400, Apr. 1991. DOI: 10.1063/1.104320.

[60] A. J. Steckl, "Review of focused ion beam implantation mixing for the fabrication of GaAs-based optoelectronic devices", *Journal of Vacuum Science & Technology B: Microelectronics and Nanometer Structures*, vol. 13, no. 6, p. 2570, Nov. 1995. DOI: 10.1116/1.588396.

[61] D. G. Deppe, N. Holonyak, W. E. Piano, V. M. Robbins, J. M. Dallesasse, K. C. Hsieh, and J. E. Baker, "Impurity diffusion and layer interdiffusion in $Al_xGa_{1-x}As$-GaAs heterostructures", *Journal of Applied Physics*, vol. 64, no. 4, pp. 1838–1844, Aug. 1988. DOI: 10.1063/1.341759.

[62] D. G. Deppe and N. Holonyak, "Atom diffusion and impurity-induced layer disordering in quantum well III-V semiconductor heterostructures", *Journal of Applied Physics*, vol. 64, no. 12, Dec. 1988. DOI: 10.1063/1.341981.

[63] B. S. Ooi, Y. S. Tang, A. S. Helmy, A. C. Bryce, J. H. Marsh, M. Paquette, and J. Beauvais, "Optical characterization of GaAs/AlGaAs quantum well wires fabricated using arsenic implantation induced intermixing", *Journal of Applied Physics*, vol. 83, no. 8, pp. 4526–4530, Apr. 1998. DOI: 10.1063/1.367236.

[64] H. H. Tan, C. Jagadish, and M. Gal, "Quantum well intermixing by proton irradiation", in *LEOS '95. IEEE Lasers and Electro-Optics Society 1995 Annual Meeting. 8th Annual Meeting. Conference Proceedings*, IEEE, 1995. DOI: 10.1109/leos.1995.484613.

[65] H. H. Tan and C. Jagadish, "Wavelength shifting in GaAs quantum well lasers by proton irradiation", *Applied Physics Letters*, vol. 71, no. 18, pp. 2680–2682, Nov. 1997. DOI: 10.1063/1.120177.

[66] S. Du, L. Fu, H. H. Tan, and C. Jagadish, "Comparison of proton and arsenic implantation-induced intermixing in InGaAsP/InGaAs/InP and InAlGaAs/InGaAs/InP quantum wells", in *2008 International Conference on Nanoscience and Nanotechnology*, IEEE, Feb. 2008. DOI: 10.1109/iconn.2008.4639238.

[67] L. Fu, H. H. Tan, M. B. Johnston, M. Gal, and C. Jagadish, "Proton irradiation-induced intermixing in InGaAs/(Al)GaAs quantum wells and quantum-well lasers", *Journal of Applied Physics*, vol. 85, no. 9, pp. 6786–6789, May 1999. DOI: 10.1063/1.370291.

[68] X. Q. Liu, X. S. Chen, Z. F. Li, W. Lu, S. C. Shen, H. H. Tan, S. Yuan, and C. Jagadish, "Proton implantation-induced intermixing effects on AlGaAs/GaAs single QW structures", *Physics Letters A*, vol. 278, no. 1-2, pp. 99–102, Dec. 2000. DOI: 10.1016/s0375-9601(00)00745-3.

[69] P. L. Gareso, H. H. Tan, J. Wong-Leung, C. Jagadish, and L. V. Dao, "Proton Irradiation Induced Intermixing in $In_xGa_{1-x}As$/InP Quantum Wells", in *Conference on Optoelectronic and Microelectronic Materials and Devices, 2004.*, IEEE, 2004. DOI: 10.1109/commad.2004.1577500.

[70] S. Moriwaki, M. Saitou, and T. Miyamoto, "Quantum well intermixing technique using proton implantation for carrier confinement of vertical-cavity surface-emitting lasers", *Japanese Journal of Applied Physics*, vol. 55, no. 8S3, Jul. 2016. DOI: 10.7567/jjap.55.08rc01.

[71] Y. S. Yun, S. Kim, H.-Y. Ryu, M.-S. Park, H. Jang, J. H. Song, W. C. Lim, Y. J. Chang, and W. J. Choi, "InGaAs/GaAs quantum well intermixing using proton irradiation for non-absorbing mirror", *Current Applied Physics*, vol. 16, no. 9, pp. 1005–1008, Sep. 2016. DOI: 10.1016/j.cap.2016.05.023.

[72] B. S. Ooi, J. H. Marsh, and A. C. Bryce, "Integration process for photonic integrated circuits using plasma damage induced layer intermixing", *Electronics Letters*, vol. 31, no. 6, pp. 449–451, Mar. 1995. DOI: 10.1049/el:19950342.

[73] H. S. Djie, C. Sookdhis, T. Mei, and J. Arokiaraj, "Photonic integration using inductively coupled argon plasma enhanced quantum well intermixing", *Electronics Letters*, vol. 38, no. 25, p. 1672, 2002. DOI: 10.1049/el:20021112.

[74] H. S. Djie, T. Mei, J. Arokiaraj, and P. Thilakan, "High-Density Plasma Enhanced Quantum Well Intermixing in InGaAs/InGaAsP Structure Using Argon Plasma", *Japanese Journal of Applied Physics*, vol. 41, no. Part 2, No. 8A, pp. 867–869, Aug. 2002. DOI: 10.1143/jjap.41.l867.

[75] T. Mei, H. S. Djie, J. Arokiaraj, and C. Sookdhis, "Understanding the inductively coupled argon plasma-enhanced quantum well intermixing", *Journal of Crystal Growth*, vol. 268, no. 3-4, pp. 384–388, Aug. 2004. DOI: 10.1016/j.jcrysgro.2004.04.059.

[76] H. S. Djie, T. Mei, J. Arokiaraj, C. Sookdhis, S. F. Yu, L. K. Ang, and X. H. Tang, "Experimental and Theoretical Analysis of Argon Plasma-Enhanced Quantum-Well Intermixing", *IEEE Journal of Quantum Electronics*, vol. 40, no. 2, pp. 166–174, Feb. 2004. DOI: 10.1109/jqe.2003.821542.

[77] H. S. Djie, T. Mei, J. Aroklaraj, and D. Nie, "Single step quantum well intermixing with multiple band gap control for III-V compound semiconductors", *Journal of Applied Physics*, vol. 96, no. 6, pp. 3282–3285, Sep. 2004. DOI: 10.1063/1.1780608.

[78] H. S. Djie, T. Mei, and J. Arokiaraj, "GaAs/AlGaAs quantum well intermixing using high-density argon plasma", *Semiconductor Science and Technology*, vol. 20, no. 2, pp. 244–249, Jan. 2005. DOI: 10.1088/0268-1242/20/2/025.

[79] H. S. Djie and T. Mei, "Plasma-induced quantum well intermixing for monolithic photonic integration", *IEEE Journal of Selected Topics in Quantum Electronics*, vol. 11, no. 2, pp. 373–382, Mar. 2005. DOI: 10.1109/jstqe.2005.845611.

[80] D. Leong, H. S. Djie, and P. Dowd, "A new quantum well intermixing technique using inductively-coupled Argon plasma on InGaAs/InGaAsP laser structures", in *Conference Proceedings. 14th Indium Phosphide and Related Materials Conference (Cat. No.02CH37307)*, IEEE, 2002. DOI: 10.1109/iciprm.2002.1014394.

[81] D. Nie, T. Mei, H. S. Djie, M. K. Chin, X. H. Tang, and Y. X. Wang, "Implementing multiple band gaps using inductively coupled argon plasma enhanced quantum well intermixing", *Journal of Vacuum Science & Technology B: Microelectronics and Nanometer Structures*, vol. 23, no. 3, p. 1050, 2005. DOI: 10.1116/1.1924414.

[82] C. Xu and T. Mei, "Inductively Coupled Argon Plasma-Enhanced Quantum-Well Intermixing: Cap Layer Effect and Plasma Process Influence", *IEEE Journal of Quantum Electronics*, vol. 45, no. 8, pp. 920–926, Aug. 2009. DOI: 10.1109/jqe.2009.2014649.

[83] J. Zhao, J. Guo, X. Huang, N. Zhou, and W. Liu, "Spatial control based quantum well intermixing in InP/InGaAsP structures using ICP", *Journal of Semiconductors*, vol. 33, no. 10, p. 106 001, Oct. 2012. DOI: 10.1088/1674-4926/33/10/106001.

[84] H. J. Chang, E. Y. Lin, K. Y. Chuang, C. L. Chiu, T. S. Lay, and T. Y. Chang, "Quantum Well Intermixing in InGaAs/InGaAlAs Structures by Using ICP-RIE and SiO_2 Sputtering", in *2007 IEEE 19th International Conference on Indium Phosphide & Related Materials*, IEEE, May 2007. DOI: 10.1109/iciprm.2007.381161.

[85] J. H. Marsh, A. C. Bryce, R. M. D. L. Rue, C. J. McLean, A. McKee, and G. Lullo, "Fabrication of quantum well photonic integrated circuits using laser processing", *Applied Surface Science*, vol. 106, pp. 326–334, Oct. 1996. DOI: 10.1016/s0169-4332(96)00414-x.

[86] B. S. Ooi, C. J. Hamilton, K. McIlvaney, A. C. Bryce, R. M. D. L. Rue, J. H. Marsh, and J. S. Roberts, "Quantum-well intermixing in GaAs-AlGaAs structures using pulsed laser irradiation", *IEEE Photonics Technology Letters*, vol. 9, no. 5, pp. 587–589, May 1997. DOI: 10.1109/68.588128.

[87] A. McKee, C. J. McLean, G. Lullo, A. C. Bryce, R. M. D. L. Rue, J. H. Marsh, and C. C. Button, "Monolithic integration in InGaAs-InGaAsP multiple-quantum-well structures using laser intermixing", *Journal of Quantum Electronics*, vol. 33, no. 1, pp. 45–55, 1997. DOI: 10.1109/3.554876.

[88] S. Balasubramanian, D. D. Nolte, and M. R. Melloch, "Enhanced diffusion in laser-annealed nonstoichiometric AlAs/GaAs heterostructures", *Journal of Applied Physics*, vol. 88, no. 8, p. 4576, 2000. DOI: 10.1063/1.1308104.

[89] T. K. Ong, O. Gunawan, B. S. Ooi, Y. L. Lam, Y. C. Chan, Y. Zhou, A. S. Helmy, and J. H. Marsh, "High-spatial-resolution quantum-well intermixing process in GaInAs/GaInAsP laser structure using pulsed-photoabsorption-induced disordering", *Journal of Applied Physics*, vol. 87, no. 6, pp. 2775–2779, Mar. 2000. DOI: 10.1063/1.372255.

[90] T. K. Ong, Y. W. Chen, B. S. Ooi, Y. L. Lam, and Y. C. Chan, "Pulsed-laser irradiation quantum well intermixing process in GaInAs/GaInAsP laser structures", *Microelectronic Engineering*, vol. 51-52, pp. 349–355, May 2000. DOI: 10.1016/s0167-9317(99)00506-7.

[91] B. S. Ooi, T. K. Ong, and O. Gunawan, "Multiple-wavelength integration in InGaAs-InGaAsP structures using pulsed laser irradiation-induced quantum-well intermixing", *IEEE Journal of Quantum Electronics*, vol. 40, no. 5, pp. 481–490, May 2004. DOI: 10.1109/jqe.2004.826431.

[92] J. Genest, J. J. Dubowski, V. Aimez, N. Pauc, D. Drouin, and M. Post, "UV laser controlled quantum well intermixing in InAlGaAs/GaAs heterostructures", *Journal of Physics: Conference Series*, vol. 59, pp. 605–609, Apr. 2007. DOI: 10.1088/1742-6596/59/1/129.

[93] J. Genest, J. J. Dubowski, and V. Aimez, "Suppressed intermixing in InAlGaAs/AlGaAs/GaAs and AlGaAs/GaAs quantum well heterostructures irradiated with a KrF excimer laser", *Applied Physics A*, vol. 89, no. 2, pp. 423–426, Aug. 2007. DOI: 10.1007/s00339-007-4230-3.

[94] J. Genest, "Quantum well intermixing controlled by excimer laser for photonic device integration", PhD thesis, Université de Sherbrooke, 2008.

[95] C. K. Chia, M. Suryana, and M. Hopkinson, "In situ control and monitoring of photonic device intermixing during laser irradiation", *Optics Express*, vol. 19, no. 10, p. 9535, May 2011. DOI: 10.1364/oe.19.009535.

[96] M. Kaleem, X. Zhang, Y.-g. Yang, Y. Zhuang, and J.-j. He, "Multi-bandgap photonic materials and devices fabricated by UV-laser induced quantum well intermixing", *Optoelectronics Letters*, vol. 9, no. 5, pp. 358–361, Aug. 2013. DOI: 10.1007/s11801-013-3088-1.

[97] Y. Zhuang, X. Zhang, M. Kaleem, and J.-J. He, "Large bandgap shift by UV excimer laser induced quantum well intermixing for photonic integration", in *2013 12th International Conference on Optical Communications and Networks (ICOCN)*, IEEE, Jul. 2013. DOI: 10.1109/icocn.2013.6617207.

[98] J. H. Marsh, "Laser induced quantum well intermixing for optoelectronic devices", in *Conference Proceedings LEOS'96 9th Annual Meeting IEEE Lasers and Electro-Optics Society*, IEEE, 1996. DOI: 10.1109/leos.1996.571948.

[99] A. S. Helmy, J. S. Aitchison, and J. H. Marsh, "Quantitative model for the kinetics of compositional intermixing in GaAs-AlGaAs quantum-confined heterostructures", *IEEE Journal of Selected Topics in Quantum Electronics*, vol. 4, no. 4, pp. 653–660, 1998. DOI: 10.1109/2944.720476.

[100] K. B. Kahen, D. L. Peterson, and G. Rajeswaran, "Effect of ion implantation dose on the interdiffusion of GaAs-AlGaAs interfaces", *Journal of Applied Physics*, vol. 68, no. 5, pp. 2087–2090, Sep. 1990. DOI: 10.1063/1.346562.

[101] J. Crank, *The Mathematics of Diffusion*, 340. JSTOR, May 1979, vol. 42, p. 165. DOI: 10.2307/3609455.

[102] S. L. Chuang, *Physics of Optoelectronic Devices*, ser. Wiley Series in Pure and Applied Optics. Wiley-Interscience, 1995, ISBN: 9780471109396. [Online]. Available: https://books.google.it/books?id=ect6QgAACAAJ.

[103] I. Gontijo, Y. S. Tang, R. M. D. L. Rue, C. M. S. Torres, J. S. Roberts, and J. H. Marsh, "Photoreflectance and photoluminescence of partially intermixed GaAs/AlGaAs double quantum wells", *Journal of Applied Physics*, vol. 76, no. 9, pp. 5434–5438, Nov. 1994. DOI: 10.1063/1.357199.

[104] R. Geursen, I. Lahiri, M. Dinu, M. R. Melloch, and D. D. Nolte, "Transient enhanced intermixing of arsenic-rich nonstoichiometric AlAs/GaAs quantum wells", *Physical Review B*, vol. 60, no. 15, pp. 10 926–10 934, Oct. 1999. DOI: 10.1103/physrevb.60.10926.

[105] A. S. Helmy, N. P. Johnson, M. L. Ke, A. C. Bryce, J. S. Aitchison, J. H. Marsh, I. Gontijo, G. S. Buller, J. Davidson, and P. Dawson, "A study of impurity-free vacancy disordering in GaAs-AlGaAs for improved modeling", *IEEE Journal of Selected Topics in Quantum Electronics*, vol. 4, no. 4, pp. 661–668, 1998. DOI: 10.1109/2944.720477.

[106] K. Nakamura, A. Shimizu, M. Koshiba, and K. Hayata, "Finite-element analysis of quantum wells of arbitrary semiconductors with arbitrary potential profiles", *IEEE Journal of Quantum Electronics*, vol. 25, no. 5, pp. 889–895, May 1989. DOI: 10.1109/3.27977.

[107] A. P. Zhao, S. R. Cvetkovic, and Z. Y. Yang, "Finite-element calculation of the influence of interdiffusion on eigenstates in a GaAs/$Al_xGa_{1-x}As$ single-quantum-well structure", *Optical and Quantum Electronics*, vol. 25, no. 11, pp. 845–851, Nov. 1993. DOI: 10.1007/bf00430190.

[108] K. Q. Le, "Finite element analysis of quantum states in layered quantum semiconductor structures with band nonparabolicity effect", *Microwave and Optical Technology Letters*, vol. 51, no. 1, pp. 1–5, Jan. 2009. DOI: 10.1002/mop.23976.

[109] S. Rihani, H. Page, and H. E. Beere, "Quasibound states in semiconductor quantum well structures", *Superlattices and Microstructures*, vol. 47, no. 2, pp. 288–299, Feb. 2010. DOI: 10.1016/j.spmi.2009.10.016.

[110] D. B. Topalović, V. V. Arsoski, S. Pavlović, N. A. Cukarić, M. Z. Tadić, and F. M. Peeters, "On Improving Accuracy of Finite-Element Solutions of the Effective-Mass Schrödinger Equation for Interdiffused Quantum Wells and Quantum Wire", *Communications in Theoretical Physics*, vol. 65, no. 1, pp. 105–113, Jan. 2016. DOI: 10.1088/0253-6102/65/1/105.

[111] K. Hayata, M. Koshiba, K. Nakamura, and A. Shimizu, "Eigenstate calculation of quantum well structures using finite elements", *Electronics Letters*, vol. 24, no. 10, pp. 614–616, May 1988. DOI: 10.1049/el:19880416.

[112] A. K. Ghatak, K. Thyagarajan, and M. r. Shenoy, "A novel numerical technique for solving the one-dimensional Schrödinger equation using matrix approach - Application to quantum well structures", *Journal of Quantum electronics*, vol. 24, no. 8, pp. 1524–1531, 1988. DOI: 10.1109/3.7079.

[113] C. Jirauschek, "Accuracy of Transfer Matrix Approaches for Solving the Effective Mass Schrödinger Equation", *Journal of Quantum Electronics*, vol. 45, no. 9, pp. 1059–1067, Sep. 2009. DOI: 10.1109/JQE.2009.2020998.

[114] D. P. Davé, "Numerical technique to calculate eigenenergies and eigenstates of quantum wells with arbitrary potential profile", *Electronics Letters*, vol. 27, no. 19, p. 1735, 1991. DOI: 10.1049/el:19911080.

[115] K. B. Kahen, D. L. Peterson, G. Rajeswaran, and D. J. Lawrence, "Properties of Ga vacancies in AlGaAs materials", *Applied Physics Letters*, vol. 55, no. 7, pp. 651–653, Aug. 1989. DOI: 10.1063/1.101811.

[116] H. Peyre, F. Alsina, J. Camassel, J. Pascual, and R. W. Glew, "Thermal stability of InGaAs/InGaAsP quantum wells", *Journal of Applied Physics*, vol. 73, no. 8, pp. 3760–3768, May 1993. DOI: 10.1063/1.352882.

[117] W. C. H. Choy and K. S. Chan, "Theoretical analysis of diffused quantum-well lasers and optical amplifiers", *Journal of Selected Topics in Quantum Electronics*, vol. 9, no. 3, pp. 698–707, May 2003. DOI: 10.1109/jstqe.2003.818842.

[118] O. Hulko, D. A. Thompson, and J. G. Simmons, "Comparison of Quantum Well Interdiffusion on Group III, Group V, and Combined Groups III and V Sublattices in GaAs-Based Structures", *IEEE Journal of Selected Topics in Quantum Electronics*, vol. 14, no. 4, pp. 1104–1112, 2008. DOI: 10.1109/jstqe.2008.920041.

[119] T. E. Schlesinger and T. Kuech, "Determination of the interdiffusion of Al and Ga in undoped (Al,Ga)As/GaAs quantum wells", *Applied Physics Letters*, vol. 49, no. 9, pp. 519–521, Sep. 1986. DOI: 10.1063/1.97107.

[120] D. H. W. Lau and J. Micallef, "Theoretical analysis of AlGaAs/GaAs quantum well waveguide defined by impurity-free vacancy diffusion", in *Physics and Simulation of Optoelectronic Devices VIII*, R. H. Binder, P. Blood, and M. Osinski, Eds., SPIE, Jul. 2000. DOI: 10.1117/12.391414.

[121] R. G. Gass and H. E. Jackson, "The time evolution of interdiffusion in multiple quantum wells: a new model of impurity-induced compositional intermixing", *IEEE Journal of Selected Topics in Quantum Electronics*, vol. 4, no. 4, pp. 669–674, 1998. DOI: 10.1109/2944.720478.

[122] Y. Chan and M. C. Y. Chan, "Multiple cations interdiffusion in InGaAs/InAlAs quantum well structure and their optical gain properties", in *Proceedings 1998 Hong Kong Electron Devices Meeting (Cat. No.98TH8368)*, IEEE, 1998. DOI: 10.1109/hkedm.1998.740190.

[123] M. C. Y. Chan, Y. Chan, and E. H. Li, "Modeling of optical gain properties of multiple cations InGaAs-InAlAs quantum-well intermixing", *IEEE Journal of Quantum Electronics*, vol. 34, no. 3, pp. 519–525, Mar. 1998. DOI: 10.1109/3.661461.

[124] I. Shtrichman, D. Gershoni, and R. Kalish, "Optical properties of GaAs/$Al_xGa_{1-x}As$ quantum wells disordered by ion implantation", *Physical Review B*, vol. 56, no. 3, pp. 1509–1515, Jul. 1997. DOI: 10.1103/physrevb.56.1509.

[125] Y. T. Oh, T. W. Kang, C. Y. Hong, K. T. Kim, and T. W. Kim, "The relation between Ga vacancy concentrations and diffusion lengths in intermixed GaAs/$Al_{0.35}Ga_{0.65}As$ multiple quantum wells", *Solid State Communications*, vol. 96, no. 4, pp. 241–244, Oct. 1995. DOI: 10.1016/0038-1098(95)00367-3.

[126] A. Pépin, "Evidence of stress dependence in SiO_2/Si_3N_4 encapsulation-based layer disordering of GaAs/AlGaAs quantum well heterostructures", *Journal of Vacuum Science & Technology B: Microelectronics and Nanometer Structures*, vol. 15, no. 1, p. 142, Jan. 1997. DOI: 10.1116/1.589240.

[127] P. N. K. Deenapanray, "Influence of Low-Temperature Chemical Vapor Deposited SiO_2 Capping Layer Porosity on GaAs/AlGaAs Quantum Well Intermixing", *Electrochemical and Solid-State Letters*, vol. 3, no. 4, p. 196, 1999. DOI: 10.1149/1.1391000.

[128] P. N. K. Deenapanray, H. H. Tan, M. I. Cohen, K. Gaff, M. Petravic, and C. Jagadish, "Silane Flow Rate Dependence of SiO_x Cap Layer Induced Impurity-Free Intermixing of GaAs/AlGaAs Quantum Wells", *Journal of The Electrochemical Society*, vol. 147, no. 5, p. 1950, 2000. DOI: 10.1149/1.1393464.

[129] P. N. K. Deenapanray and C. Jagadish, "Effect of Stress on Impurity-Free Quantum Well Intermixing", *Electrochemical and Solid-State Letters*, vol. 4, no. 2, 2001. DOI: 10.1149/1.1339242.

[130] H. H. Tan, P. N. K. Deenapanray, L. Fu, and C. Jagadish, "Effect of deposition parameters on SiO_x-enhanced intermixing in GaAs/AlGaAs quantum wells", in *1999 IEEE LEOS Annual Meeting Conference Proceedings. LEOS'99. 12th Annual Meeting. IEEE Lasers and Electro-Optics Society 1999 Annual Meeting (Cat. No.99CH37009)*, IEEE, 1999. DOI: 10.1109/leos.1999.811786.

[131] X. F. Liu, B. C. Qiu, M. L. Ke, A. C. Bryce, and J. H. Marsh, "Control of multiple bandgap shifts in InGaAs-AlInGaAs multiple-quantum-well material using different thicknesses of PECVD SiO2 protection layers", *IEEE Photonics Technology Letters*, vol. 12, no. 9, pp. 1141–1143, Sep. 2000. DOI: 10.1109/68.874215.

[132] P. Jucun, W. Boying, C. Jie, Z. Jie, and W. Yongchen, "Plasma-enhanced chemical vapordeposition SiO_2 film after ion implantation induces quantum well intermixing", *Journal of Wuhan University of Technology-Mater. Sci. Ed.*, vol. 21, no. 4, pp. 105–107, Dec. 2006. DOI: 10.1007/bf02841217.

[133] J. Ziegler, J. Biersack, and M. Ziegler, *SRIM: The Stopping and Range of Ions in Matter*. 2015.

[134] H. Naito, T. Nagakura, K. Torii, M. Takauji, H. Aoshima, T. Morita, J. Maeda, and H. Yoshida, "Long-Term Reliability of 915-nm Broad-Area Laser Diodes Under 20-W CW Operation", *IEEE photonics technology letters*, vol. 27, no. 15, pp. 1660–1662, Aug. 2015. DOI: 10.1109/lpt.2015.2433927.

[135] A. S. Helmy, S. K. Murad, A. C. Bryce, J. S. Aitchison, S. E. Hicks, and C. D. Wilkinson, "Control of silica cap properties by oxygen plasma treatment for single-cap selective impurity free vacancy diffusion", *Applied Physics Letters*, 1999. DOI: 10.1063/1.123106.

[136] S. E. Hicks, S. K. Murad, I. Sturrock, and C. D. Wilkinson, "Improving the resistance of PECVD silicon nitride to dry etching using an oxygen plasma", *Microelectronic Engineering*, vol. 35, no. 1-4, pp. 41–44, Feb. 1997. DOI: 10.1016/s0167-9317(96)00139-6.

[137] O. P. Kowalski, C. J. Hamilton, S. D. McDougall, J. H. Marsh, A. C. Bryce, R. M. D. L. Rue, B. Vögele, C. R. Stanley, C. C. Button, and J. S. Roberts, "A universal damage induced technique for quantum well intermixing", *Applied Physics Letters*, vol. 72, no. 5, pp. 581–583, Feb. 1998. DOI: 10.1063/1.120765.

[138] A. McKee, G. Lullo, C. J. McLean, B. C. Qiu, A. C. Bryce, R. M. D. L. Rue, and J. H. Marsh, "Extended cavity lasers fabricated using photo-absorption induced disordering", in *Conference Proceedings. 1997 International Conference on Indium Phosphide and Related Materials*, IEEE, 1997. DOI: 10.1109/iciprm.1997.600130.

[139] V. Hongpinyo, Y. H. Ding, C. E. Dimas, Y. Wang, B. S. Ooi, W. Qiu, L. L. Goddard, E. M. Behymer, G. D. Cole, and T. C. Bond, "Intermixing of InGaAs/GaAs Quantum Well Using Multiple Cycles Annealing", in *2008 IEEE PhotonicsGlobal@Singapore*, IEEE, Dec. 2008. DOI: 10.1109/ipgc.2008.4781312.

[140] L. R. Ram-Mohan, S. Saigal, D. Dossa, and J. Shertzer, "The finite-element method for energy eigenvalues of quantum mechanical systems", *Computers in Physics*, vol. 4, no. 1, p. 50, 1990. DOI: 10.1063/1.168374.

[141] M. G. Larson and F. Bengzon, *The Finite Element Method: Theory, Implementation, and Applications*. Springer Berlin Heidelberg, 2013. DOI: 10.1007/978-3-642-33287-6.

[142] J. Crank and P. Nicolson, "A practical method for numerical evaluation of solutions of partial differential equations of the heat-conduction type", *Advances in Computational Mathematics*, vol. 6, no. 1, pp. 207–226, Dec. 1996. DOI: 10.1007/bf02127704.